UNIVERSITY OF CALIFORNIA
RIVERSIDE

Measuring the Granularity of the Diffuse Hard X-ray Background

A dissertation submitted in partial satisfaction
of the requirements for the degree of

Doctor of Philosophy

in

Physics

by

Daniel Rufus MacDonald

June, 1999

Dissertation Committee:

Allen Zych, Chairman

Duane Gruber

Umar Mohideen

The Dissertation of Daniel Rufus MacDonald is approved:

Committee Chairman

University of California, Riverside

To

Duane

Acknowledgments

I would like to thank my mother and father for all their enduring support and encouragement. I hate to disappoint Muriel, Sue and Rob by actually graduating and getting a real job, but it is about time.

Allen Zych has been very patient during the eight years it has taken me to finish and has not complained about the lab work that we never got around to. He has continually looked out for me and has not seemed worried about my tendency to turn in everything at the last possible moment.

Umar Mohideen was very thoughtful to help me out at the last moment.

It is impossible to state how important Duane has been in getting me through this work. He is the only true renaissance man I know.

Martina spent a of time proof reading this text; and while complaining about my abuse of the language has given me a valuable non-specialists opinion. She is the only person who has read through this entire thing without being required to.

Susan Angello has always been convinced of, and enthusiastic about, the progress that I have made.

All the things I know about teaching I learned from Steve.

It took many people to make HEXTE work including Rick, Mike, Ed, Philippe and Biff, but it would not have been possible without Fred. Aside from teaching me everything I know about lab work and field work, working for uncle Freddie has been one of the most fun experiences I've had (Excluding Sheps).

All the programmers and computer support staff George Huszar, Tom Gasaway, Pete James and Stinky have been incredibly helpful; as have Shirley Roy and Cheryl Matson.

None of the analysis would have been possible if David Marsden had not taken the trouble to make get_accum work under many strange conditions.

David Kirkman was a major motivating force while we were both writing our dissertations. There is nothing more encouraging than someone saying 'I wrote 15 pages of solid science today. What have you done?'

I have to thank Joh3n and Dancing Boy for all the distractions that have made it fun to be here in the middle of the night.

Miss China has supplied about half of the food that I ate during the time I've spent in gradate school and I might not have made it through without the hot and sour soup.

This work was funded by NASA grants NAS5-3450, NAS5-4798 and NAS5-7119.

ABSTRACT OF THE DISSERTATION

Measuring the Granularity of the Diffuse Hard X-ray Background

by

Daniel Rufus MacDonald

Doctor of Philosophy, Graduate program in Physics

University of California, Riverside, June, 1999

Professor Allen Zych, Chairman

The diffuse X-ray background is widely held to originate largely from distant active galaxies. This view is supported by both counts of sources in survey missions and fluctuation studies in the soft x-ray energy band. However, most of the x-ray background emission occurs in the 10-60 keV hard x-ray band and sensitive studies in this energy band are only now possible.

The fluctuations in the x-ray background for three wide energy bands have been determined. They are 13.0 $\pm$ 2.1 % of XRB flux from 15.5 to 20.2 keV, 15.8 $\pm$ 2.7 % from 20.2 to 24.9 keV and 32 $\pm$ 11 % from 34 to 41 keV for a 1.1 square degree field of view.

During normal observations, the High Energy X-ray Timing Experiment instrument (HEXTE) on the Rossi X-ray Timing Explorer (RXTE) Spacecraft makes

nearly simultaneous observations of two pairs of background fields separated by 3.0 degrees. Differences in fluxes from these pairs of background fields can be used to detect a source population much deeper than can be studied from individual detections. A measurement of the fluctuations in the X-ray background in wide energy bands above 15 keV can be made using the ensemble of all long RXTE pointings, a total of $\sim$36.7 million seconds of observations. A distribution of the sky flux differences can be made from a data set of these long pointings. Tails in the distribution of the differences are dominated by sources that occur at a spatial density of one source per field of view. The nominal HEXTE instrument field of view is one square degree, but this field can be smeared out by seasonal rotation of the spacecraft pointing. An excess variation can be found by comparing the the fluctuation distribution to a distribution characterized by a data set that only contains statistical counting errors. This excess variation in wide energy bands is used to create the fluctuation spectrum.

In a field created by a distribution of discrete sources, the fractional fluctuations — the smoothness of the field — is determined by the number of sources which create the field. Knowing the fractional fluctuations, the source density can be calculated.

The spectrum of the source density, when combined with data from the HEAO-1 A4 instrument, results in an energy power law spectral index to the number of sources of -0.64 $\pm$ 0.20 from 15 to 80 keV. This result is in direct disagreement with models of the XRB in which the emission in this energy range is dominated by a class of sources more numerous than Seyfert 1s.

Contents

List of Figures

List of Tables

Chapter 1

Introduction

1.1 What is The X-ray Background?

The diffuse X-ray background (XRB) radiation is the second most luminous isotropic radiation field in the sky. The XRB is believed to be of a much more recent origin than the brightest radiation field, the Cosmic Microwave Background (CMB). The XRB is thought to originate from a redshift of z $\sim$ 1 [Schwartz and Gursky 1974]. If the sources of the XRB are distributed like the density fluctuations, then the XRB is an indicator of large scale structure at that epoch. To show the relative energetic relation between the two isotropic radiation fields, figure 1.1 from [Fabian and Barcons 1992] shows the background radiation from radio to gamma rays, in units of constant energy per decade. In these units the areas under the curves at different wavelengths represent the same energy flux. The figure shows

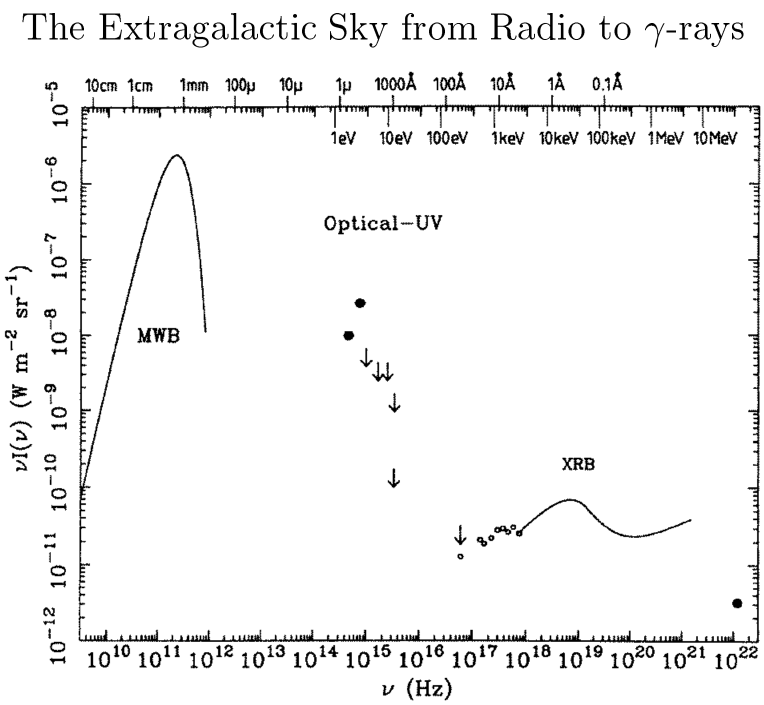

Figure 1.1: Energy spectrum of extragalactic sky in units of constant energy per decade. Arrows in the optical and UV regions are upper limits. From [Fabian and Barcons 1992]. In these units a horizontal line represents a constant energy flux at all wavelengths. The Frequency on the horizontal axis goes from radio on the left to gamma-rays on the right. The cosmic microwave background is labeled as MWB

the CMB, the feature labeled MWB in the radio region on the left side of the figure, and the XRB on the right.

Although referred to as diffuse, the XRB is considered to be either partially or wholly composed of an ensemble of discrete sources. Perhaps half of the XRB emission at energies of a few keV can be attributed to different classes of galaxies [Zdziarski *et al.* 1995], having a central non-stellar radiation source — active galaxies.

Many different phenomena at wavelengths from radio to gamma-rays are responsible for the classification of different types of active galaxies. They display differing luminosities, spectral properties and variabilities. The combined emission from these active galaxies, which are too dim to be detected individually create a seemingly isotropic radiation field — the XRB. The XRB can be seen in the background of the x-ray image of the moon shown in figure 1.2 from [Schmitt *et al.* 1991], which shows solar x-rays reflected by the moon. The sun illuminates the right side of the

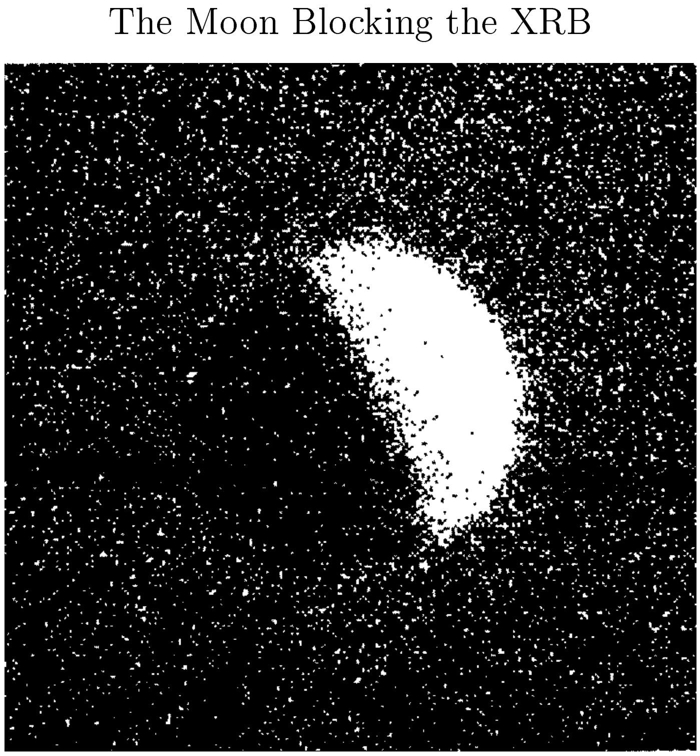

Figure 1.2: ROSAT Image of the Moon and the XRB soft x-rays (0.1 – 2 keV) from [Schmitt *et al.* 1991]. The XRB can be seen in the surrounding sky, in the area that is not shadowed by the moon. The counts on the left side of the moon are the level of instrumental noise. The right side of the moon is illuminated by the sun.

moon, but the few counts on the dark side of the moon, which blocks the background radiation, result only from instrumental noise. The XRB was actually discovered in an early attempt to see reflected solar x-rays from the moon [Giacconi *et al.* 1962].

1.2 History of the X-ray Background

The x-ray background was the first cosmic radiation field to be discovered and predated the discovery of the more energetic cosmic microwave background by several years [Penzias and Wilson 1965]. The XRB was discovered by [Giacconi *et al.* 1962] during a rocket flight to measure solar x-rays reflected from the moon. The source of this radiation has been an ongoing field of research since that time. Giacconi's first measurement of the background is shown in figure 1.3. The figure shows the counting rate in the instruments two functioning detectors as a function of the azimuthal angle of the rotating rocket. The large counting rate in the southwest is due to point sources. The instrumental background has been subtracted from the counting rate so that the constant offset from zero counting rate is due to the flux from the XRB. The open circles in the figure are from the detector with the thinner window, which is more sensitive to lower energy x-rays. The higher offset from zero count rate in this lower energy detector indicates that the XRB flux is decreasing with increasing energy.

From this rough spatial and spectral measurement, the study of the spectrum and spatial properties of the XRB began. The first spectral fit over a wide energy range in the XRB came from a compilation of different experiments which were fit

First Measurement of the XRB

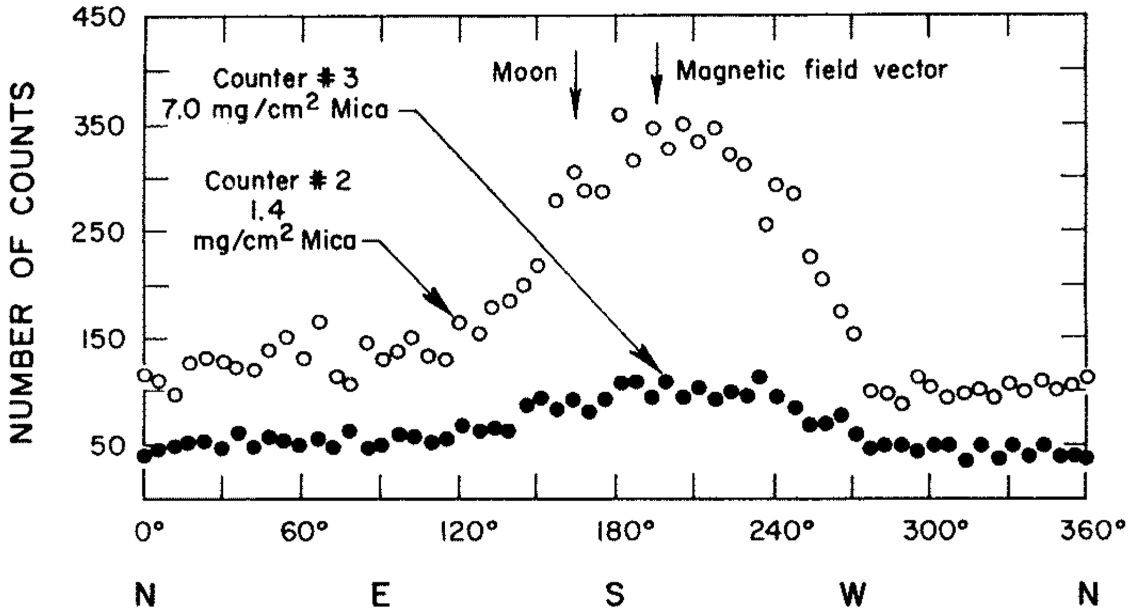

Figure 1.3: Number of counts vs. azimuth angle. The numbers represent counts accumulated in 350 seconds in each 6° angular interval. From [Giacconi *et al.* 1962]. The increased count rate in the southwest is due to point sources while the constant offset from zero count rate is due to the XRB.

as a power law by [Gould 1967]. Gould was the first to fit the XRB spectrum from 1 keV to 1 MeV and found a power law with an energy index of 2.3.

1.2.1 Spectrum

The third Orbiting Solar Observatory (OSO-3) was the first to examine the XRB using a complete sky survey. [Schwartz 1969] measured the spectrum in seven energy bins from 7 to 213 keV which is the energy range where the XRB is most energetic (figures 1.1 and 1.4). Schwartz found that a single power law spectral form could not fit the OSO-3 observations.

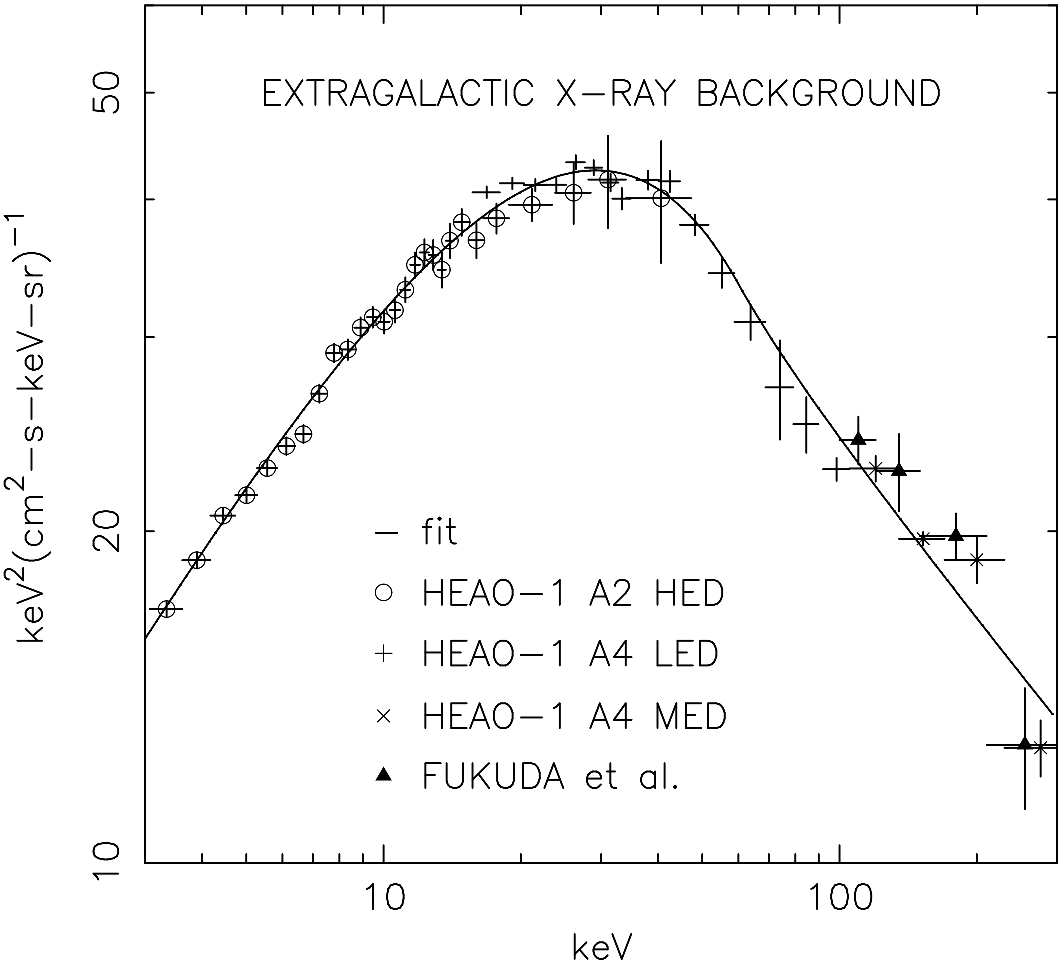

Figure 1.4: The spectrum of the XRB from HEAO-1 is shown with Grubers empirical fit in units of constant energy per decade. From [Gruber *et al.* 1999].

The first High Energy Astrophysical Observatory (HEAO-1) observed the XRB over an energy range even wider than OSO-3, 3 keV – $\frac{1}{2}$ MeV [Marshall *et al.* 1980] [Gruber 1992] [Gruber *et al.* 1999] (figure 1.4). Gruber also created a piecewise empirical fit to the XRB spectrum, given in units of keV/(cm^2-s-keV-sr) :

$$7.877E^{-.29} * e^{-E/41.13} \qquad\qquad 3keV < E < 60keV$$

and

$$0.0259(E/60)^{-5.5} + 0.504(E/60)^{-1.59} + 0.0288(E/60)^{-1.05} \qquad 60keV < E < 6000keV.$$

Which is shown as the solid line in figure 1.4. The functional form for the lower energy portion was developed by [Boldt 1987].

1.2.2 Uniformity

The first measurement of the uniformity of the XRB, which led to an explanation of an extragalactic origin for the radiation, came from OSO-3 and set a limit of 5% to the galactic halo contribution to the XRB in the 8–40 keV energy range [Schwartz 1969]. Later analysis of the Uhuru satellite measurements in the 1 – 10 keV range by [Schwartz and Gursky 1974] found the XRB to be isotropic to a limit of 3%. A sample of one great circle strip of the Uhuru data is shown in figure 1.5. The independence of the counting rate to galactic latitude in the figure suggests the extragalactic origin of the background.

The nonuniformity in the XRB has been characterized in different ways. At the largest angular scales, there have been attempts to measure the dipole term of the nonuniformity. The dipole variation amplitude for an observer with a velocity v

Uhuru Scan of Sky-Strip

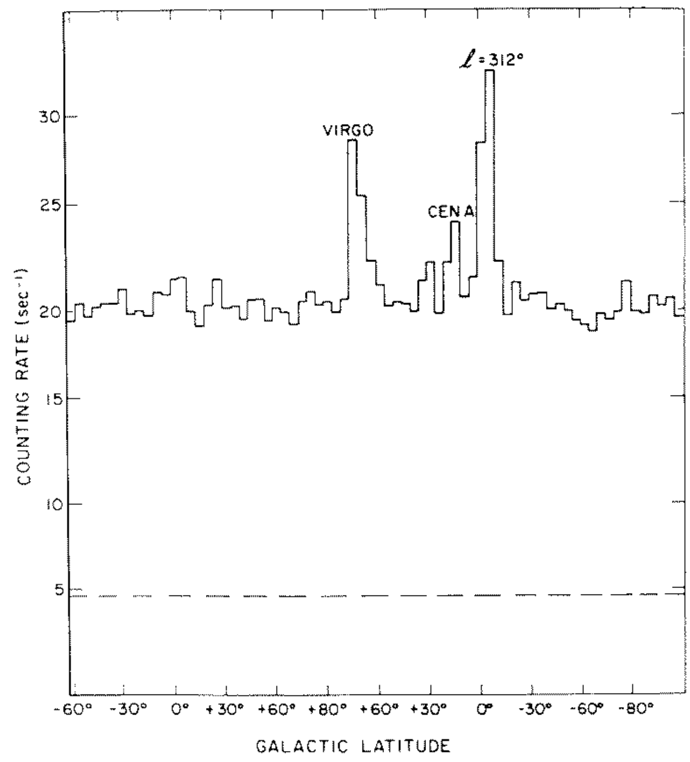

Figure 1.5: One day of Uhuru counting rates along great circle through the galactic poles showing an isotropic background. Instrumental background is shown as dashed line. [Schwartz and Gursky 1974]

relative to the field of flux S is:

$$\frac{\delta S}{S} = (2 + \Gamma)(v/c) cos\theta$$

Where $(2 + \Gamma)$ is the Compton-Getting factor for a power law spectrum of index Γ.

Since the discovery of the CMB dipole by [Henry 1971] attempts have been made to measure the expected dipole term in the XRB to compare it to the dipole measurements of the CMB. From the last survey mission, the HEAO-1, [Shafer 1983] using the A2 experiment, found a marginally significant dipole term that agreed in direction and velocity with the CMB dipole term. [Gruber 1992] had indications of a dipole term in the HEAO-1 A4 data that also agreed generally with the CMB. It is interesting that these observations have about the same error boxes as Henry's CMB measurement of $10\frac{1}{2} \pm 4$ h right ascension and -30 $\pm$ 25° declination.

At smaller angular scales, granularity or fluctuation measurements have been made by survey missions. Perhaps the easiest way to see the fluctuations in the background is to look at the HEAO A2 skymap in figure 1.6. The maps are in galactic coordinates and the XRB fluctuations are seen as the graininess in the areas away from the central horizontal area — the galactic plane.

Fluctuation measurements were made by HEAO with both the soft x-ray A2 experiment and the hard x-ray A4 experiment. From the A2 data, [Shafer 1983] found fluctuations of 2% on a 49 square degree angular scale. ([Gruber 1992]) using the A4 instrument found RMS fluctuations in hard x-rays of about 0.3% on a 200 square degree scale (see section 1.6 on fluctuations).

1.3 Why is the X-ray Background important?

The identity of the process or sources that create the XRB is the most basic unanswered question about the background. The spectral shape of the background being very consistent with thin thermal bremsstrahlung, suggests a hot emitting gas at a

HEAO-1 A2 Map of Sky in X-Rays

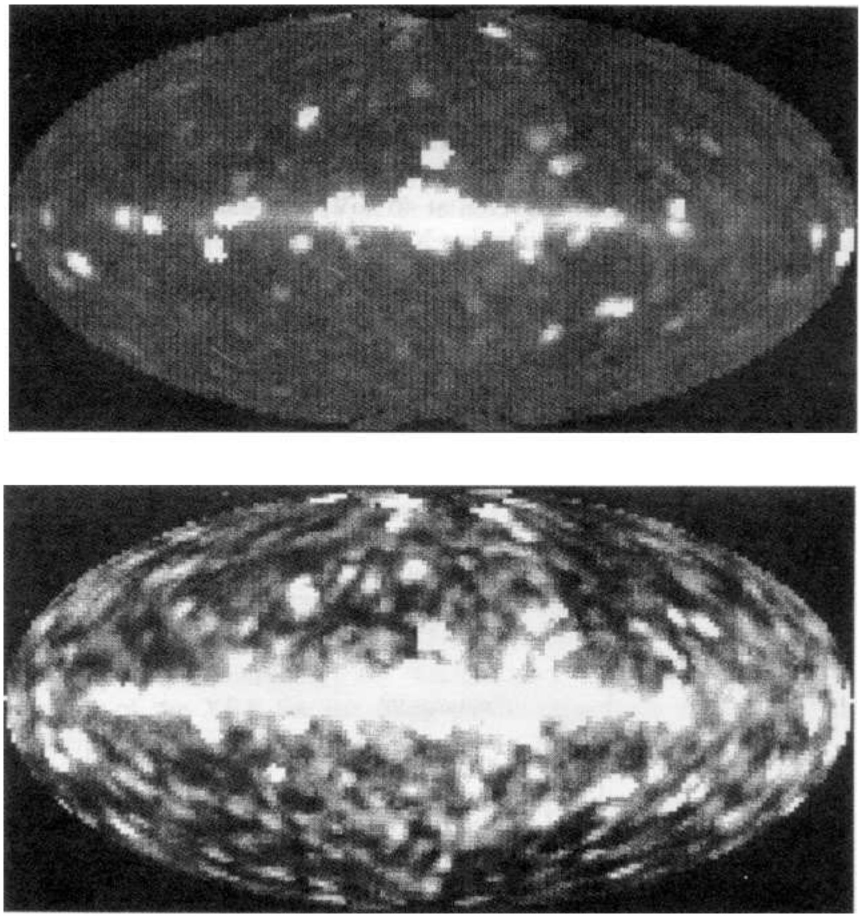

Figure 1.6: Map of sky in 2 – 10 keV x-rays from the HEAO-1 A2 experiment. The galaxy is the bright band in the center of the images. XRB fluctuations can be seen outside of the galactic plane. The lower map has increased contrast to better show the fluctuations. Maps courtesy of K. Jahoda.

temperature of 40 keV [Taylor and Wright 1989] but this origin has been found to be an unsatisfactory explanation on both theoretical and observational grounds (see section 1.5).

Although we generally refer to the XRB as isotropic and structureless, it tells us about the nature and properties of the contributing sources at the time that the x-radiation was emitted from these sources. If the sources are a good indicator of the overall mass distribution at $z \sim 1$, then the XRB is a good indicator of the formation of large scale structure at that epoch [Carrera, Fabian, and Barcons 1997] [Lahav, Piran, and Treyer 1997]. Unfortunately, data from my study is not sensitive to the large scale structure. Our difference measurements are measures of the fluctuations in the background at a 3° scale, but we can not measure the relation between our difference measurement and the average flux. Without this information we cannot separate the signal from the discrete source statistics from the signal from large scale structure [Carrera, Fabian, and Barcons 1997]. Our difference measurements can be used as a measure of the number of sources in the observation field. Limits to the number density of the sources of the XRB can be derived (section 5.1.2). These are sensitive enough to constrain current models of the XRB.

From an instrumental point of view, this study is a measurement of the average properties of sources that individually would be below the detection threshold of the instrument, the High Energy X-ray Timing Experiment (HEXTE) which is described in chapter 2.

1.4 Why is HEXTE the instrument to use?

The peak in the power of the XRB is at ~ 40 keV (see figure 1.1) which fits well within the HEXTE band of 12-256 keV (see chapter 2 for HEXTE specifications). HEXTE is not a survey instrument and so unevenly samples the sky. Yet the observing program gives access to large amounts of exposure time (see section 3.2 on coverage). Data for this study are collected at almost all times that HEXTE is not pointed in the galactic plane. During the course of observing objects, HEXTE collects off-source data to subtract internal instrumental background. We have used this data, approximately 36.7 million seconds of observing time, collected during almost all observations to measure the background.

The difference in the counting rates between pairs of nearby fields are used for this study because the signal from the XRB is overwhelmed by internal detector noise which must be carefully removed. The fast beam switching employed by the HEXTE instrument is designed to remove the instrumentation noise from the sky signal in a much more reliable way than was previously possible (section 2.1.3). This allows data to be taken at times when models to predict instrumental noise have problems with reliability such as parts of the orbit with large charged particle fluxes, which substantially increase instrument noise (section 2.3.2).

1.5 X-ray Background Sources

Historically there have been two different classes of source models for the XRB. The first model was that of a hot diffuse gas [Taylor and Wright 1989]. This stemmed from the spectral shape of the background, which looked like a thin thermal bremsstrahlung spectrum with a temperature of 40 keV. There are several problems with this model. The density of a uniform gas required to create the flux of the XRB is several times the measured average baryon density [Tytler *et al.* 1999]; although this difficulty can be reduced by clumping the matter, it is difficult to eliminate [Guilbert and Fabian 1986]. Problems also arise from the contributions of known classes of AGN. If these sources contribute more than $\sim 20\%$ of the XRB flux, they distort the spectrum of the remaining flux so that is no longer resembles that of a 40 keV gas [Guilbert and Fabian 1986]. Fluctuation measurements also rule out this model since the shape of the distribution of the fluctuations is different for truly diffuse and discrete models (see sections 1.6 and 5.1.1). But this source model was conclusively put to rest by [Mather *et al.* 1990] using an entirely different technique.. Using COBE data they failed to find the expected Sunyaev Zel'dovich effect, a distortion of the CMB caused by inverse Compton scattering of the CMB from the electrons of the hot diffuse gas necessary for a truly diffuse XRB. Their measurement limited the contribution of a hot diffuse gas to a few percent of the observed flux. The possible hot gas contribution to the XRB was later lowered by two orders of magnitude by analyzing the spectral shape of the CMB using four years of data from the COBE instrument [Mather *et al.* 1994].

1.5.1 Hard X-ray Spectral Paradox

One of the most persistent problems with modeling the XRB is the shape of the spectrum. As mentioned above it is well fit by thermal bremsstrahlung emission. Unfortunately, once the contributions of known classes of sources is removed, the spectrum no longer resembles a hot gas [Guilbert and Fabian 1986].

Under a model of discrete sources, where the known contributions of different types of active galaxies such as QSOs and Seyfert-1 galaxies are removed, the remaining flux has a spectral shape that is too flat below 40 keV to fit any of the known classes of x-ray objects (see figure 1.7). Redshifting the populations of the emitting sources up to redshifts of z $\sim$ 6 helps but does not eliminate this problem [Zdziarski, Zycki, and Krolik 1993]. Elihu Boldt coined the term 'spectral paradox' for this problem.

1.5.2 X-ray Background Source Models

Active Galaxies (AG) have been actively investigated [Giacconi and Zamorani 1987] [Zdziarski 1996] [Ueda *et al.* 1998] as the likely major contribution to the XRB. Active galaxies are those which emit radiation from a central component, the nucleus (AGN), which doesn't seem to be due to the stars in the galaxy. There are a number of different types of AGN whose central emission ranges over many orders of magnitude from a fraction of the flux from the stars to completely overwhelming the flux from the rest of the galaxy. Figure 1.7 from [Zdziarski 1996] shows a model fit containing contributions from known classes of sources to the XRB where the densities of the different components have been adjusted to fit the data.. The

Model Fit to XRB Spectrum

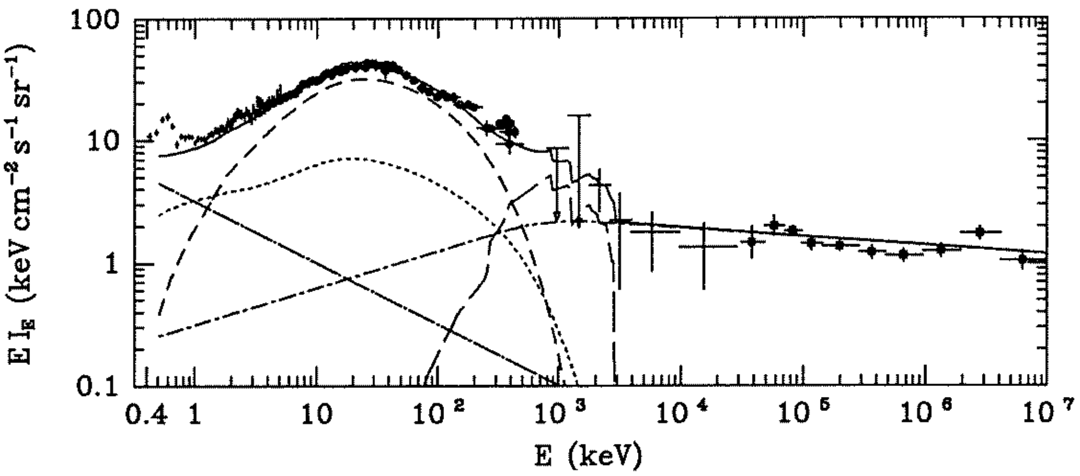

Figure 1.7: A model fit to the XRB spectrum [Zdziarski 1996] with contributions from different classes of AGN. The long dashed-dotted line is the QSO component. The short dashed-dotted line is the Blazar component. The short dashed line is the Seyfert-1 galaxies and the long dashed line is the remainder which [Zdziarski 1996] model as Seyfert-2 galaxies. Normalizations for the different spectral components have been adjusted to fit the data.

unified AGN model views different classes of active galaxies as one phenomena whose different manifestations depend largely on viewing angle. This leads to the postulation of a large population of absorbed AGN, type 2 Seyfert galaxies, which are weak sources in the few keV energy where the majority of the work on the XRB has been performed. Although weak in the soft x-ray band, these type 2 Seyfert galaxies could contribute a large fraction of the remaining flux to the XRB. Type 2 Seyfert galaxies are the most populous of the active galaxies (see table 5.1). The unified AGN model is discussed in section 5.2.1.

1.6 Fluctuations

Fluctuations are the deviations from the average flux $< S >$ of the XRB at a specific point. $D = S- < S >$ The fluctuations are represented by the letter D since its first use with radio observations, where the fluctuations were deviations of a signal. This method of analysis was adapted to x-ray observations by [Scheuer 1973] from his previous radio work [Scheuer 1957]. In the simplest case of the XRB being a set of identical sources observed with a uniform beam of solid angle Ω, given N sources per field of view, the variation in that field will be governed by Poisson statistics — approximately $\sqrt{N}$. The fractional fluctuation in the field will be $\frac{1}{\sqrt{N}}$ and is proportional to $\frac{1}{\sqrt{\Omega}}$. The distributions of the fluctuations for more realistic source distributions and beam profiles is discussed in section 5.1.

Observations of the fluctuations in the background give us information on the source distribution which is dominated by sources on the scale of one source per field of view (see Section 5.1.1). If the XRB was a truly diffuse field, the distribution of the observed fluctuations would be just measurement noise. If the sources are discrete, the distribution of the fluctuations takes a different and broader form which is dependent upon the spatial distribution of the sources and the number density. See Section 5.1.

Chapter 2

Instrument

The X-Ray Timing Explorer (XTE) was launched on December 30 1995. It carries three different instrument packages. The All Sky Monitor (ASM) [Levine *et al.* 1996] is a survey instrument and the other two are pointed instruments, the Proportional Counter Array (PCA) [Jahoda *et al.* 1996] and the High Energy X-Ray Timing Experiment (HEXTE) [Rothschild *et al.* 1998]. The PCA and HEXTE operate in complementary energy ranges; the PCA from 2 to 60 keV and HEXTE from 15 to 250 keV. XTE was launched into a low earth orbit with an inclination angle of 23° at an altitude of 600 km which gives an orbital period of approximately 90 minutes.

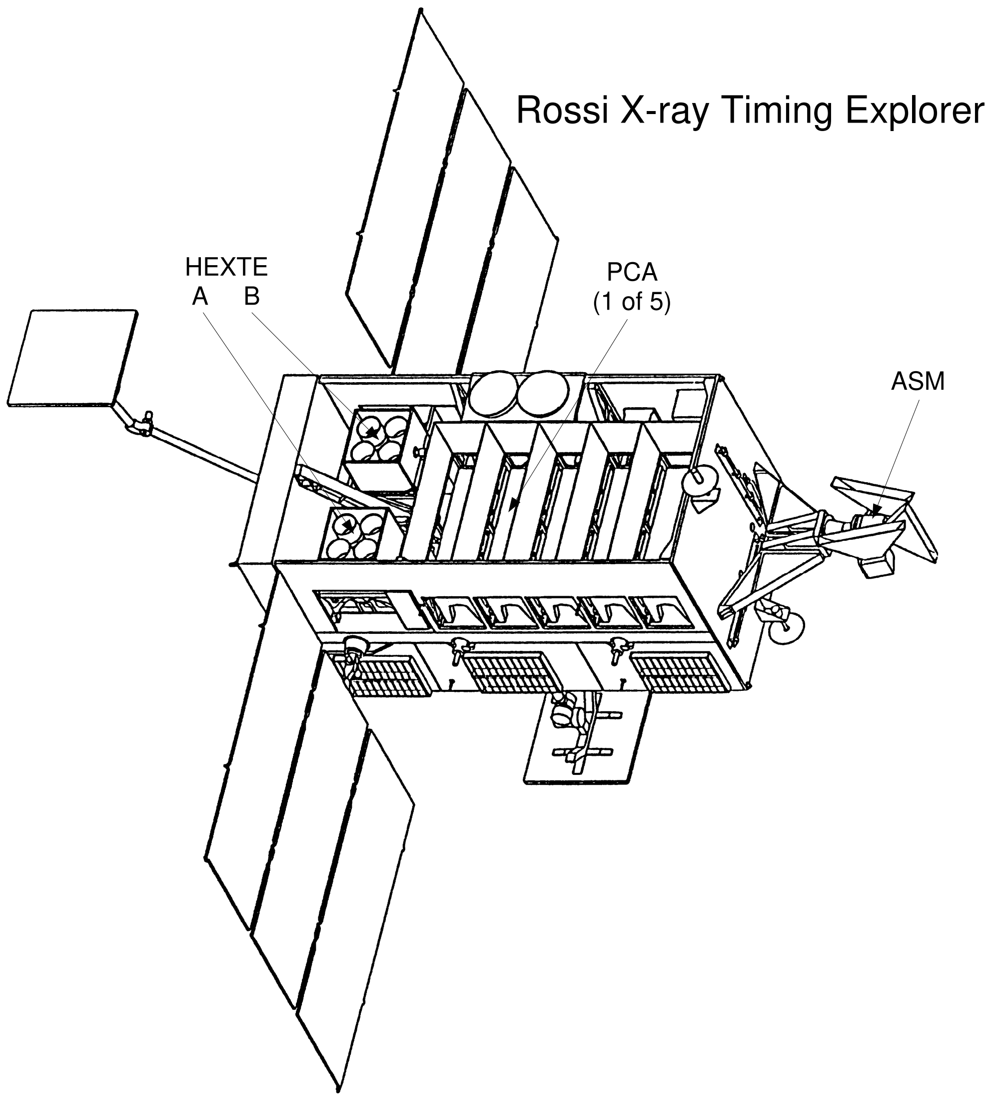

Figure 2.1: The XTE spacecraft. The Three instruments are shown. The High Energy X-Ray Timing Experiment (HEXTE) and the Proportional Counter Array (PCA) are pointed instruments while the All Sky Monitor (ASM) scans the sky. From [Rothschild *et al.* 1998].

2.1 HEXTE Specifications

The HEXTE instrument consists of eight Phoswich scintillation detectors, and their necessary electronics, divided into two identical clusters (Figure 2.3). Each cluster has an independent data path and moves on and off axis, "rocking", by a few degrees independently with the rocking axes offset 90° in order to obtain detector background.

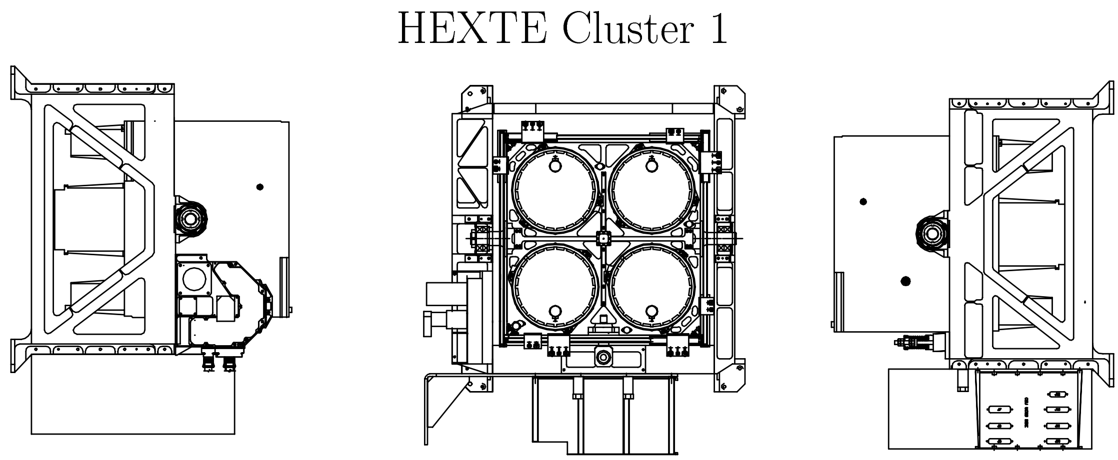

Figure 2.2: HEXTE Cluster 1 is shown from three sides. The side towards the PCA instrument is down in all three figures. The central figure is along the viewing axis looking down the Phoswich collimators. In all three figures, the rotation axis is in the horizontal plane and the bushings can be seen at the ends of the rocking axis.

The two Clusters are positioned at one end of the XTE spacecraft as in figure 2.3. Cluster 1 rocks towards and away from the PCA while cluster 2 rocks towards and away from cluster one. The clusters are independently powered and commanded, even though they have identical software and identical hardware with the exception of the positions of components with respect to the rocking axes. There is a confusing overabundance of naming schemes for the HEXTE clusters. They evolved from differences in the hardware and software designations in the instrument and various attempts to correct the ambiguities. There are at least four different naming schemes for the clusters : 0 and 1, 1 and 2, A and B, and finally 0 and B. I will refer to the cluster that rocks towards and away from the PCA as cluster 1 and the other as cluster 2, although images from other sources such as figure 2.1 may use other schemes.

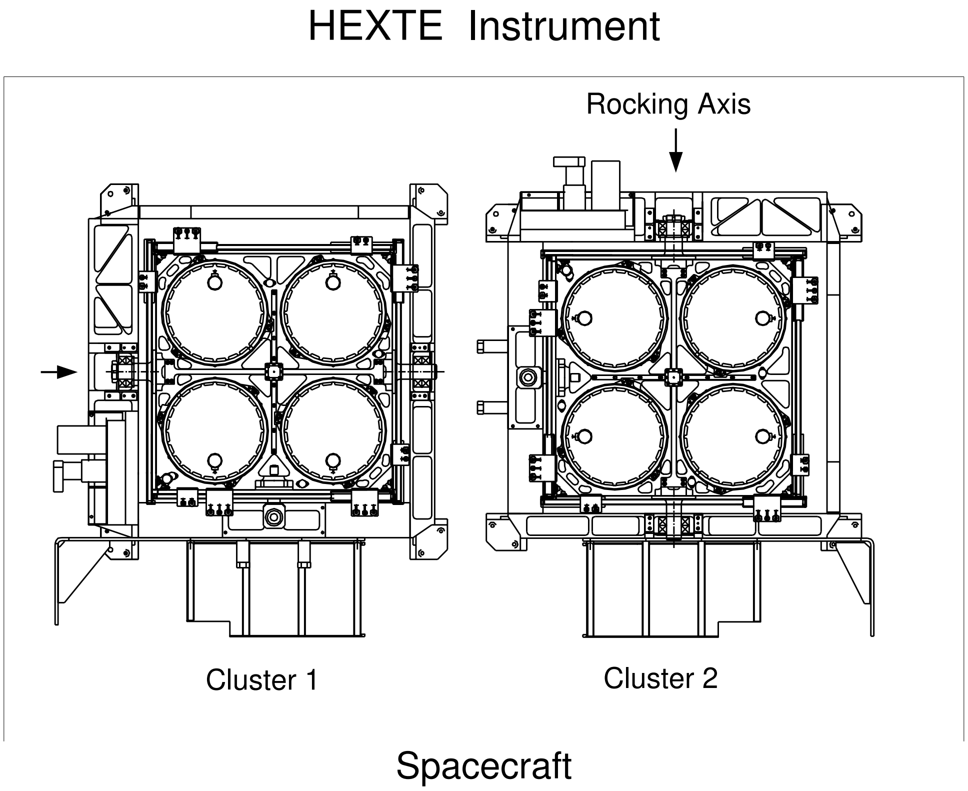

Figure 2.3: The positions of the HEXTE Clusters with respect to the spacecraft shown down the viewing axis of the instruments. The bulk of XTE lies below the bottom of the image (see also figure 2.1).

The low background counting rate in HEXTE, which is vital for studying faint sources, is kept low due to the particle shields, the design of the Phoswich detectors and the selection of the orbit. The particle shields are four active plastic scintillation detectors which form a four sided box perpendicular to the viewing axis [Hink *et al.* 1991]. The particle shields lower the background rate in HEXTE by $\sim 1/3$ by vetoing events that occur due to energetic cosmic or geomagnetically-trapped charged particles passing through the detector. Each cluster contains a small plastic scintillation detector, called the particle monitor, that monitors the charged particle environment of the spacecraft and puts the detectors into a safe state when the charged particle flux becomes too intense. XTE makes eight daily passages through the South Atlantic Anomaly (SAA). The SAA is a region of the earth's magnetic field which is populated by trapped particles at the altitude of XTE's orbit(see section 2.3.2).

2.1.1 Detectors

The phoswich, short for phosphor sandwich, scintillation detectors consist of a Sodium Iodide (NaI) detector joined typically to a Cesium Iodide (CsI) detector which acts as a shield. The detectors each have an effective area of ~ 200 cm^2. The CsI shield can be looked at as the fifth side of the particle shield box (section 2.1). The scintillators emit visible light when excited by x-rays, γ-rays and energetic particles. The light from the scintillators is converted to photoelectrons by the photocathode of the photomultiplier tube (PMT). X-rays that enter the detector

A HEXTE Phoswich Detector

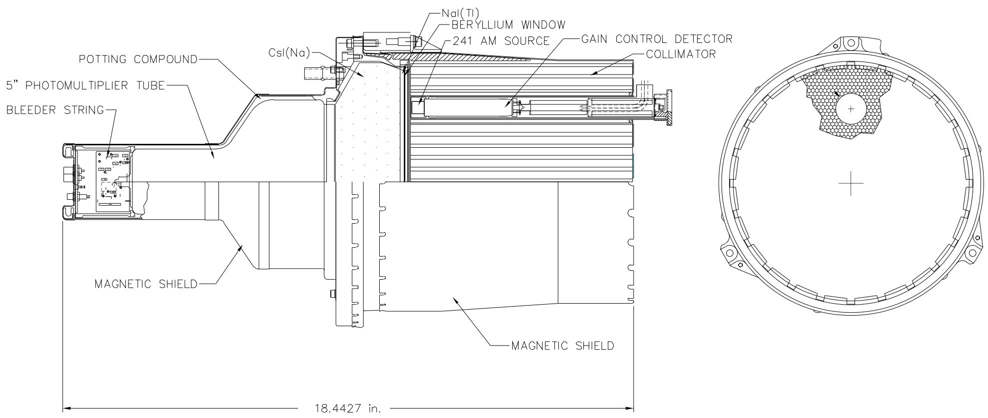

Figure 2.4: A HEXTE phoswich detector is shown with collimator. The figure on the right is shown from the instrument viewing axis with the honeycomb pattern of the lead collimator shown only in the region near the gain control detector.

are likely to give up their energy to an electron of an atom in a single event via the photoelectric effect. Events in the CsI shield can be differentiated from events in the NaI detector by the decay time of the visible light emission which is measured by the detector electronics. The CsI shield is used to veto events that do not originate in the NaI detector — events from photons that do not come through the collimator. The CsI crystal is connected to the front of the PMT which accelerates photoelectrons, created in the front coating of the photocathode by incident visible photons, with a number of high voltage dynodes. The accelerated electrons collide with the dynode and create a shower of electrons which result in a current at the anode. Changes in the voltage across the dynodes or in the ambient magnetic field cause changes in the overall gain of the system. This would translate to apparent changes in the energies of the incident x-rays. The geomagnetic field in the XTE orbit changes considerable in both magnitude and direction on orbital timescales. To counter these gain changes, each detector has a active gain control system based on the 60 keV nuclear line from an ^{241}Am calibration source [Pelling, Rothschild, and MacDonald 1991]. The detector system has an average energy resolution of 15.4% at 60 keV. Magnetic shielding [Rothschild, Pelling, and Hink 1991] isolates the PMT from changes in the PMT's orientation in the earth's magnetic field. The magnetic shielding along with the gain control system control the gain on orbit to within 0.3% on one day averages.

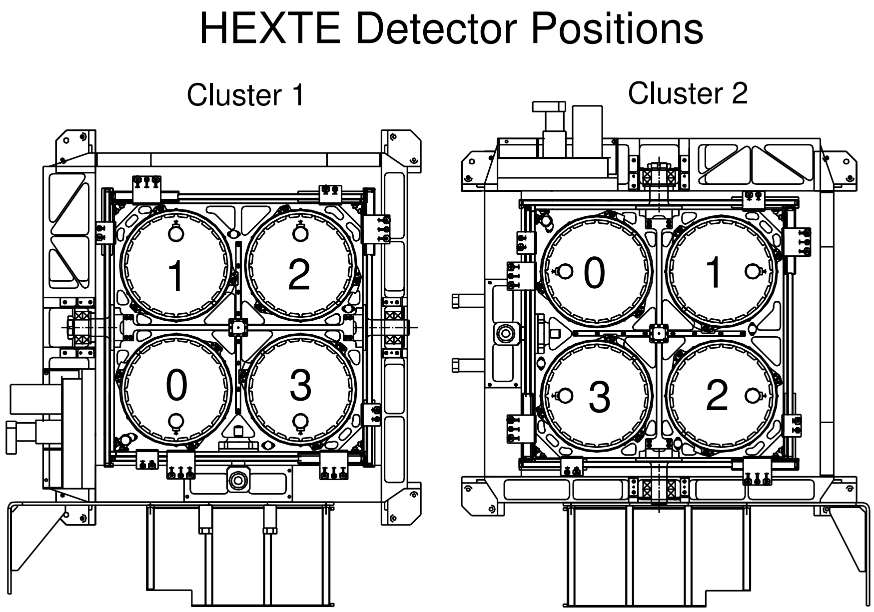

Figure 2.5: The positions of the HEXTE phoswich detectors within the HEXTE instrument are shown from the instrument viewing axis. Detectors in each cluster are numbered clockwise starting with the detector closest to the particle monitor.

The detectors are numbered within the clusters increasing clockwise if one was looking down the instrument axis towards the cluster. The lowest numbered detector is the one closest to the particle monitor. As with the clusters there are two ambiguous schemes for numbering the detectors: 0-1-2-3 and 1-2-3-4. I will use the 0-1-2-3 numbering scheme throughout. Table 2.1 relates the positions of the phoswich detectors in the instrument to their preflight designations. Due to a failure of the shaping amp in its front-end electronics, detector 2 in Cluster 2 stopped processing energy information on March 6 1996, approximately 2 months into the mission.

Table 2.1: Phoswich locations

Phoswich #	Cluster 1	Cluster 2
0	P	F
1	H	D
2	G	L
3	Q	E

2.1.2 Field of View

The phoswich detectors have hexagonal lead collimators that give a full width half maximum (FWHM) field-of-view (FOV) of $\sim$ 1 square degree. The FOV for the two clusters are shown in figure 2.6. The hexagonal nature of the FOV of individual detectors are washed out by the effect of slightly different alignments of the detectors within each cluster with respect to the viewing axis. With 7 of the 8 detectors returning spectral information, the effective areas of the two clusters for spectral work are 755 cm^2 and 584 cm^2 for 1 and 2, respectively. The properties of the individual detectors are shown in table 2.2.

Table 2.2: Phoswich Specifications

Detector	area cm^2	Field of View [a]
Cluster 1		
0	185.75	
1	192.20	
2	192.71	
3	184.56	
Total	755.22	1.11
Cluster 2		
0	200.59	
1	191.98	
3	192.41	
Total	584.98	1.08

[a] in square degrees

2.1.3 Aperture Modulator

The HEXTE clusters have a number of on and off source chopping patterns. The one that is useful for the background fluctuation measurement is the default two sided rocking mode which is used except for very strong sources and where there is a serendipitous source in one of the background FOVs. As shown in figure 2.7, each cluster alternates between an on-source position and two off-source positions, one on each side. The two clusters are offset 90° in rocking phase, as well as the 90° offset in position (figure 2.8), so that there will always be one cluster pointed at the source. The time for the cluster to move from one position to another is taken

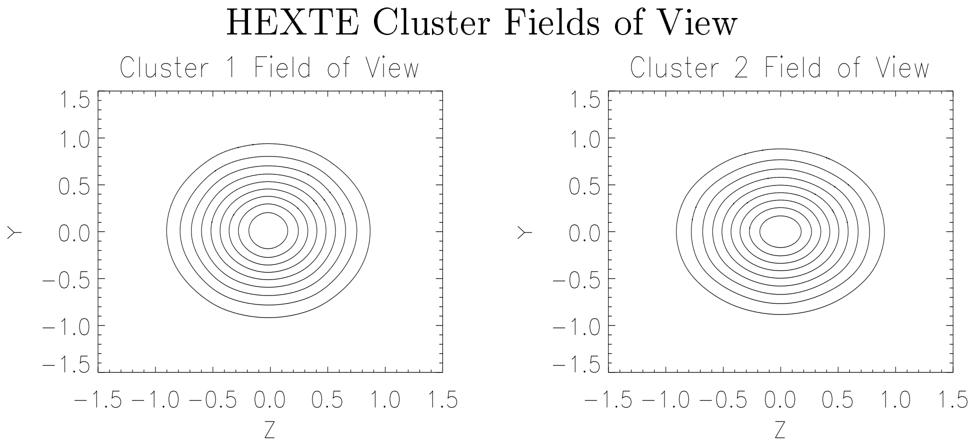

Figure 2.6: The figure on the left is for the four detectors in cluster 1 and the figure on the right is for detectors 0, 1 and 3 in cluster 2. The axes are in degrees in spacecraft coordinates (see figure 2.9). Detector 2 in cluster 2 failed early in the mission and is not used in this study. Shown with 10% contours, the FWHM of the clusters are 1.11 and 1.08 square degrees respectively.

during the background time so that it is 4 seconds shorter than the on-source time. The rocking intervals can be set at 16, 32, 64 or 128 seconds, but all of the data has been taken with 16 or 32 second rocking. The faster timing intervals sample the instrumental background more quickly and better approximate background changes on faster timescales. The center of the off source fields-of-view can be either 1.5 ° or 3.0 ° from the on source position. Fortunately, the vast majority of the data is taken with the 1.5 ° rocking. This mode is better for the XRB measurement since it minimizes the smearing of the field of view.

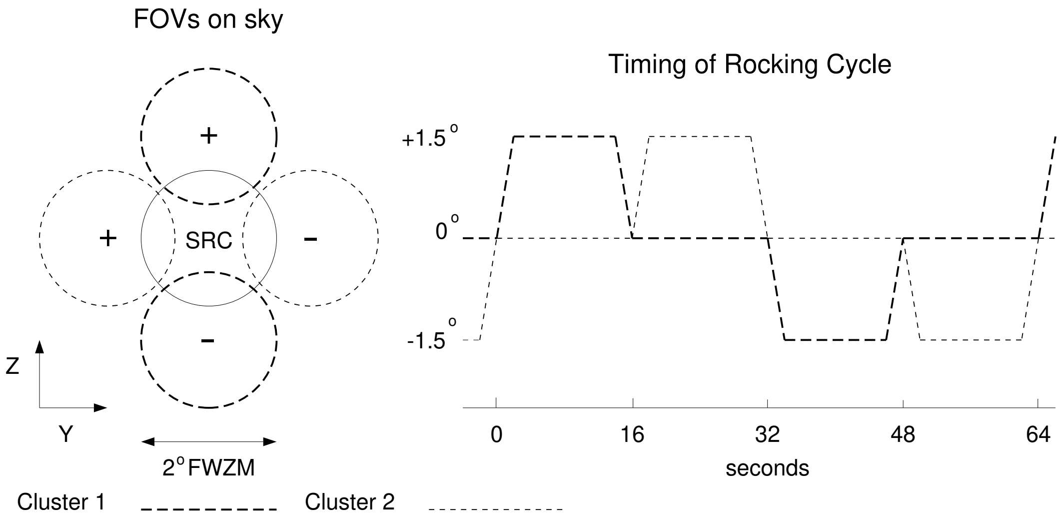

Figure 2.7: The figure on the left is the fields of view on the sky of the source and off-source positions for the two clusters in spacecraft coordinates. The 2° Full Width Zero Maximum (FWZM) fields of view are shown. The figure on the right is a timing diagram for the rocking cycle in the 16 second rocking mode.

2.1.4 Smearing

The XTE spacecraft has one axis, the Z axis, that is always pointed approximately in the direction of the sun (see figure 2.9). The HEXTE and PCA instruments point in the X axis. The HEXTE clusters 1 and 2 rock in the ± Z and the ± Y directions respectively (figures 2.7 and 2.8). As the angles between a particular source and the sun change during the year, the locations of the background positions rotate in spacecraft coordinates. This rotation smears out the background field in time and increases the effective FOV for the background measurements. The extent of this smearing depends on the position of the source and the specifics of the observation schedule of the source. Figure 2.10 contrasts an observation with almost no smearing and one with a substantial amount. The two observations have approximately the

Motion of HEXTE Clusters

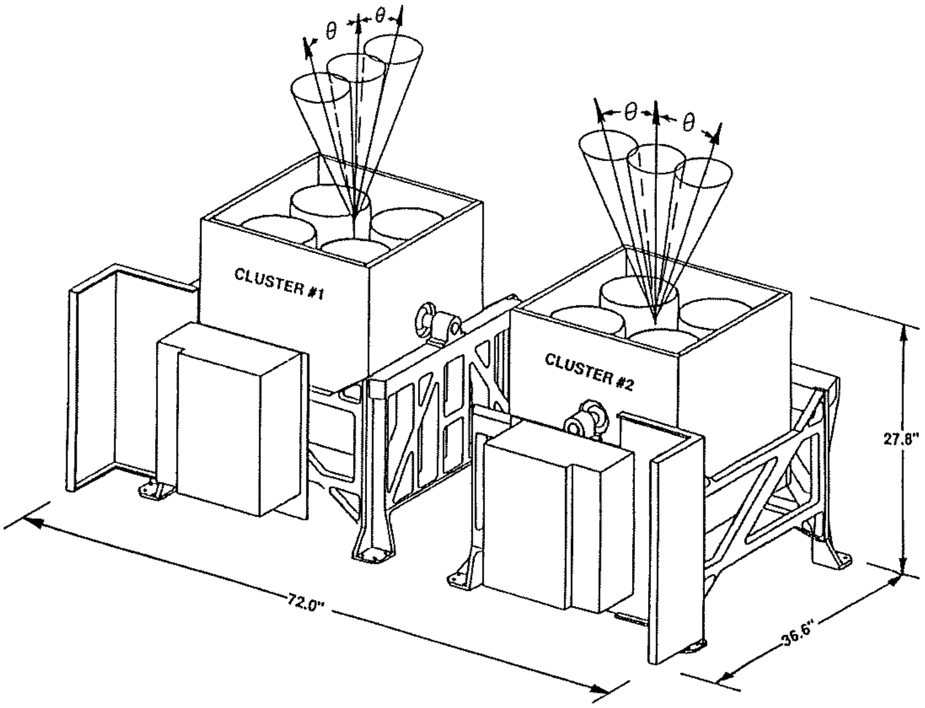

Figure 2.8: HEXTE clusters with on-source and off-source fields of view. The timing of the on and off source pointing is shown in figure 2.7.

same livetime. Since the fluctuations expected in an observation depend strongly on the field of view (chapter 5 introduction), it is necessary to compensate for this change in the FOV in the analysis (section 3.1.3).

2.2 Observing Plan

No XTE observations were expressly scheduled for this XRB investigation, but I observe parasitically (or symbiotically) on the backs of other XTE observations. The observations for the XRB measurement are taken as part of the internal background

XTE Spacecraft Axes

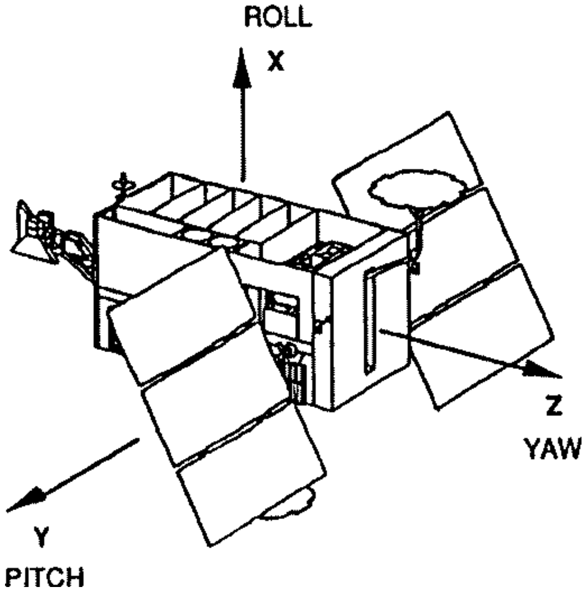

Figure 2.9: XTE spacecraft with spacecraft axes marked. HEXTE instrument is to right in image between the solar panels. The positive X axis is the viewing axis for HEXTE and the PCA.

subtraction for other observations. We have the rights to the data from the off source positions of all the XTE observations that are longer than 50k seconds. (see Appendix A). Additionally, we have 5 minute PCA observations of each of the HEXTE background fields for these observations in order to help identify any contaminating sources.

2.2.1 Contaminating sources

There are several types of sources that are considered to be contamination. First there are known x-ray sources, which are considered part of the foreground and must be removed. Two of the observed fields in this study, even though they are outside

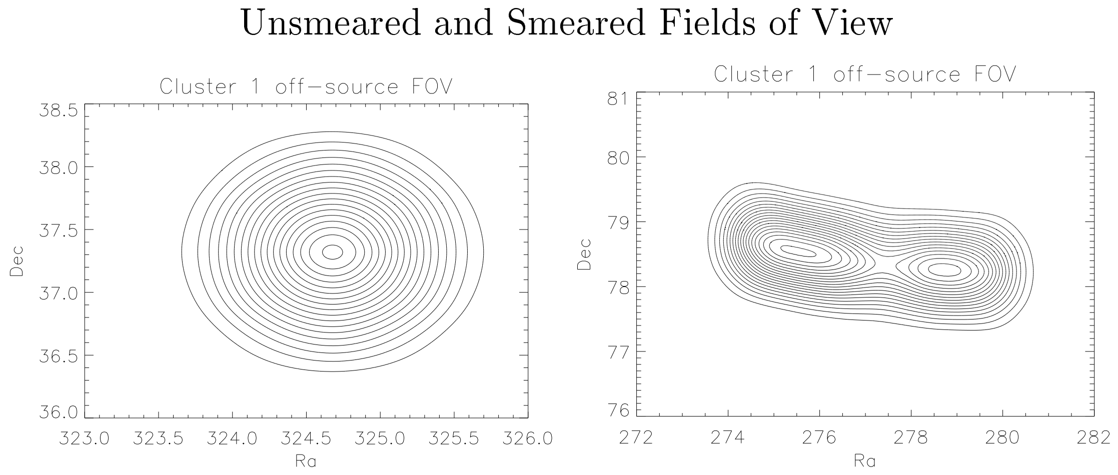

Figure 2.10: The figure on the left is a 100ks observation of cyg x-2 which has essentially the ideal instrument FOV. The figure on the right is a 145ks observation of 3C390.3 which has ~ 5 times the ideal FOV. Both figures are the off-source + background field for cluster 1 and use 5% contours.

of the galactic plane, have known sources in their background fields. There will also be unknown sources that happen to be in the field of view of the observation. The galactic plane can be considered a large source that must be avoided. Since the XRB is partly or completely composed of discrete sources (section 5.2), the separation of the foreground from the background is dependent on the sensitivity of the instrument performing the observations. Differentiating sources to be considered part of the foreground from the background is discussed in section 3.2.1.

The known and unknown isolated sources are removed by simply eliminating their observations from the analysis. The galactic contribution is removed by eliminating all observations that take place within the galactic disk or the bulge. All observations within 10° of the galactic center and all observations with galactic latitudes of less than 4° are eliminated.

2.2.2 Selection

When the contaminating sources have been removed, we still have a huge database of millions of seconds of data. There are several constraints used for selecting suitable data from this database. As just described, we exclude the galactic bulge and the galactic disk to avoid confusion with the numerous galactic x-ray sources and the diffuse galactic emission. We look for sources, known or unknown, in the background FOVs and we have to be aware of and compensate for excessively smeared observation (see section 2.1.4).

In some cases the observations of a particular source have been taken at widely different times. In these cases the background fields have rotated enough so that the fields of view of the different sub-observations are independent. In this case we can use subsets of a particular observation as separate measurements since they are sampling different, separable areas on the sky. The observation of NGC 4151 (figure 2.11 is an example of a monitoring campaign that can be divided into four independent background observations since the background FOVs are independent.

2.2.3 Scheduling

The XTE spacecraft has flexible scheduling to allow for both observations of transient sources and for monitoring of sources over long periods of time. This flexibility

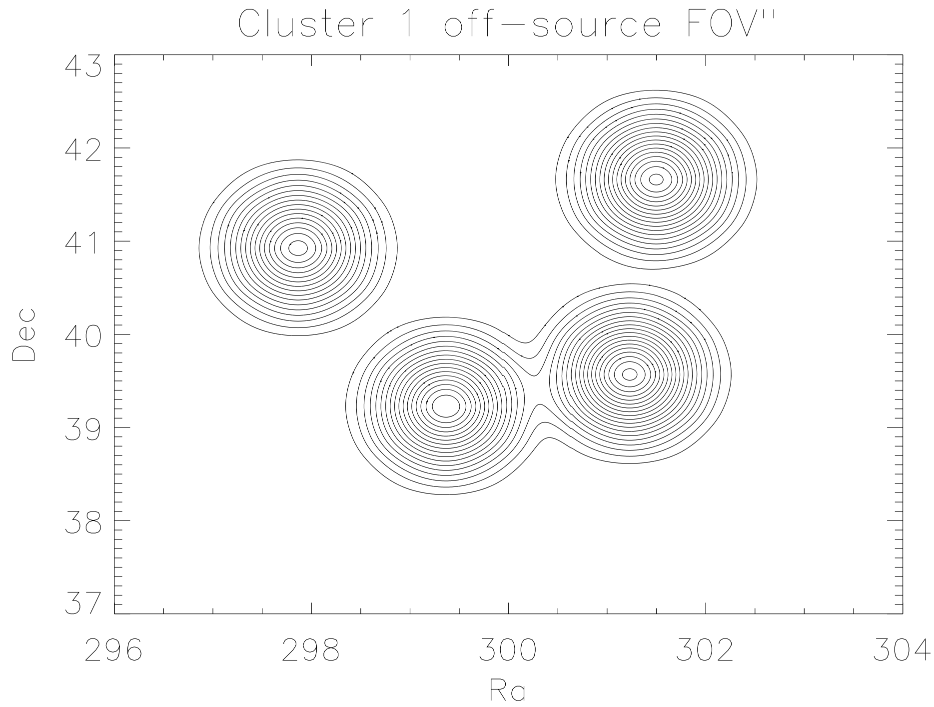

Figure 2.11: Observation of NGC 4151 with sections separated enough spatially to be divided into four independent sub-observations. Off-source + background field for cluster 1 is shown using 5% contours.

in observations causes complications for the analysis of our parasitic data. All of the observations that are long enough to be useful for the background measurement are divided up into several observations at different times. The total time elapsed between the start and end of an observation can be as short as a few days or as long as the entire mission. This results in the necessity to divide observations and in the smearing discussed in section 2.1.4. Different sub-observations may also have different science and rocking modes as well as different instrument settings such as different lower energy thresholds (see section 3.1.3). Different investigator's observations of the same source can often be combined if they use the same instrument settings.

2.3 Data

There are a number of different types of data packets that are created by the XTE spacecraft and the instruments on board. The packets necessary for HEXTE data processing and their application identification numbers (apid)s are listed in table 2.3. Two types of packets are created by each of the HEXTE clusters: one contains housekeeping data, such as temperatures and calibration information, and the other science data, which consists of events, livetimes and instrument settings. These packets along with several types of spacecraft housekeeping packets containing position and pointing information are used to select data of appropriate modes for our analysis. The packets are transmitted on different time scales. The most impor-

Table 2.3: Selected XTE data packets

apid	Contents
	HEXTE Instrument
80	Cluster 1 Science data
83	Cluster 1 Housekeeping data
86	Cluster 2 Science data
89	Cluster 2 Housekeeping data
	XTE Spacecraft
1	Status
14	Attitude
17	Config Status
21	Command and Aberration
24	Statistics and Ephemerides

tant timescale is the 16 second instrument data frame (IDF) which is the timescale that the housekeeping data packets are sent and the timescale that the livetime corrections can be made (see section 2.3.3).

2.3.1 Selection

As briefly mentioned in the observing plan (section2.2.2), the observations we used were selected from the 36.7 Ms database of long XTE observations based on several different criteria: The position of the source, the length of the observations and known contaminating sources. There are also a number of environmental and instrumental effects that had to be taken into account when selecting the data from a particular observation: South Atlantic Anomaly (SAA) passages, earth occultations, instrument modes, transmission errors and missing data. After all the observational losses have been excluded we are left with 12.7 Ms of observations.

2.3.2 Operational Losses

Table 2.4: Orbital Environment Losses

Source	% loss
Predicted Earth occultations and SAA passages	31
Corrected Earth occultations	12
Galaxy	35
Field rotation	5
Missing data	< 1

Table 2.4 gives the approximate fraction of data lost from orbital effects. Earth occultations occur when the earth is between the spacecraft and the source. This is about 40% of the orbit for objects close to the ecliptic plane. The SAA is a region where there are a large number of trapped charged particles at the altitude of XTE's orbit. (Section 2.3.3 deals with the effects of charged particle events on the HEXTE detectors.) The flux of charged particles in the SAA is so high that the instruments on the spacecraft have to be shut down to avoid damage. XTE travels through the SAA 8 times in the typical day. Figure 2.12 shows the particle monitor rates for a typical day. The charged particles During these SAA passages create

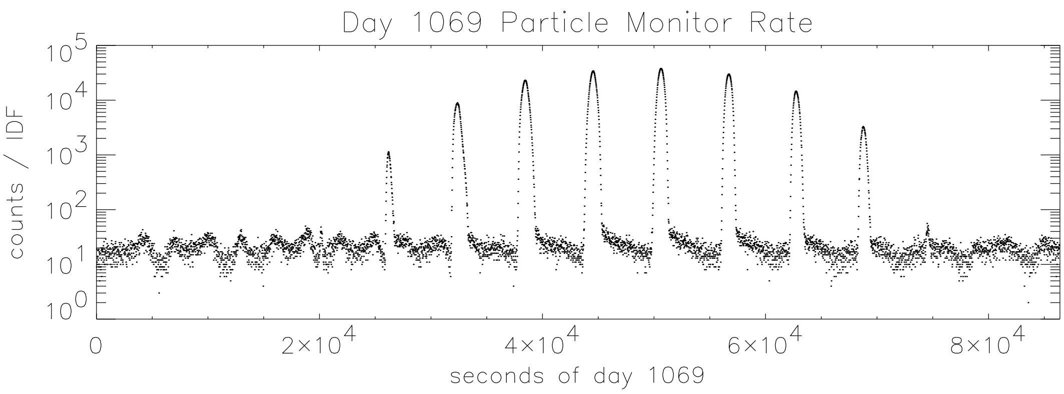

Figure 2.12: Particle monitor rate for day 1069. The eight SAA passages can be seen by the large jump in flux. The passages can also be seen as the data gaps in figures 2.13 and 2.14 Orbital variations in flux can also be seen as the waving baseline during non-SAA orbits.

radioactive elements inside the HEXTE detector. One of the most prominent is ^{125}I which has a 25 minute half-life. The decay of this element can be seen in the rates immediately after the SAA passages (figure 2.13). The increase in count rate during the 90 minute orbital period can also be seen in the non-SAA intervals. There were

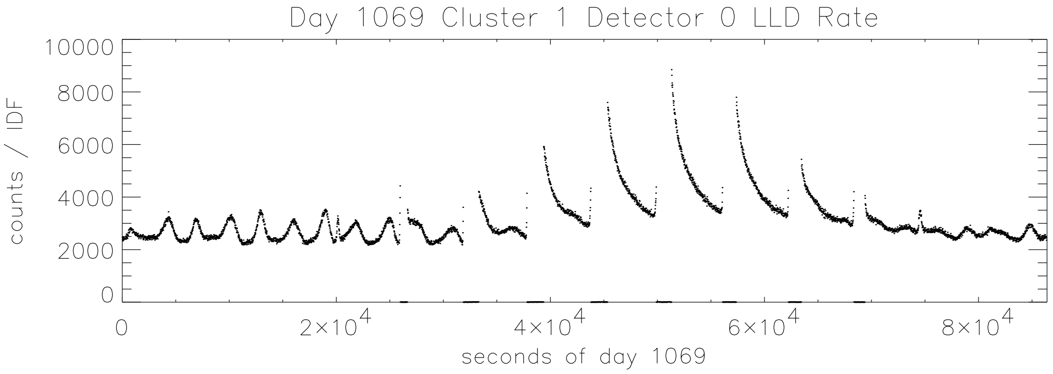

Figure 2.13: Lower energy threshold rates for day 1069. Orbital variations in the environment of the instrument can be seen as the variations in the baseline of the non-SAA orbits. The radiation induced in the detectors by the SAA passages can be seen decaying after the instrument is turned on.

two different observations taken during day 1069. The first observation taken during the first four hours of the day was a galactic source GRS 1915. The rest of the day was spent observing LMC X-3. In figure 2.14 of the good event rates for day 1069, the efficiency of the HEXTE background subtraction can be seen. The two lines in the figure are the on-source and the off-source event rates in the instrument. The difference between the lower (off-source) line and the upper (on-source) line is the source flux. GRS 1915 is brighter in the HEXTE energy band than LMC X-3 so the separation between the lines is greater at the beginning of the day. The source flux can be seen to be constant on the timescale of the changes in the internal noise such as the times when the instrument is recovering from SAA passages.

Table 2.5 shows the different HEXTE instrument science modes. The vast majority of the data has been taken in Event mode, which is the mode that is used

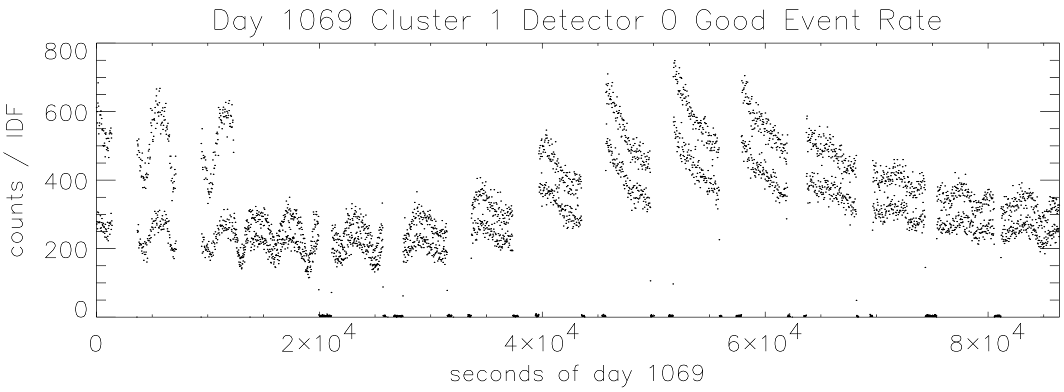

Figure 2.14: Good event rates for day 1069. The source flux can be seen as the difference between the low and high points at any time. The source observed for the first 4 hours of the day is brighter than the source in the second observation. The source flux is seen to be constant even during high internal background intervals after SAA passages. The differing fluxes throughout the day are due to the fluxes in the sources observed.

for the XRB study. There have been very few times with significant missing data

Table 2.5: HEXTE Science Modes

0	Idle Mode
1	Event Mode
2	Histogram Bin Mode
3	Multiscaler Bin Mode
4	PHA / PSA Mode
5	Not Used
6	Burst Mode
7	Diagnostic Mode

from the spacecraft but small data loss intervals must be removed from the science data since livetime can still accrue and change the apparent source fluxes in these intervals. There are known times of losses of a few 16-second instrument data frames (IDFs) worth of data such as when commands are sent and at the beginning of the day. Losses of more than three IDFs at a time are very rare.

Table 2.6: Instrument Mode and Positional Losses

Source	loss
High LLD Setting	150 ks
Unusable rocking mode	1013 ks
3.0° rocking mode	234 ks
Contaminating sources	
Cluster 1	97 ks
Cluster 2	69 ks

Table 2.6 shows the observation time lost due to different instrumental effects. The Lower Level Discriminator (LLD) sets the lowest energy events to be processed by the instrument. Observations with differing energy limits would cause statistical problems and most of the signal is in the lowest energy bands, so observation with high LLD settings are removed. Some observations have been taken with the Aperture Modulator turned off or in a mode where it only points off-source on one side. Both off-source positions are required for the analysis (section 3.1) so these intervals are also eliminated. The 3.0° rocking mode data is usable, it is shown to indicate that the vast majority of the data is taken with the default 1.5° rocking. There were two observations which had known sources in one of the off-source fields. One of these foreground objects was found in an off-source field of each cluster.

2.3.3 Systematics

There have been different tests performed on the HEXTE instrument by myself and others to understand the limits of the systematic effects introduced into the data by the various subsystems (section 3.4). The only corrections that have been generally made have been to empirically correct for several different deficiencies in the counting of livetime (section3.1.3). The most significant problem is based on miscounting of the deadtime occurring after charged particle events which swamp the detector electronics and prohibit event processing (section3.1.3).

Livetime Errors

There are several well understood contributions to the problems with the livetimes recorded in the HEXTE instrument. The largest correction, which can be up to 40%, is due to slower than anticipated instrument recovery from events which deposit a large amount of energy in the detectors. These large events saturate the preamp electronics in a way that is not accounted for in the calculation of the instrument livetime. There is a function in the electronics called the XULD window, which is a programmed deadtime after each of these large events to allow for recovery but the electronics take longer to recover than the window allows for and a correction must be made in the analysis software (see section 3.2.2). The majority of the events causing these large energy losses are cosmic rays or charged particles that are trapped in the earth's magnetic fields. The changes in the fluxes of these particles as the spacecraft orbits and changes its geomagnetic latitude can be seen as a wobble in the flux rate in figure 2.12.

2.3.4 Resolution

The nominal energy resolution of the HEXTE instrument is 15 % at 60 keV and is much smaller than the wide energy bins that are necessary for the present analysis due to the small signal in the fluctuation measurements.

Chapter 3

Analysis

The analysis of the HEXTE data was comprised of several major parts: selection of the data, which has been looked at from an instrument perspective in section 2.2.2, testing for and measurement of systematic errors, abstracting the useful information from the data and creation of software to perform all of the preceding tasks. The different elements of the analysis were not independently performed as presented but rather the analysis grew as systematic effects were discovered and removed and layers of complexity were added to the analysis.

3.1 Method

The first step in the analysis was the collection of spectra for each source observation, summed from events during all the time that the spacecraft was pointed on source and was in the correct configuration. Spectra were collected for the three different pointing directions: the on-source and the two off-source positions. The data from the on-source position is not relevant to this analysis, since the goal is to extract the differences between the off-source positions. This data is available in a raw form as packets from daily network downloads. There also needed to be a method to select data intervals, or more to the point, to remove problematical time intervals (see section 2.3.1). As a part of HEXTE system testing, software was developed which operated on the raw packetized data. After launch this software and the raw data became the packet data archive.

3.1.1 Packet Data Archive

Due to the large volume of data to be analyzed, the unavailability of tools and the several month time delay for receiving the guest observer data, which arrived in a completely different format (the Flexible Image Transport System or FITS), all of the data processing has been done using the packet data archive (PDA).

The archive is created at UCSD by daily transfers, over the net, of the raw data packets from the satellite data stream from computers at Goddard Space Flight Center (GSFC), where the XTE control center assembles the individual packet archives. The HEXTE portion of the archive is transferred to weekly CD-ROMs and benefits from the most efficient and, most importantly for this work, automatable software for data extraction.

3.1.2 Packet Data Archive Extraction Software

The extraction of data from the archive, like Gaul, is divided into three parts. These are: first the depacketizing of all of the packet data from an observation; then the identification of the usable data intervals; and finally, the creation of one or more summed spectra of the selected intervals. These summed spectra are the basic elements of the XRB analysis (see figure 3.1).

For each day since the launch of XTE, a log file has been made that details, almost correctly, each of the observations made during that day. This file is called an obscat, short for observation catalog. These files detail the parameters of the observations, including modes, pointing and the orbital events, such as earth occultations and SAA passages during the observations. But the obscats are sufficiently unreliable in their timing of these events that they are only used to determine the start and stop time of each observation.

For each observation which meets the selection criteria in sections 2.2.2 and 3.1.3 a program, scanh, extracts the observation information and builds a list of start and stop times of the observations. This information is then read by another program, good, which creates a shell script with the postfix .good to extract all the necessary information from the archive.

The good script executes the playback tools, a package of software originally created for instrumental checkout, that service the packet data. The programs

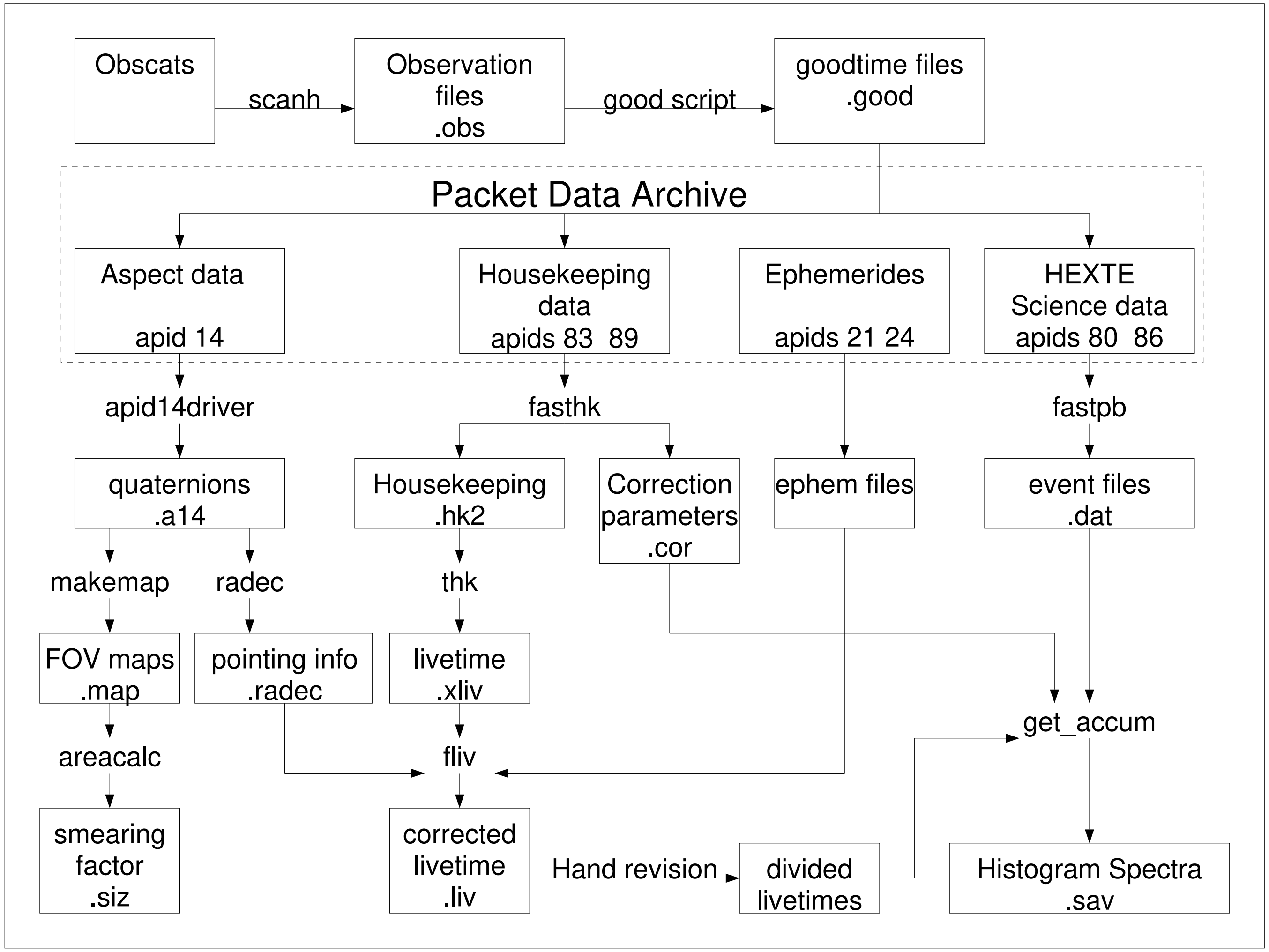

Figure 3.1: A flowchart of the extraction of the basic analysis unit, the summed observation spectrum, from the HEXTE packet data archive.

fasthk and apid14driver create ascii text files containing subsets of the instrument status, pointing and livetime correction information from the archive. The fastpb program creates an event-by-event data file which includes the raw livetimes that are used in the last step of the extraction. The details of the execution the analysis software are discussed in appendix B and a flowchart is shown in figure 3.1.

3.1.3 Selection

The next step in the extraction is to determine which parts if any of the data for a particular observation can be used and if the observation can be divided into independent sections. Elimination of earth occultation and SAA passage intervals as well as non event-mode intervals is completely automated. Removal of other contaminating intervals is partially automated (see table 3.1).

Table 3.1: Interval Selection Criteria

Pointing and Smearing	source position background rotation remove sections divide observations
Instrument Settings	rocking mode LLD setting XULD Window
Sources	known sources

There are a number of programs that eliminate bad data intervals. They operate on the packet data archive files or on the output of the other programs (figure 3.1).

The program radec creates a file which contains the locations and variations in the sky positions of the source pointing and the positions of the four off-source pointings. (see figure 2.7). Time intervals when the spacecraft is not pointing at the source are removed. Intervals where the background locations are spatially separated enough so that they are independent are divided into different observations (see figure 2.11). Finally any short intervals that would substantially increase the smearing or would disallow division of intervals are removed.

Fasthk creates lists of different housekeeping quantities. It is used to create livetime correction files for get_accum and a file with the housekeeping values which require evaluation. This housekeeping file is used by several of the other programs and can be evaluated by eye if necessary.

Biff Heindl, a member of the HEXTE instrument team, has created an empirical correction to the livetime errors discussed in section 2.3.3. Using extensive data collected on the Crab Nebula, a bright and steady x-ray source at HEXTE energies, he found a combination of discriminator counting rates which corrected the Crab counting rate to be constant. The correction file has all the discriminator rates that the program get_accum will use to make the "Biff" correction. The propagation of the livetime errors from this correction is discussed with the evaluation of the systematic errors in section 3.4.3.

The script thk reads the housekeeping file and creates a livetime file with intervals where the instrument is in the correct mode. The HEXTE instrument turns itself off during SAA passages and is commanded into idle-mode during times that are predicted to be earth occultations. The SAA passages are determined by the flux measured by the particle monitor, but the earth occultations are obtained from orbital predictions and can be wrong by as much as half an hour. There is no science data collected during idle-mode. Such intervals are removed from the dataset. Following SAA passages the instrument counting rate is elevated due to production of radioactive I^{125} in the detector itself with a 25 minute half-life (section 2.3.1) and there can be effects introduced into the science data from the instrument power returning in the first few minutes after the SAA passage, therefore I remove the first 5 minutes of data after exiting SAA passages. The thk script only allows data intervals where the instrument is in the event science mode. It accumulates statistics on the rocking position during the good intervals so that intervals of one-sided rocking or staring (pointing only on-source) can be eliminated.

Since the times of the earth occultations from the orbital predictions can be wrong, the actual times of earth occultations must be calculated and removed. The fliv script calculated the times of the earth occultations from the spacecraft pointing direction and the ephemerides. Since the instrument does not collect data at the times that it is predicted to be in earth occult, the additional times in occult are eliminated, but the data from the incorrect time interval can not be recovered. The amount of time lost to these orbital prediction errors is large $\sim$12% of the observation time (see section 2.3.2).

The state of the XULD window and the LLD setting are accumulated, but they are not used to automaticly eliminate any intervals at this point. The state of the XULD window, which has had three different lengths during the mission : 300, 500 and 2500 μs, can be used to eliminate some data, but it has not been seen to be a significant contaminating factor in the results. The few observations with raised energy threshold settings have been removed by hand. This represents only $\sim$ 150 ks of data (see section 2.3.2).

Observations that have short resulting time intervals are accumulated, but some are eliminated later in the fluctuation analysis since very short intervals have large statistical errors and reduce the significance of the final result (see section 3.3.2).

After the final intervals have been chosen for a given observation, an exposure map, a map of the instrument response is calculated from the pointing and rotation information and the collimator responses (e.g., figure 2.10). This map is used to calculate how the field of view compares to the ideal instrument FOV — how smeared the observation is. After trying a number of different measures of the smearing in these intervals, the full width at half maximum (FWHM) appears to be a good compromise between oversensitivity to low response extended wings of the map and overemphasis of separated maxima. The FWHM is also quick to calculate. Since the fluctuations are proportional to the square root of the field of view (section 5), the smearing factor, is used to correct all the data to the same FOV as the model for fitting (section 3.3.1). The flux for a measurement is multiplied by the square root of the smearing factor. This corrects the flux to that for the ideal instrument FOV.

3.2 Sky Coverage

Since no observations were scheduled for this project, the locations on the sky for the various observations used in this study follow objects of interest in the sky (Figure 3.2). This means that the selection of the regions for the background observations are essentially random. Observations in the galactic bulge and the galactic plane have been excluded to remove contamination from galactic distributed radiation. [Valinia and Marshall 1998] When the galaxy is removed, the remaining observations are reasonably well distributed throughout the rest of the sky (figure 3.3). The total sky observed by all of the observations is 0.11 steradians.

3.2.1 Separating the foreground from the background

A number of observations have foreground sources in one or more of the background fields. Since the background is hypothetically created by discrete sources, these bright sources can be viewed as large fluctuations in the background. Practically, sources above the detection threshold of the instrument are called foreground objects. The separation of the foreground from the background therefore requires a precise statement of this threshold. I have taken a three σ detection of a source in

Long HEXTE Observations

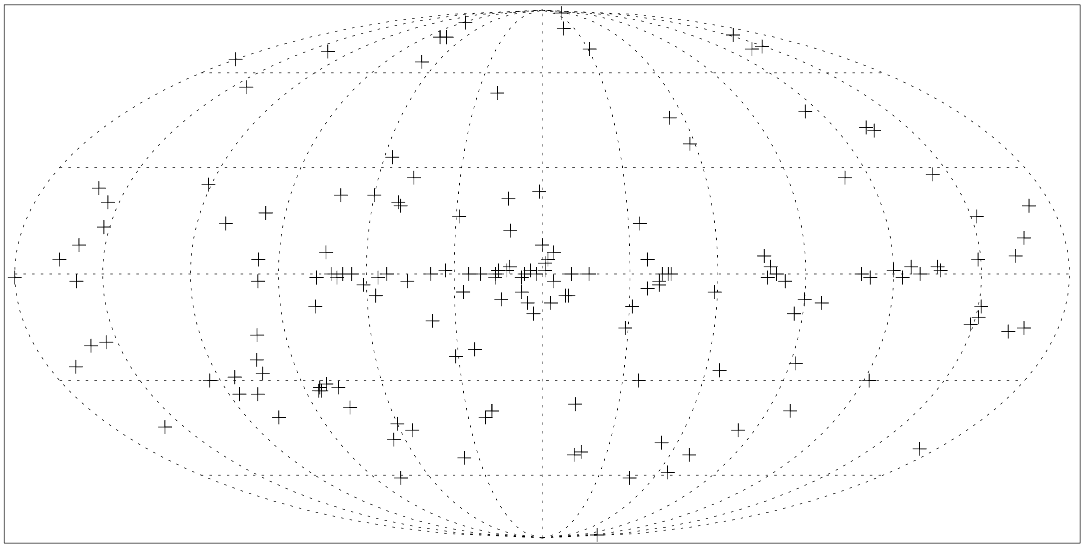

Figure 3.2: Map in galactic coordinates of the locations of all the observations in the dataset before the galaxy has been excluded.

Long HEXTE Observations Excluding Galaxy

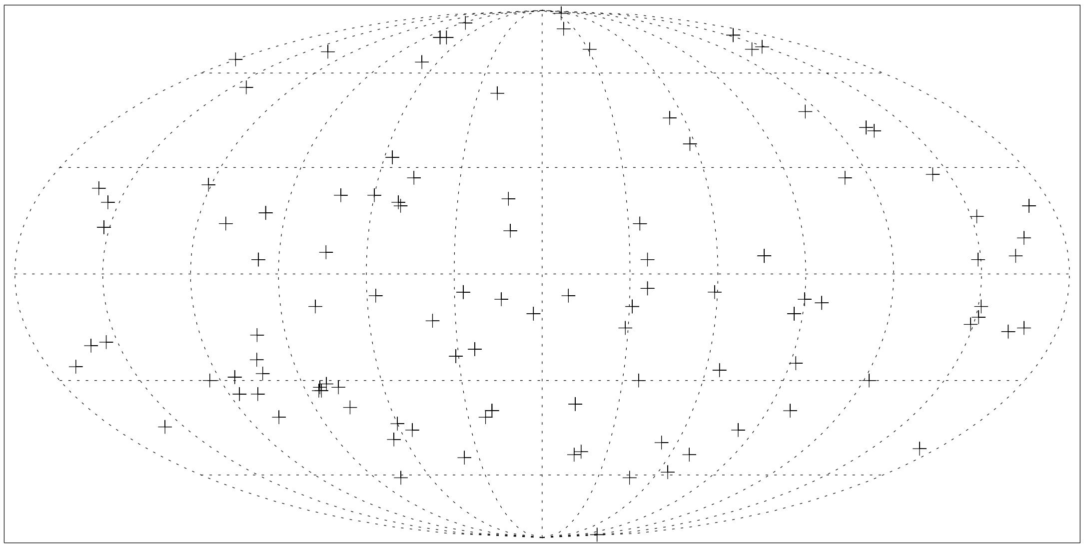

Figure 3.3: Map in galactic coordinates of the locations of all the observations in the dataset. Sources within 10° of the galactic center and sources with galactic latitude $< 4°$ have been excluded.

the shortest allowed data interval — ~ 25 ks — as the criterion for the detection of an uncataloged source. This gives a threshold flux of 0.03 counts per second per channel in channels 16–25 . This criterion is important in the calculation of the number density calculated in section 5.1.2. Using this threshold flux, there were no uncataloged sources found in any of the observations taken outside of the galactic disc. Since all known cataloged x-ray sources are considered to be part of the foreground, the three observations with known sources in one of the fields of view have been eliminated. Figure 3.4 shows a source, 4U1510-59, in the cluster 2 minus off-source field of view.

3.2.2 get_accum

The final step in the extraction of the data from the packet data archive is to create the summed count spectra from the selected time intervals. Get_accum is the IDL program which performs the actual accumulation of events and corrections to the livetimes. get_accum was created by David Marsden as a part of the instrument checkout and has grown to be the data accumulation tool for the packet data.

The output of get_accum are spectra for the on-source and off-source positions and their corrected livetimes — the histogrammed spectra. The off-source spectra and livetimes are converted into counting rates. The differences in these counting rates measure the difference in flux between the two background areas on the sky. For each observation there is a separate difference measurement for each of the

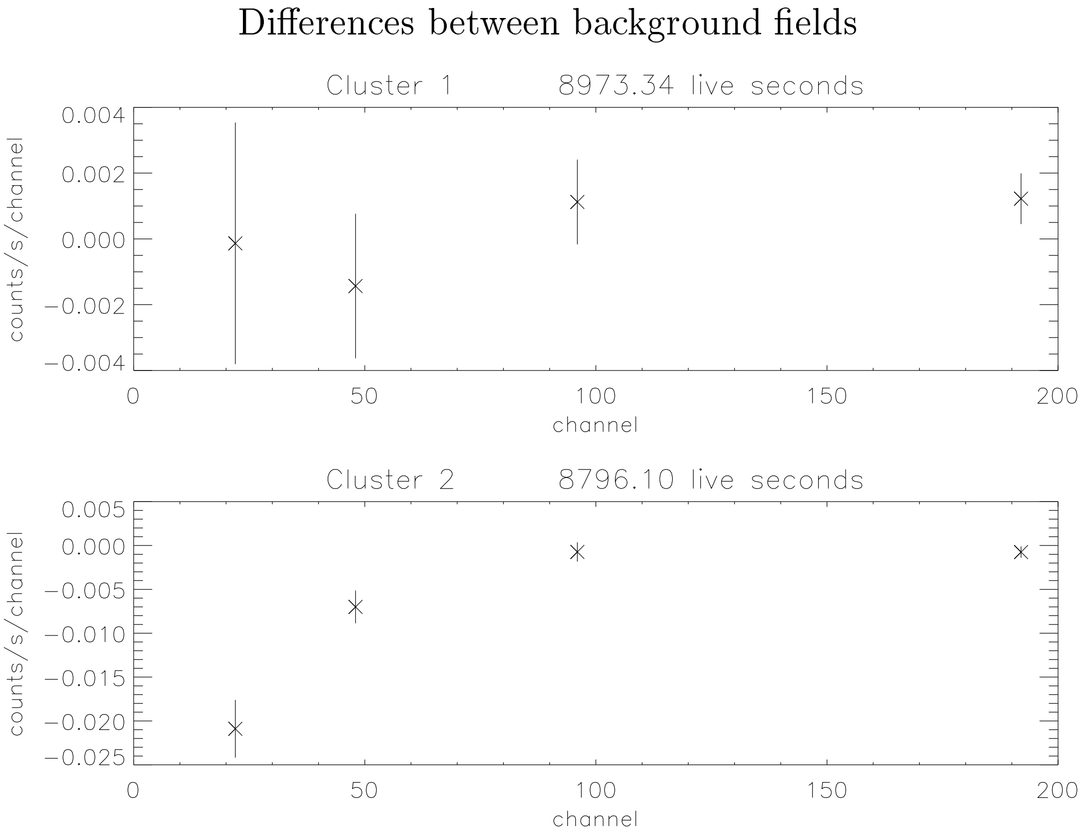

Figure 3.4: A source, 4U1510-59, can be seen in the minus off-source field of view for cluster 2. Sources in the minus off-source FOV appear as negative fluxes in the difference measurements. The energy bands shown are those used in the analysis. See table 3.2

clusters, since they have separate background FOVs (figure 2.7).

Figures 3.5 and 3.6 show spectral difference measurements for a typical length observation. The errors are larger for cluster 2 since detector 2 in cluster 2 only operated for the first few months of the mission and therefore could not be used for this analysis. This leaves cluster 2 with $\sim 3/4$ of the detector area of cluster 1 (see section 2.1.1).

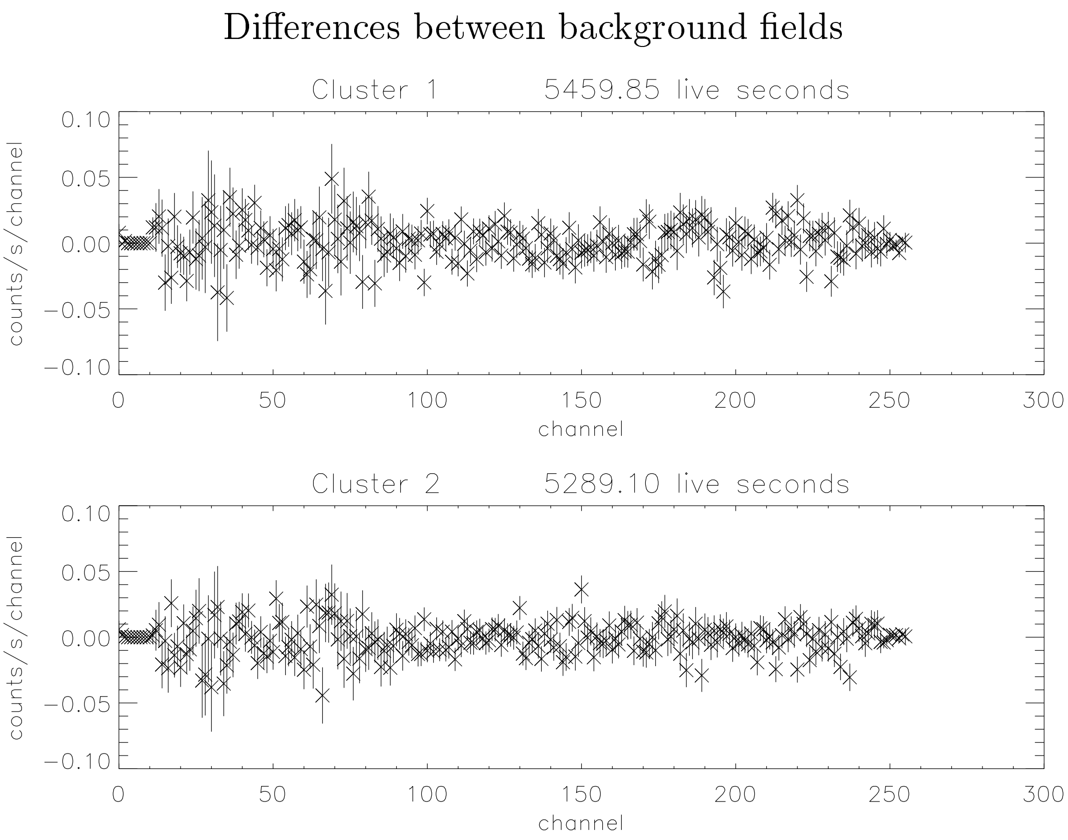

Figure 3.5: Difference between off-source-plus and off-source-minus fields for an on-source pointing towards the active galaxy mrk 279 which is a 50 ksec observation giving ~ 5 ksec net livetime in each background field with the full instrument energy resolution of 256 energy bins.

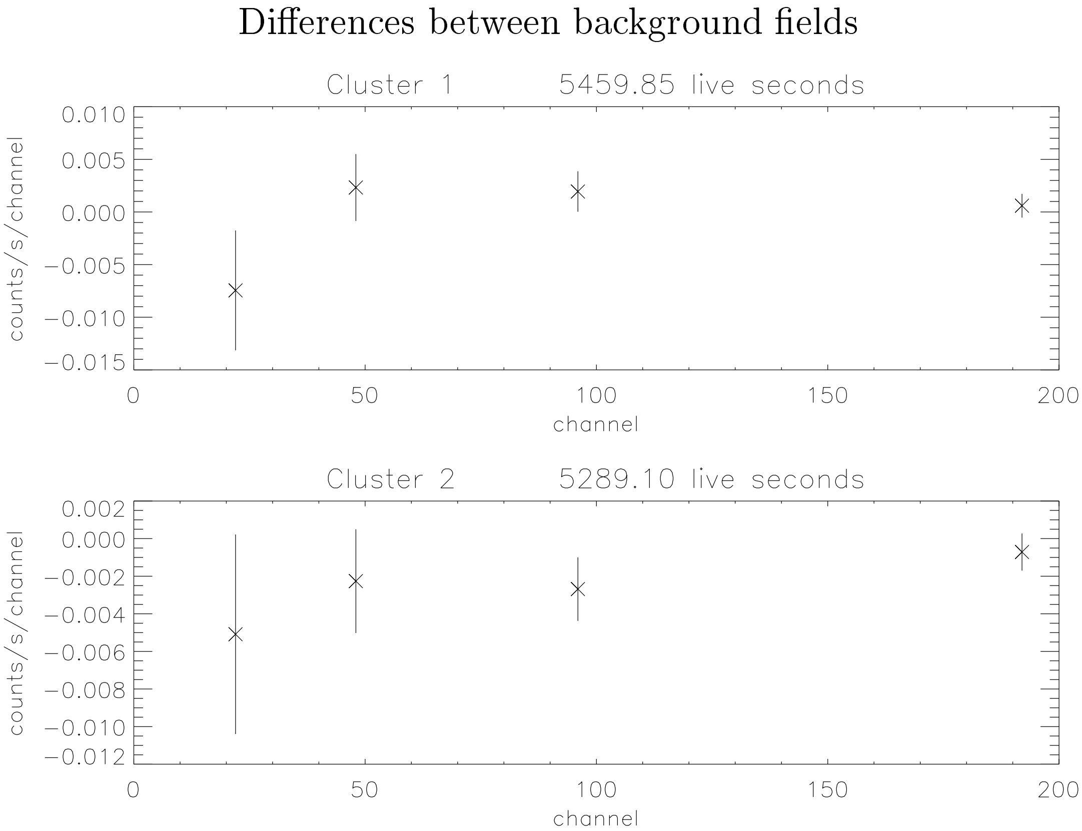

Figure 3.6: Difference between off-source-plus and off-source-minus fields for an on-source pointing towards the active galaxy mrk 279 which is a 50 ksec observation giving ~ 5 ksec net livetime in each background field. shown are the 4 energy bins used in the analysis. See table 3.2

3.3 Measuring Fluctuations

An observation has four background fields, two for cluster 1 and two for cluster 2 (see figure 2.7). If there is no source in the fields, as defined in section 3.2.1, then the flux difference between each pair is the difference in the XRB flux — a fluctuation in the XRB. For individual observations, the fluctuations in the XRB are below the sensitivity of the HEXTE instrument for any reasonable observation length (see section5.3). Although too small to be observed individually, combining observations of different sky regions allow us to measure average properties of the sky fluctuations. Since the fluctuations are small compared to the instrument noise, care must be taken to remove the noise. Using differences between off-source pointings of the same detectors subtracts out any instrumental background that varies slowly compared to the 16 to 32 second timescale of the rocking (section 2.3.2). The residual systematic effects of the rocking period is discussed in section 3.4.3.

Internal instrument background subtraction is the most important single problem to overcome in performing this observation. The expected signal is only a few percent of the instrumental background (see Table 5.2) and any systematic effects that are comparable to the counting statistics in an observation could be confused with an XRB fluctuation (see section 3.4). Figure 3.7 shows the instrumental background averaged over the entire set of observations for both clusters. The predicted signal of the XRB is compared to the instrument background rate in section 3.4.3.

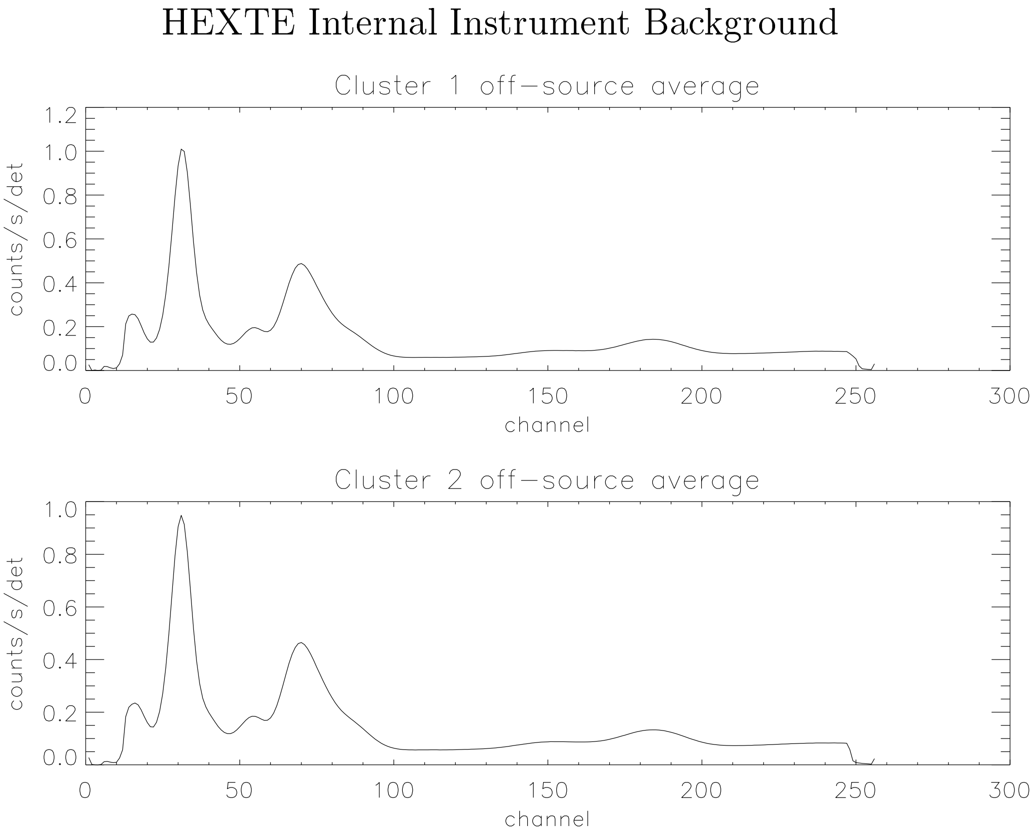

Figure 3.7: The internal background rate for a single detector in the HEXTE instrument averaged over all the observations in the dataset. The effects of the LLD and ULD can be seen below channel 15 and above channel 246.

Since the XRB signal is so small, the spectra must be binned in wide energy bands to see any signal from the XRB. The energy bands, shown in table 3.2, are chosen to avoid the large line features at 30 and 66 keV in the instrument background (see figure 3.7). Table 3.2 shows the energy bands by both their HEXTE channel range and the equivalent energy range. The first energy band is divided into two smaller bands to measure the spectrum of the fluctuations better. The entire band is used for the calculation of the number density.

Table 3.2: Channel and Energy Bands

band	channel	energy keV
1a	16–20	15.5–20.2
1b	21–25	20.2–24.9
1	16–25	15.5–24.9
2	35–41	34–41
3	81-128	80–132
4	129-245	132–261

The difference measurements always take as the off-source-plus position minus the off-source-minus position. Figure 3.8 shows the fluxes in the different energy bands for all the observations in the data set (appendix A). Each of these fluxes can be looked at as a measurement of any sky fluctuations convolved with the counting statistics of the observation and the systematic errors. To evaluate the sky fluctuation part of the signal, the fluxes have to be corrected to take into account their differing fields of view. The differing observing times of the observations is handled in the model (section 3.3.4).

3.3.1 Smearing Correction

The effect of an increased field of view is to wash out the fluctuation signal. The expected fractional fluctuation is proportional to the FOV $^{-\frac{1}{2}}$ (see section 5), which varies somewhat from observation to observation. To compensate for this effect the flux in each observation is normalized to the ideal instrument response FOV. This is accomplished by multiplying the signal by the square root of the smearing

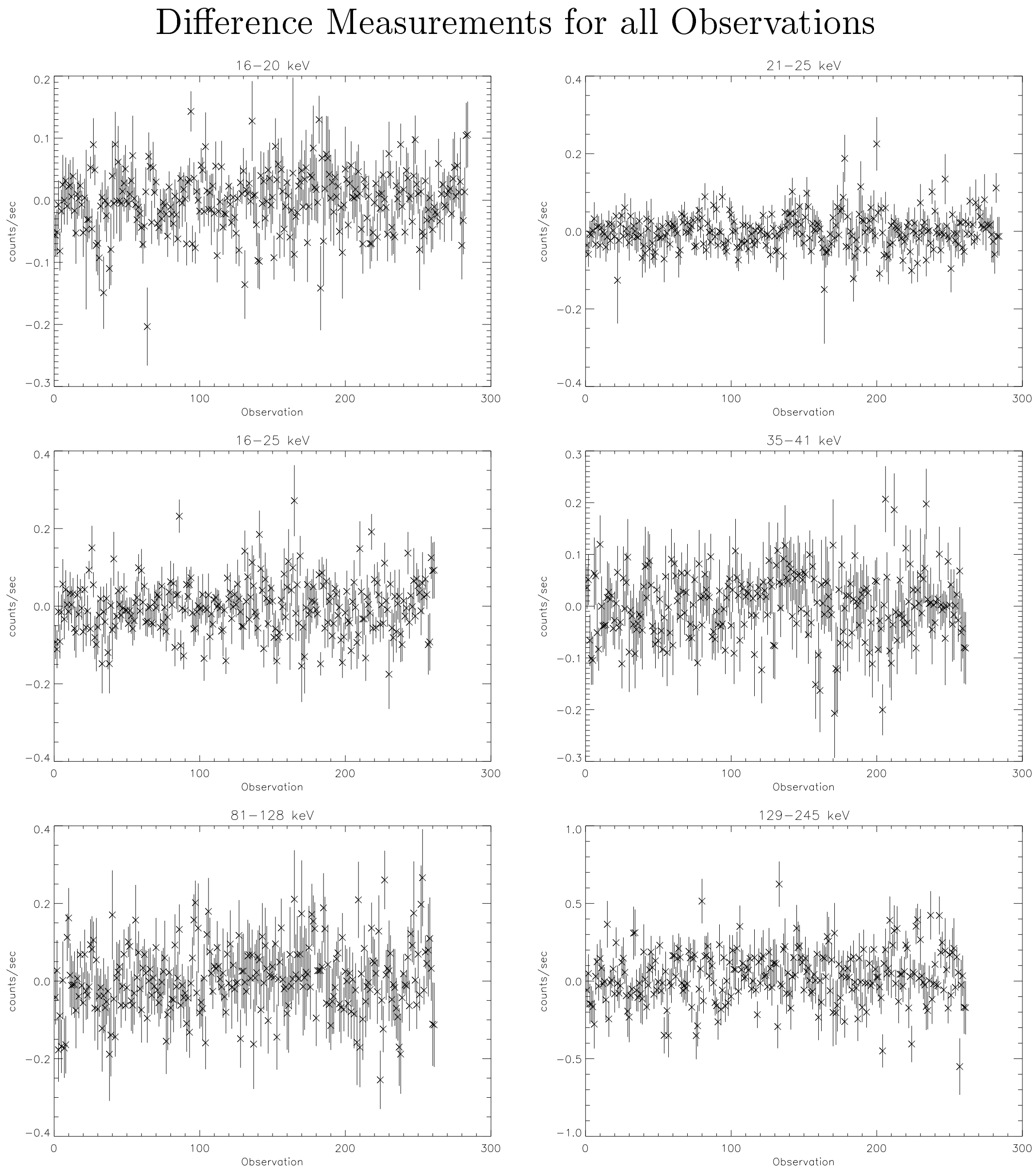

Figure 3.8: Difference fluxes for all observations in the final dataset in each of the six energy bands after the smearing correction has been made.

factor. The smearing factor is the actual FOV of the observation divided by the ideal instrument FOV. The smearing factors for each observation are listed in appendix A. The average smearing factor is 1.11 ± 0.04, thus the average smearing correction is only 5%.

3.3.2 Short Observations

Short observations have large fractional errors from Poisson counting statistics. The addition of data points with large Poisson errors leads to decreased signal to noise and essentially muddies the waters, lowering the sensitivity of the analysis. Finding the optimum lower time threshold is a tradeoff between increasing signal to noise and loss of total observing time. A cutoff of 2500 seconds of livetime in the off-source pointings has been found to give the optimum sensitivity. This corresponds to an observation time of $\sim$ 20 ks. Figure 3.9 shows the KS test probabilities for data sets with observations with shorter observing times than 2500 seconds of livetime in each background field excluded and with them included. The figure on the left has all the short observations included and can be seen to have a wider distribution with a greater probability of agreement with zero flux and at the higher end such as 0.06 counts per second. The widths defined by the 5% probability level are 0.036 and 0.0315, respectively.

Effect of Short Observations

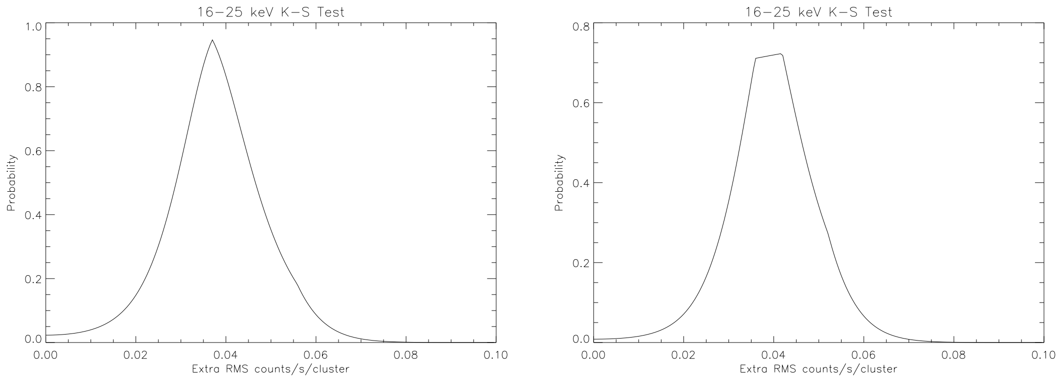

Figure 3.9: Kolmogorov-Smirnov test probability of fit of the data set to a model as a function of extra flux in the lowest energy band. The figure on the left has all the short observations included. The figure on the right is only those observations with > 2500 s livetime. The curve on the right has smaller wings and is therefore a more constraining result. The widths defined by the 5% probability level are 0.036 and 0.0315, respectively.

3.3.3 Distribution of Fluctuations

Histograms of the flux difference measurements are shown in figure 3.10. The distinction between positive and negative flux measurements is purely an instrumental effect since positive flux is any difference measurement where the flux in the off-source-plus field is greater than the off-source-minus field. This is not the same as the measurement being greater than the average flux in the background, as is true with the distributions of the fluctuations from survey missions where the average flux in the background for each data point is known and can be subtracted. This effect dilutes the signature shape of the fluctuation measurements such as in figure 5.1 by averaging it with its reverse. What we have is the symmetrical form $\frac{1}{2}(P(D)+P(-D))$. To fit this symmetrical observation of the fluctuation we make a

Histogrammed Difference Measurements

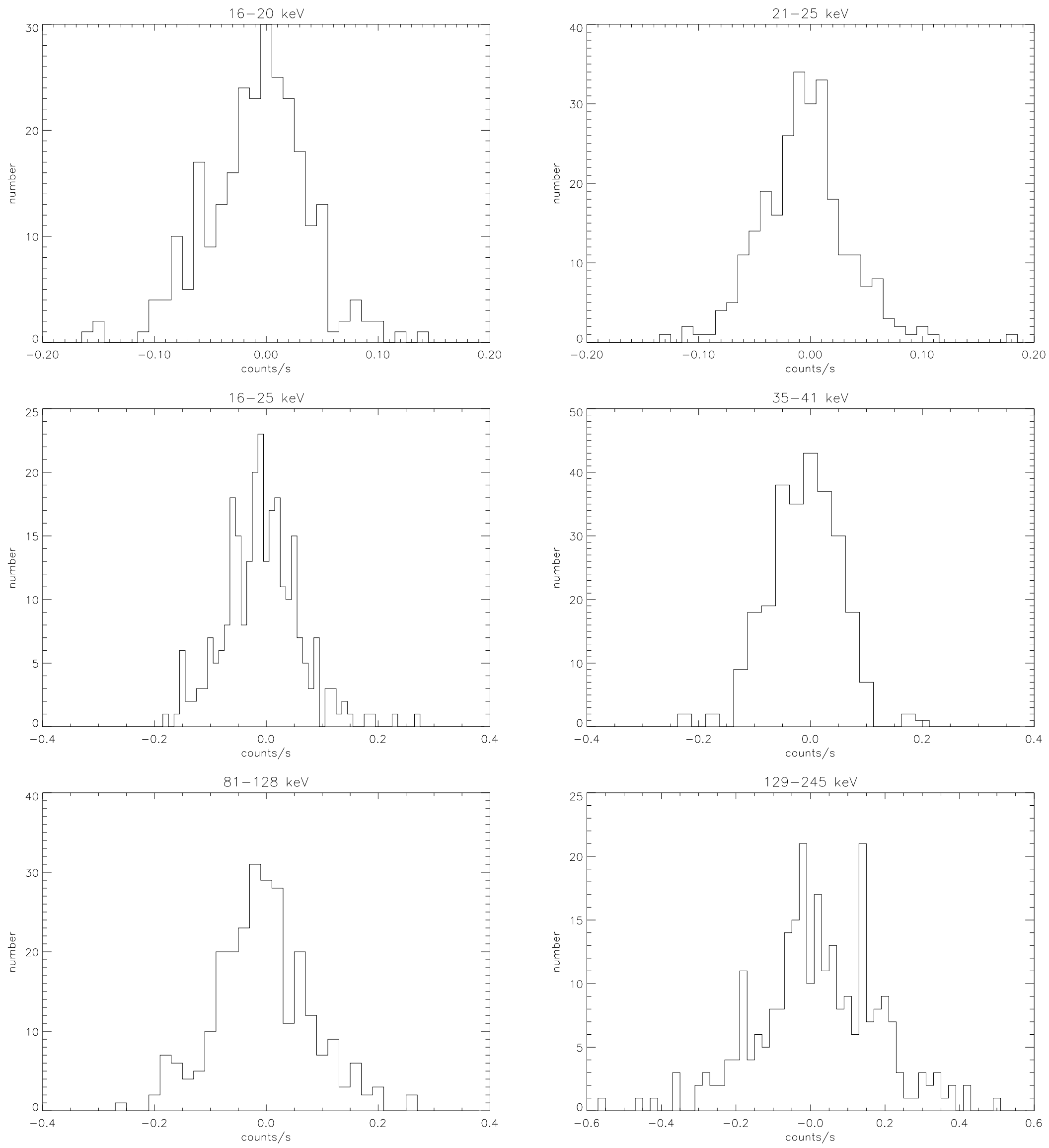

Figure 3.10: Histogram of difference for all observations in the final dataset in each of the six energy bands.

model where the observations are the sky fluctuations broadened by counting statistics. Since the count rates in the data come from counting photons, the counting statistics can be propagated through the analysis. The widths of the distributions that are due to counting statistics alone can be seen as the fit line in each panel of figure 3.11. The fit can be seen to work best in the 80–132 keV band where there is only a marginal detection of a sky flux. The systematic error contributions to the flux distribution and their removal are discussed in section 3.4.

3.3.4 Model

The measurement of the fluctuations is a comparison of the data set to a series of models. These models are created by taking the errors from the counting statistics in the data set and adding an extra width from a sky fluctuation modeled as an extra Gaussian term added to the counting errors from each observation. The probability that the data set is consistent with the model distribution is measured using two different statistical tests, the Kolmogorov Smirnov (KS) test and the χ^2 test.

The Kolmogorov Smirnov Test

The Kolmogorov Smirnov test is a way of measuring whether a two datasets, or a dataset and a model are drawn from the same distribution. They define the cumulative distribution function (CDF) which is the fraction of all the data points to the left of a given value. This function, which is by definition zero at the first

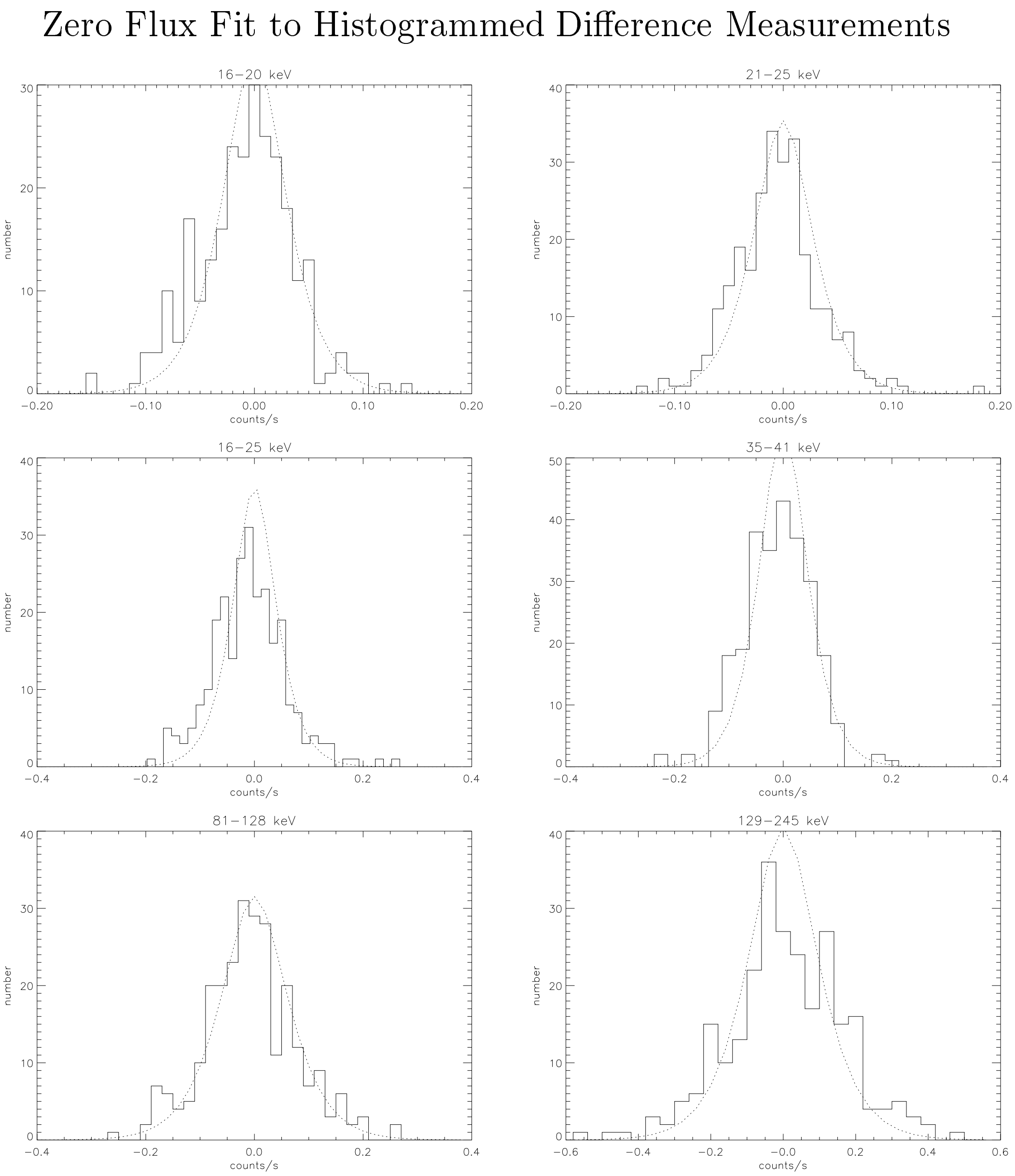

Figure 3.11: Histogram of difference for all observations in the final dataset in each of the six energy bands. The dotted lines are fits for distributions with only counting statistics and no additional flux. The zero flux fits, which may look good by eye, are shown to be bad when when compared to the best fits in figure 3.19.

data point and one at the last can be estimated from the data by sorting it into ascending order then summing. Figure 3.12 shows the ordered data for energy band 1 and the CDF estimated from the data. This CDF can now be compared to another

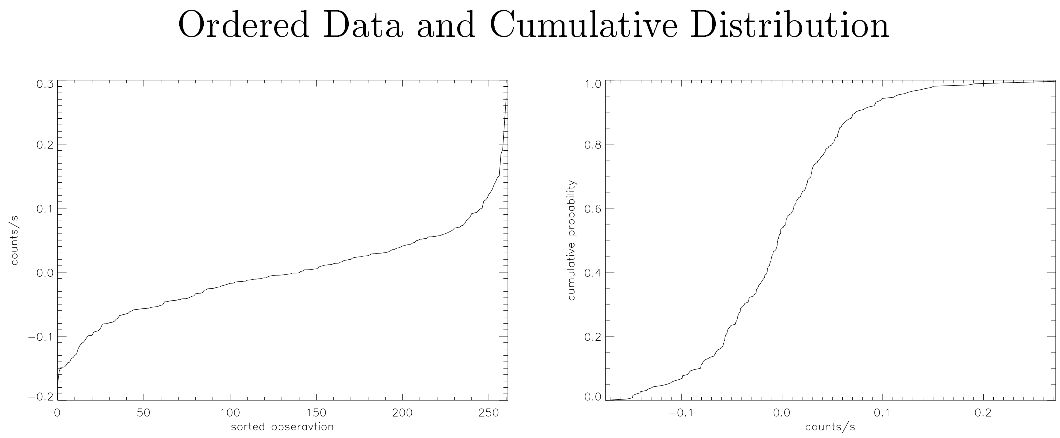

Figure 3.12: The figure on the left is the dataset sorted into ascending order. The figure on the right is the same data summed and normalized to estimate the CDF.

CDF from our model. The Figure 3.13 shows the data CDF and two model CDFs, one for counting statistics only and the other with an additional RMS sky flux of 0.04 counts per second. The data and models are for energy band 1 of the dataset. Figure 3.14 shows the absolute values of the differences between the CDFs in figure 3.13. The maximum value of the difference between two CDFs is the Kolmogorov Smirnov statistic D (shown in figure 3.14). The important property of the D statistic is that the probability that a certain D value for two CDFs drawn from the same dataset can be calculated [Press *et al.* 1988].

$$Probability(D > observed) = Q_{KS}\left(\sqrt{N}D\right)$$

Comparing CDFs

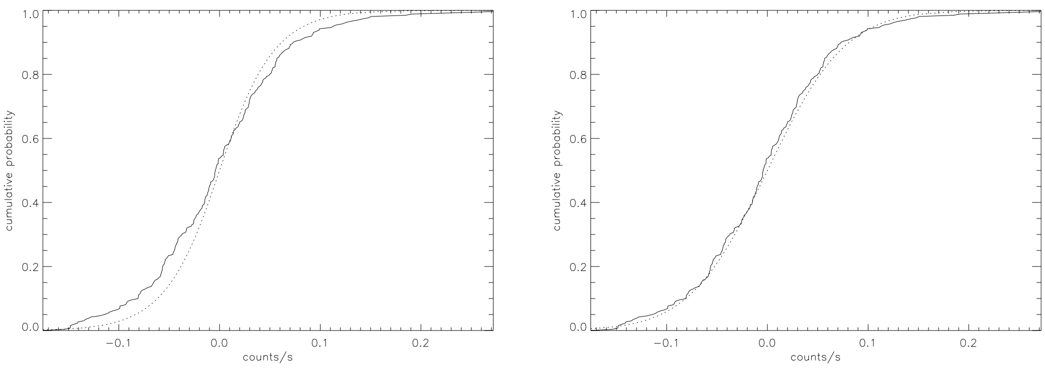

Figure 3.13: The CDF for the data is compared to two different model CDFs. The dotted line in the figure on the left is the CDF for a model with only counting statistics and the dotted line in the figure on the right is for an additional sky flux of 0.04 counts/s.

for two CDFs when one CDF is a continuous function and the other has N data points. Where :

$$Q_{KS}(\lambda) = 2\sum_{j=1}^{\infty}(-)^{j-1}e^{-2j^2\lambda^2}$$

So, for any D value a probability can be calculated.

For the D values from figure 3.14 of 0.1 and 0.043 the probabilities of the CDFs being drawn from the model distribution are 0.8% and 72%, respectively. To find the sky fluxes that give good fits to the dataset, different sky noise contributions were added to the counting statistics. The KS probabilities derived from these different tests are shown as a function of the added RMS sky flux in figure 3.15. Taking the region in flux, the x axis, where the probability is greater than 5% gives the 90% confidence region (see table 3.3). The KS test routines from [Press *et al.* 1988] are

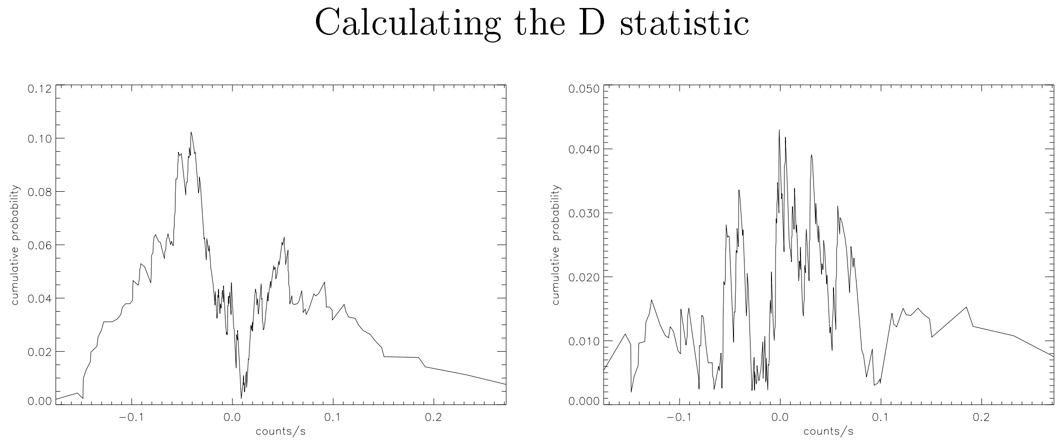

Figure 3.14: The figures are the differences between he CDFs shown in figure 3.13. The D value for the figures are 0.1 and 0.043 which correspond to probabilities of 0.8% and 72% likelihood of being drawn from the same distribution.

used throughout the analysis.

The KS test has no built in assumptions about the statistics governing the distributions that are being tested although our model does make such an assumption. This makes the KS test a general and conservative estimator. The fixing of the ends of the CDF makes the KS test less sensitive to the outliers in the distribution than the other test — the χ^2 test.

The χ^2 Test

For a set of N_i data points drawn from a distribution n_i, χ^2 is defined as :

$$\chi^2 = \sum_i \frac{(N_i - n_i)^2}{\sigma_{n_i}^2}$$

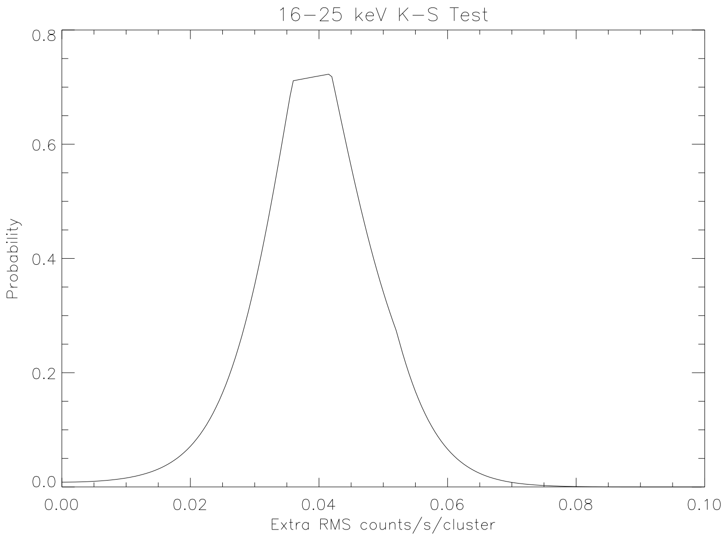

Figure 3.15: Kolmogorov-Smirnov test probability of fit of the data set to a model as a function of extra sky noise in energy band 1. The probability is sampled every 5x10^{-4} RMS counts/sec/cluster

and for Poisson statistics

$$\sigma_{n_i}^2 = N_i$$

The probability that a χ^2 measurement for data drawn from the model points n_i is greater than a particular χ^2 is :

$$P(\chi^2|\nu) = \frac{1}{\Gamma(\frac{\nu}{2})} \int_0^{\frac{\chi^2}{2}} e^{-t} t^{\frac{\nu}{2}} dt$$

Where the Γ function is defined as :

$$\Gamma(z) = \int_0^{\infty} t^{z-1} e^{-t} dt$$

And ν is the number of degrees of freedom to the model.

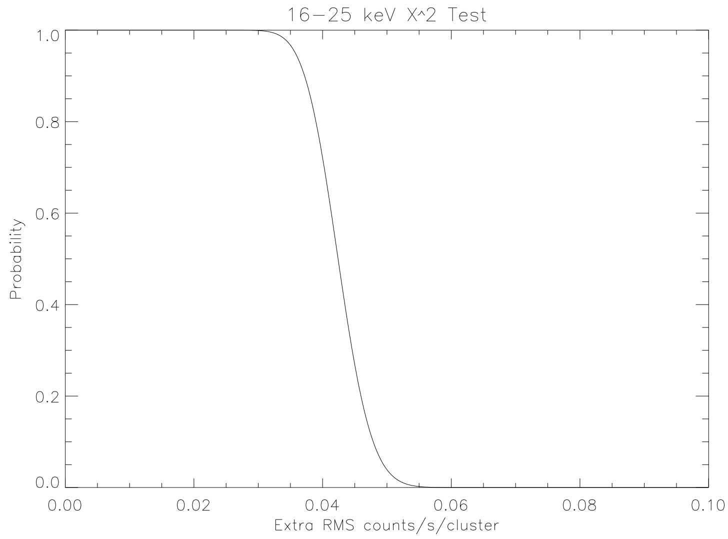

Figure 3.16: χ^2 test probability of fit of the data set to a model as a function of extra sky noise in energy band 1. The probability is sampled every 1x10^{-4} RMS counts/sec/cluster

In this case the number of degrees of freedom is equal to the number of data points. As with the KS test, the χ^2 value can be found for different values of RMS flux added in quadrature to the basic statistical model. Figure 3.16 shows the probability that a χ^2 value will be greater than the model value. The area on the left where the value is one is where the model does not have enough width to the distribution — the model, including the assumed fluctuations level, is smoother than the data. The area on the right is the area where the model has too much width. Taking the region in flux, the x axis, where the probability is between 5% and 95% gives the 90% confidence limits (see table 3.3).

The χ^2 test has a built in assumption that the errors are Gaussian. This assumption is not strictly true since the P(D) distribution has a high flux tail (figure 5.1) which is still present in the symmetrized form (figure 5.3). The agreement with the more general KS test results show that the effect is small (table 3.3).

Test Results

The test results for the KS and χ^2 tests are shown in figures 3.17 and 3.18, respectively. The fits of these test on the histogrammed dataset is shown in figure 3.19. The KS test results for the highest channel shows a low peak probability. This indicates that the data in those bands is not well fit by the model. Since the XRB flux in this bend is very low (see table 3.7), the extra noise in this band is entirely systematic and is not expected to fit the model. The KS results from this band is still used as a check on the χ^2 results. The use of the highest two energy bands as a measurement of the systematic errors is discussed in section 3.4.3.

Table 3.3 shows the extra RMS fluctuations for the two different test in the six different energy bands.

3.3.5 Cluster averages

The dataset is a combination of data from two different instruments — the two different clusters. Cluster 1 and cluster 2 have different detectors, electronics and data paths. These differences have led to two instruments with slightly different properties. So far, the two datasets have been combined without normalization,

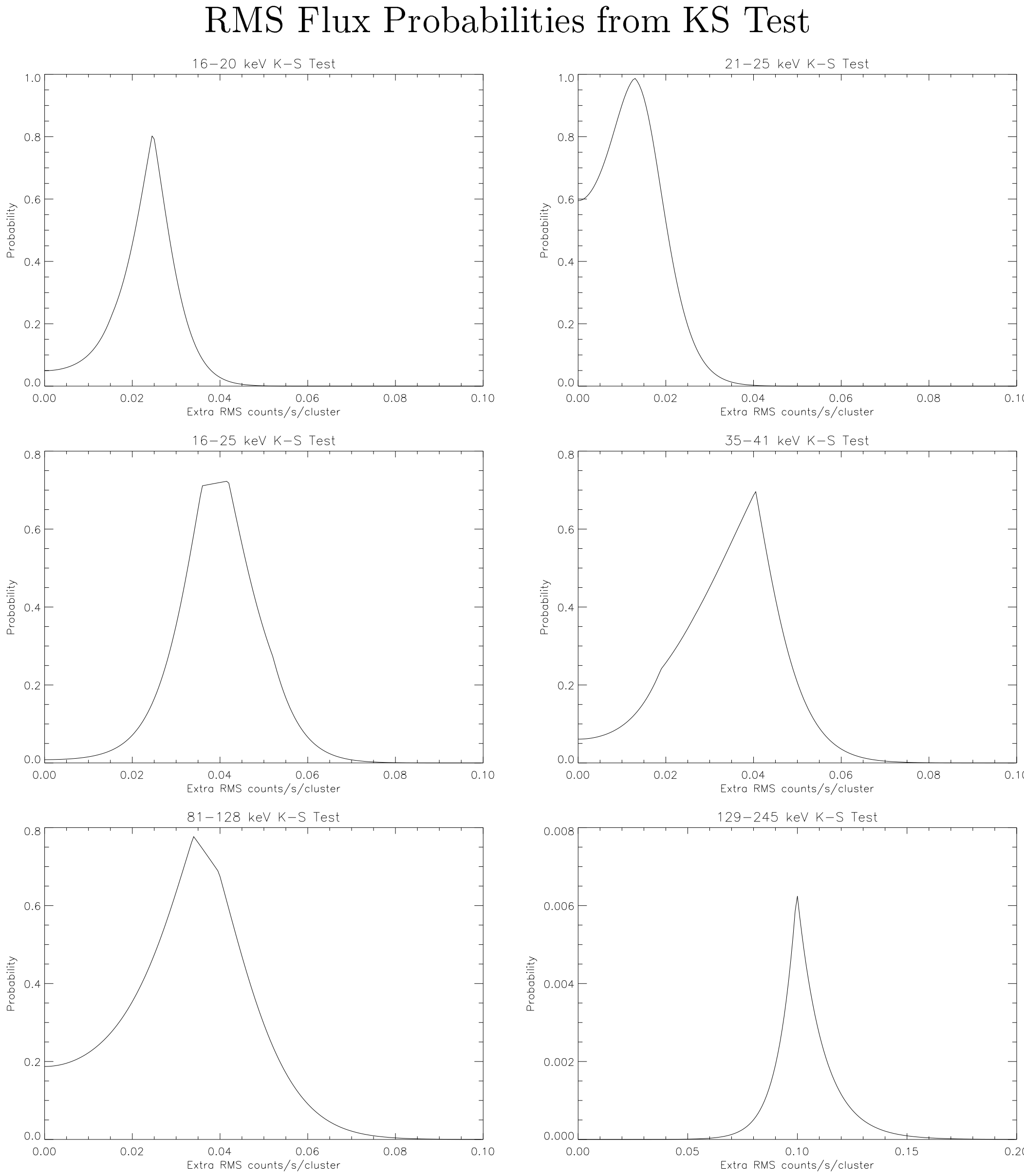

Figure 3.17: KS Test probabilities as a function of model RMS flux for the six energy bands.

RMS Flux Probabilities from χ^2 Test

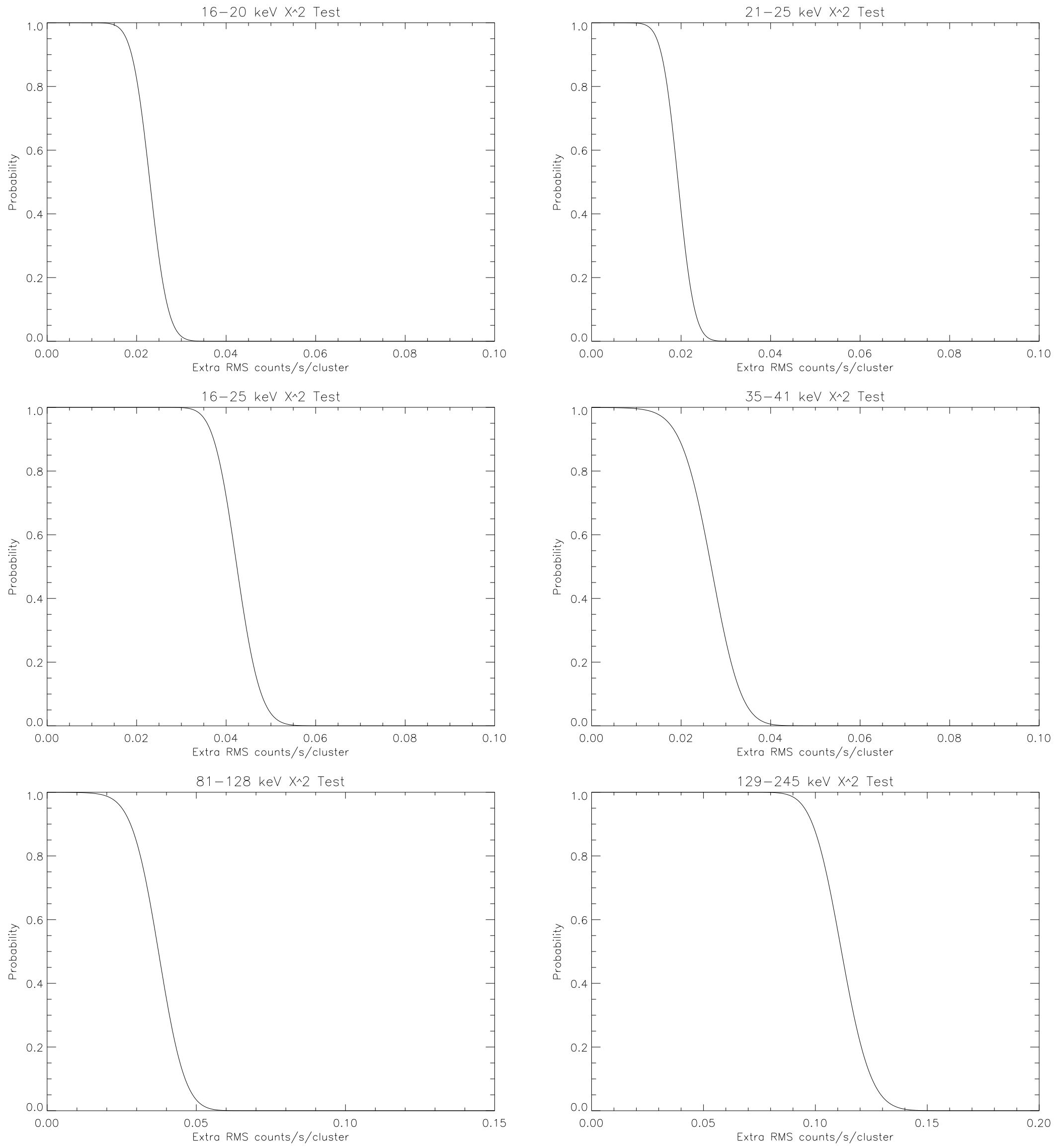

Figure 3.18: χ^2 Test probabilities as a function of model RMS flux for the six energy bands.

Model Fits to Histogrammed Difference Measurements

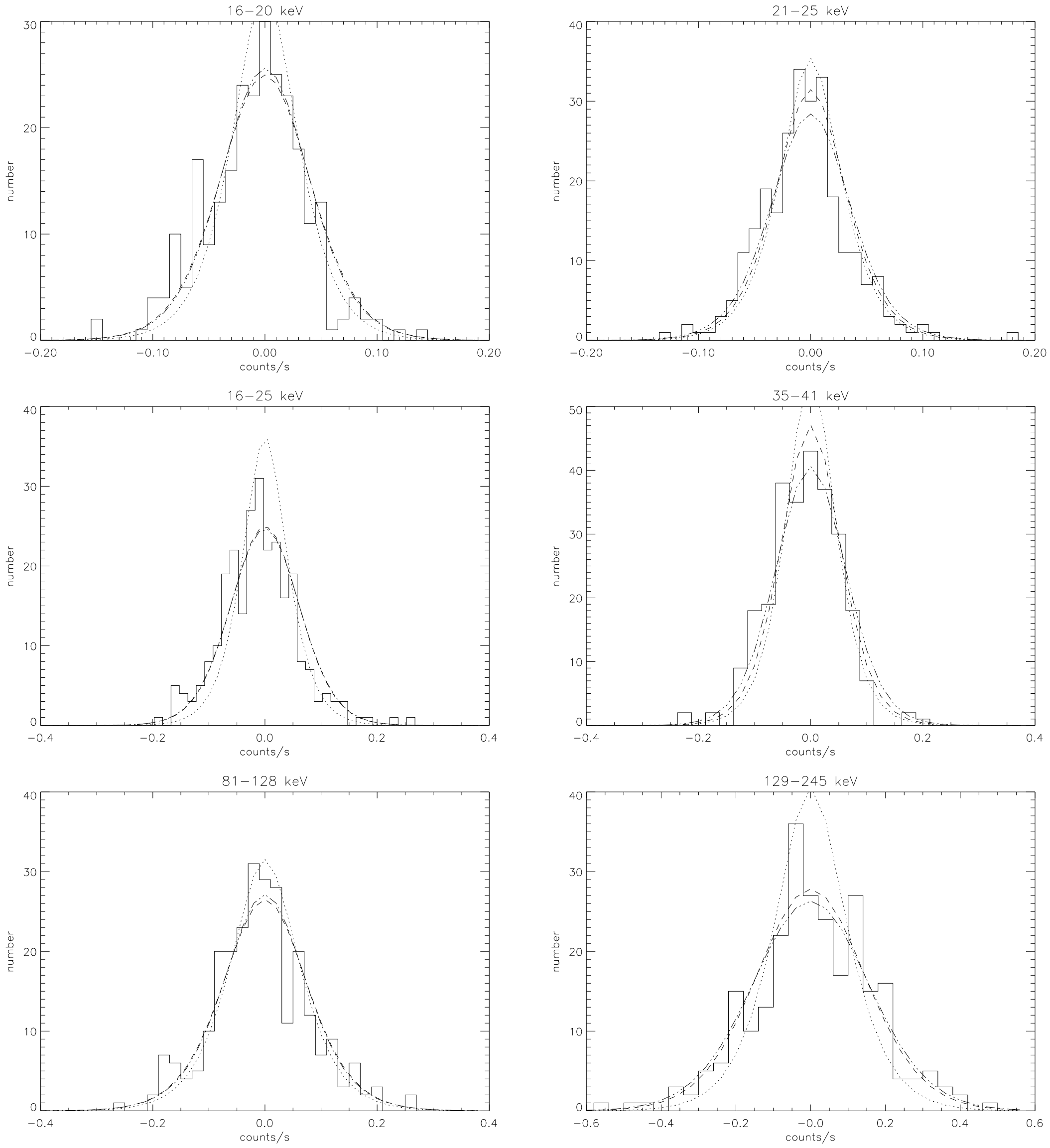

Figure 3.19: Histogram of difference for all observations in the final dataset in each of the six energy bands. There are three different fits shown. The dotted line is the fit is with counting statistics only. The dashed line is the fit from the KS test measurements and the dashed-dotted line is the fit from the χ^2 test measurements.

Table 3.3: Fluctuation Measurements from KS and χ^2 Tests

band	channel	KS test RMS counts/s	error	χ^2 test RMS counts/s	error
1a	16–20	0.025	0.007	0.023	0.003
1b	21–25	0.013	0.007	0.019	0.003
1	16–25	0.042	0.009	0.043	0.004
2	35–41	0.041	0.012	0.027	0.005
3	81-128	0.034	0.014	0.037	0.007
4	129-245	0.10	0.011	0.11	0.01

since that introduces another free parameter for each instrument. It is possible that the two halves of the dataset should be individually normalized before they are combined. This has the effect of adding two free parameters to the model — the averages of the two clusters individual fluxes. Figure 3.21 shows the averages for the different energy bands for the two clusters. The results for averaged and non-averaged data are shown in tables 3.4 and 3.5 The effect of the two constraints can be accounted for explicitly in the χ^2 test results but not in the KS test. Since the subtraction of the average does not significantly affect the results, the non-normalized results have been used for the rest of the analysis. Section 3.4.2 discusses the average offsets of the clusters and their effect on the systematic errors.

So far the RMS flux added to the counting statistics in the two tests has been referred to as extra or additional flux. This is because so far we have not separated the sky flux from the broadening of the distribution due to systematic effects in the instrument and observing method. Looking at table 3.3, there is a large extra noise

Table 3.4: KS Test Normalized vs Non-normalized results

band	channel	Non-Normalized	error	Normalized	error
1a	16–20	0.025	0.007	0.025	0.007
1b	21–25	0.013	0.007	0.014	0.008
1	16–25	0.042	0.009	0.037	0.009
2	35–41	0.041	0.012	0.036	0.017
3	81-128	0.034	0.014	0.033	0.021
4	129-245	0.10	0.011	0.10	0.018

Table 3.5: χ^2 Test Normalized vs Non-normalized results

band	channel	Non-Normalized	error	Normalized	error
1a	16–20	0.023	0.003	0.023	0.003
1b	21–25	0.019	0.003	0.019	0.003
1	16–25	0.043	0.004	0.042	0.004
2	35–41	0.027	0.005	0.026	0.005
3	81-128	0.037	0.007	0.036	0.007
4	129-245	0.11	0.01	0.11	0.01

in the highest two energy bands where the flux from the XRB is small (see section 5.3). This is an indication that there are significant systematic effects convolved with the the sky signal. The next step in the analysis is to separate the sky signal from the systematic effects.

3.4 Systematics

The fundamental source of uncertainty in the data is in the counting statistics of the photons in the various different observations. This has been accounted for explicitly in the model, so the flux we measure is in addition to the counting statistics. The model, however does not take systematic effects into account. The extra flux measured in the model is the convolution of the sky flux with the systematic effects. Here we use three different methods to limit and measure these systematics: predictions, tests and direct measurement. From these measurements we find that, the two major sources of systematic error are livetime correction errors and errors introduced by the chopping of the signal by the aperture modulator. Both result in noise which has the spectrum of the detector internal background.

3.4.1 Predictions of Systematics

[Gruber *et al.* 1996] calculated the residual errors from the rocking in the HEXTE instrument. The calculations were made for a smaller pre-flight predicted instrument noise, but are here adjusted for the instrument noise level measured in the dataset. These calculations were designed to be conservative upper limits and so are designed to overestimate the statistical errors.

Rocking the instrument off source to create background fields creates a pattern of alternating on-source and off-source measurements (section 2.1.3). The background measurement for an on-source position can be looked at as the average of the two surrounding background measurements. If the background is changing, for example as an exponential decay as it is during recovery from SAA events, there is a residual second order term to the change in the background and the method of averaging the two background fields leaves an error. [Gruber *et al.* 1996] estimate a limit of 0.3% of the internal instrument noise as the limit to the systematic error. For our energy bins this would give the fluxes shown in table 3.6. These values are larger than the

Table 3.6: Predicted Limits to Systematics

band	channel	Limit (counts/s)	χ^2 data (counts/s)
1a	16–20	0.011	0.023
1b	21–25	0.010	0.019
1	16–25	0.023	0.043
2	35–41	0.026	0.027
3	81-128	0.053	0.037
4	129-245	0.13	0.11

signal in all but the lowest channels where the signal dominates the systematics. This shows that the predictions are of the same order as the systematics since they overpredict the flux in the two highest channels, which are dominated by systematics effects, by 30%.

3.4.2 Tests for Systematics

A number of different tests for systematic effects have been performed to limit effects on the analysis. Since the dataset contains *all* the uncontaminated long HEXTE observations, there is no independent measurements precise enough to constrain the systematics to a meaningful level. These tests mostly identify effects which would overwhelm the fluctuation signal. The only way to truly eliminate the systematic effects at the level of the fluctuation measurement is to measure them in the fluctuation data set using auxiliary data and tricks of analysis (see section 3.4.3). Such tests have been invented and used along the way in the analysis to find and remove systematic effects and have led to the data selection criteria in sections 2.2, 2.3 and 3.1.3.

Averages

The averaging of all data is the simplest test which identifies the more blatant systematic effects. Most of the possible effects from orbital and spacecraft orientation will be averaged out, while zeroth order and spacecraft-centric effects will remain. The average differences are shown in figures 3.20 and 3.21. The averages are $2.7 \times 10^{-5} \pm 1.8 \times 10^{-5}$ counts per second for cluster 1 and $1.1 \times 10^{-4} \pm 2.1 \times 10^{-5}$ counts per second for cluster 2.

The clusters are positioned so that cluster 1 rocks in an axis parallel to cluster 2 and cluster 2 rocks towards and away from cluster 1 (see figure 2.8). The rocking in cluster 2 brings it closer and farther away from the mass of cluster 1. This increases the background in cluster 2 when it is the the off-source-plus position, which is the position closer to cluster 1. [Gruber *et al.* 1996] estimate an increase of 0.01% of the background in this position. This would translate into a positive offset in the difference measurement. The positive offset in cluster 2 translates into a 0.016 ± 0.004 % increase in the background rate, which agrees roughly with the Gruber calculation. Since this is a first order effect, and the the measurements of

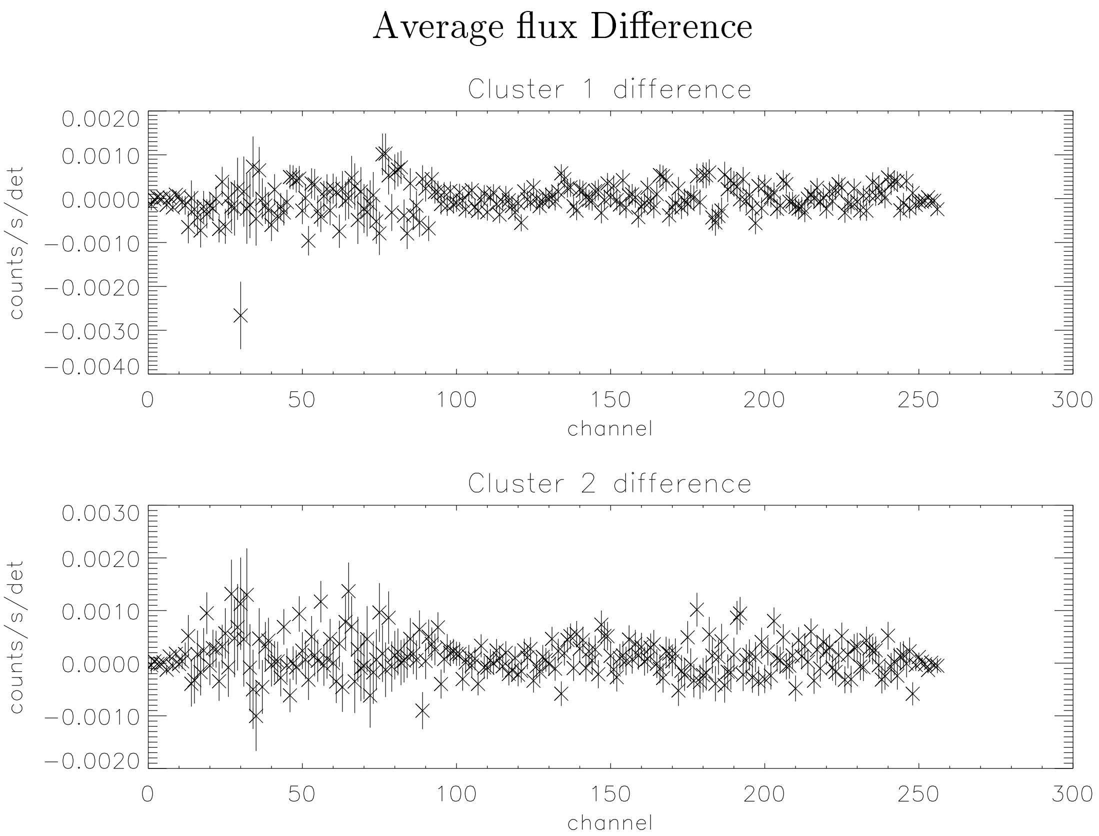

Figure 3.20: Average flux difference for the entire dataset taken as a whole using the full HEXTE energy resolution.

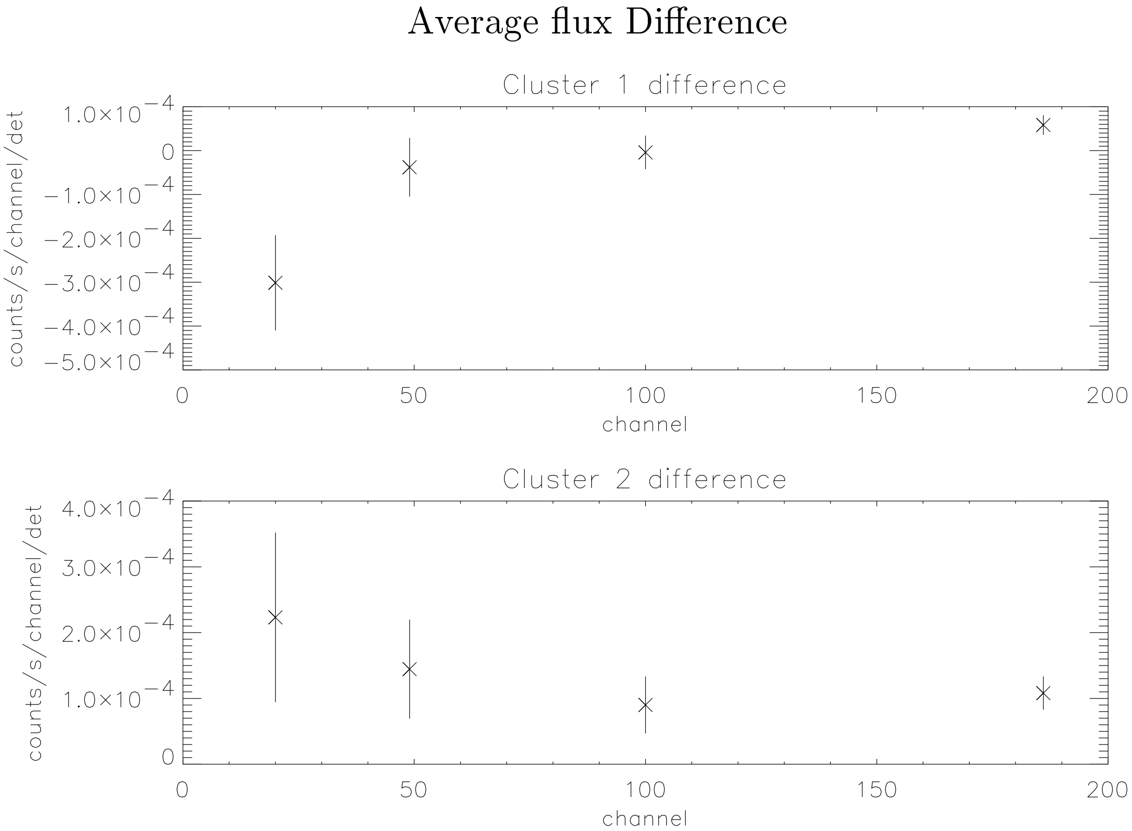

Figure 3.21: Average flux difference for the entire dataset taken as a whole using the standard 4 energy bins. Cluster 2 can be seen to have a net positive offset of $1.1\text{x}10^{-4} \pm 2.1\text{x}10^{-5}$ counts per second.

the fluctuations amounts to a study of the second moment of the sky fluxes, this offset should not affect the analysis. In section 3.3.5 the effect of the removal of the cluster averages did indeed leave the results unchanged.

Consistency

Another general test is performed to evaluate the consistency of the signal within a single observation. The longest single observation of an object, NGC 7469, $\sim$800 ksec has been divided into 8 sub-observations of $\sim$100 ks each. These sub-observations, being of the same field, should produce a consistent measurement. These observations taken over several months, with one sub-observation separated by 3 months, included a wide range of spacecraft and observational conditions and therefore should display any long term systematic variations. The observations in the 4 broad energy bands, shown in figure 3.22, are consistent with their average.

Modeling

One indication of the level of systematic effects is found by comparing the model's sensitivity to fluctuations to the sensitivity found in the dataset. A simulated data set was made of differing numbers of observations at different points in the analysis. The simulation assumes the same counting statistics as the observations and broadening for an assumed RMS sky fluctuation, but does not include any broadening from systematics. The fluctuation levels used in the model are those from section

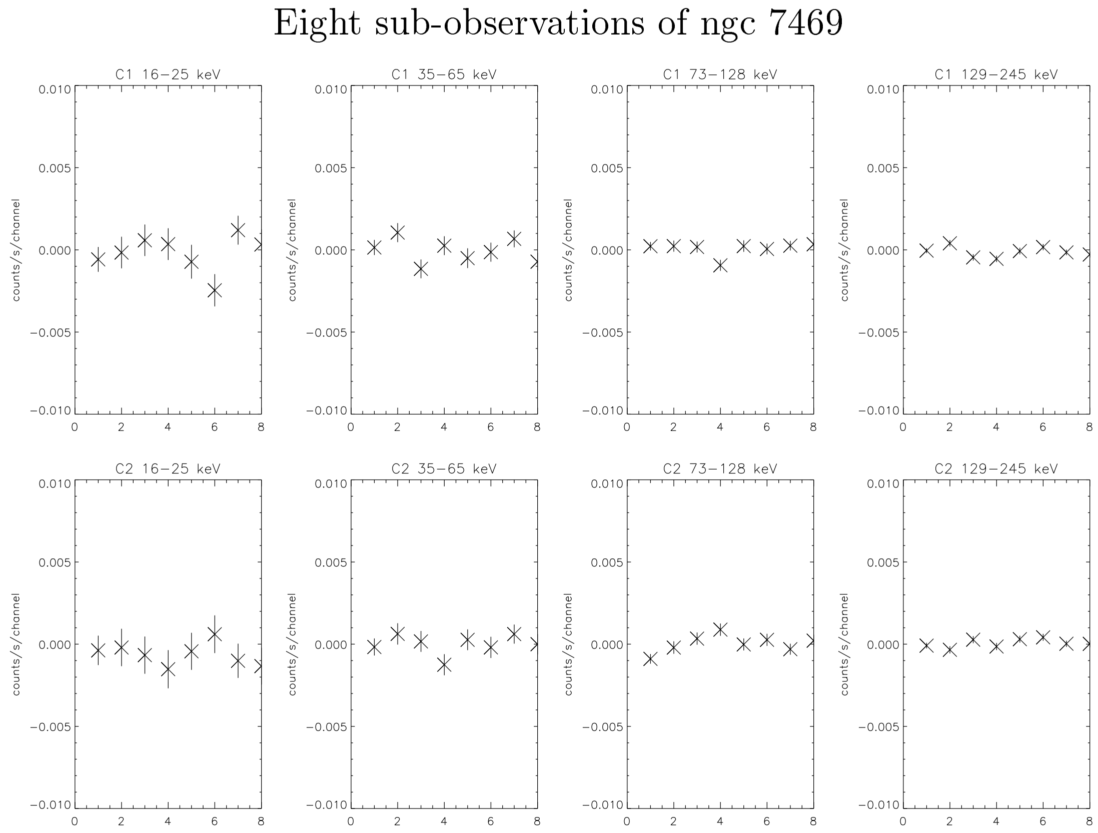

Figure 3.22: The observation of ngc 7469, the longest in the data set is divided into eight parts to check for consistency in observing a single field of view on the sky. The upper row is from cluster 1 and the lower row is from cluster 2. The data is binned in 4 energy bands which differ in the middle two from the standard energy bands.

5.3 and are shown in table 3.7.

For the smaller amounts of data from the first year of the mission, shown in figure 3.23, the simulation agrees well with the measurements in the two lower energy bins. This indicates that at this level the systematic factors have not become significant. For the entire dataset, shown in figure 3.24, the simulated data has a narrower range of acceptable probabilities and the peak in the distribution is slightly shifted by the

Simulated vs. Measured Data from A01

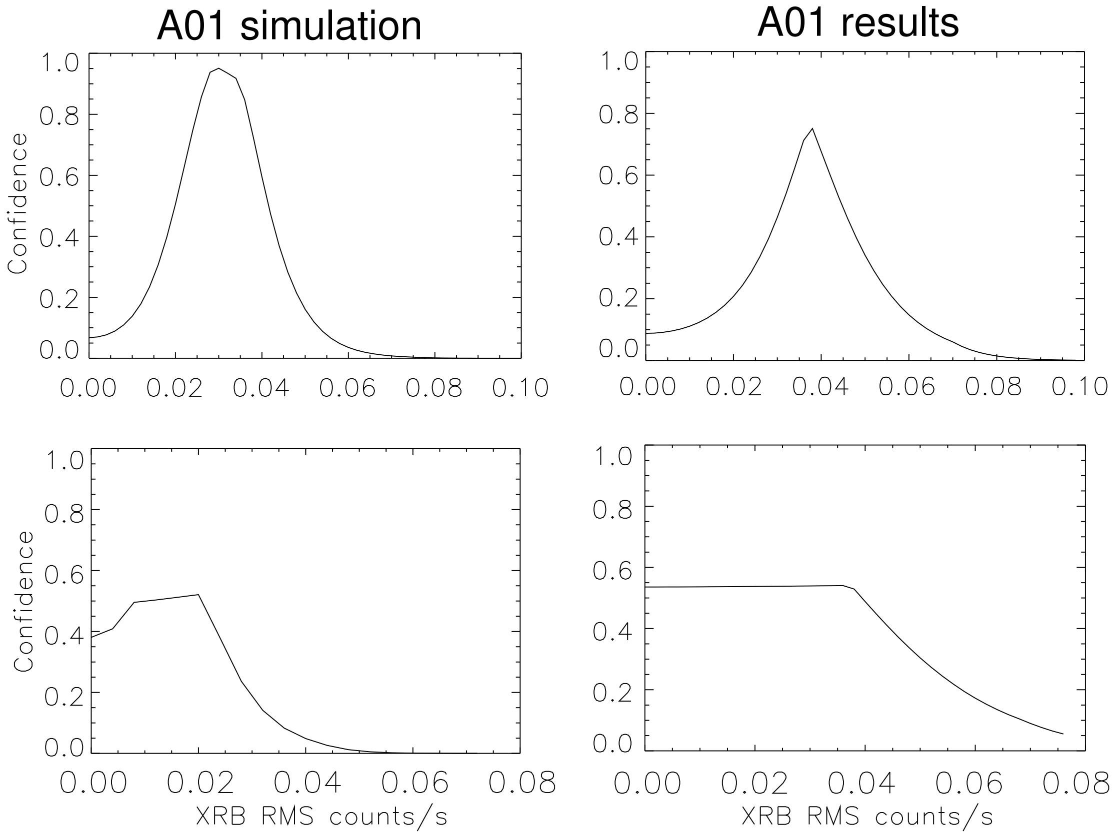

Figure 3.23: KS test confidence of the simulated data (left panels) vs the measurements (right panels) for the first years data versus the assumed fluctuation level in detector counts. The top row is for the 15.5–24.9 keV and the bottom row is for 43–64 keV.

these systematics.

3.4.3 Direct Measurement of the Systematics

The higher energy bands in the HEXTE instrument provide a means of measuring the effects of the systematics. Table 3.7 shows the predicted fluctuation levels in detector counts per second for the different energy bands. The sky fluctuation level

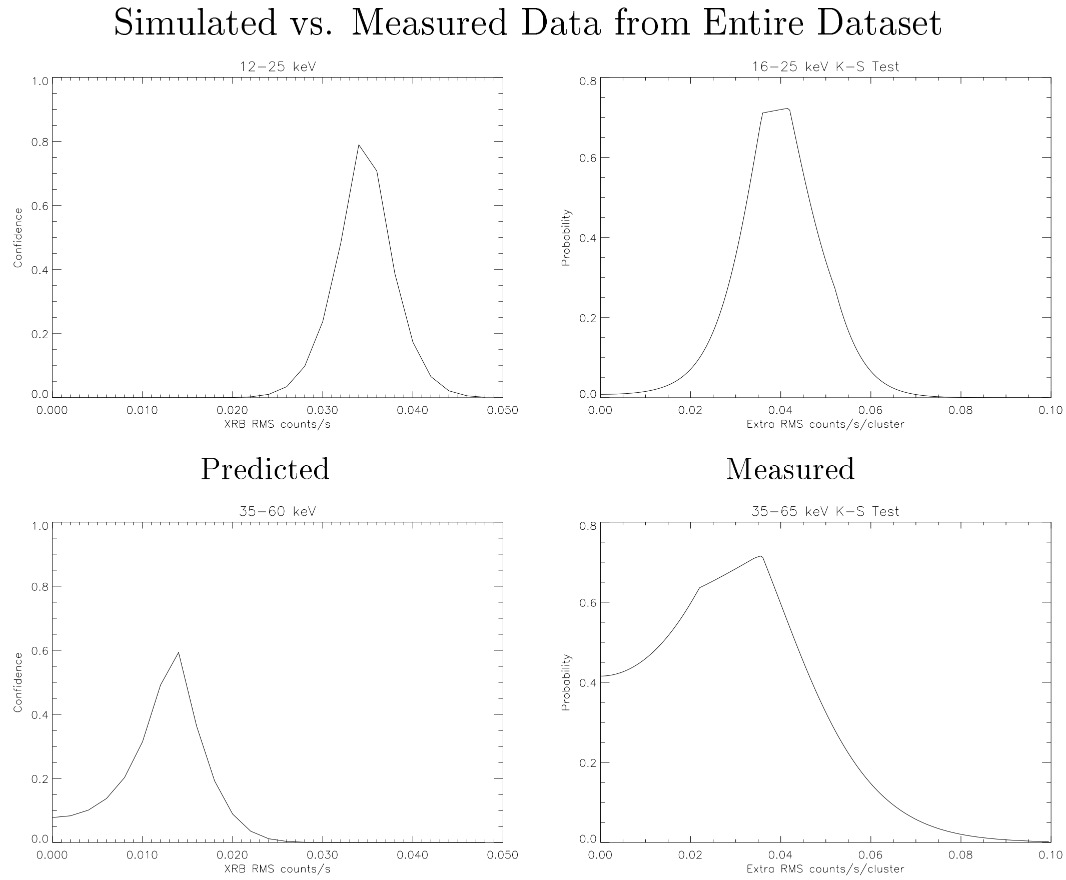

Figure 3.24: KS test confidence of the simulated data (left panels) vs the measurements (right panels) for the entire data set versus the assumed fluctuation level in detector counts. The top row is for the 15.5–24.9 keV and the bottom row is for 34–64 keV.

predicted in the highest two bands is more than an order of magnitude less than the additional RMS fluctuation measured by the two tests (table 3.3). The signal in these energy bands is then a direct measurement of the level of the systematics in the instrument.

Having two energy bands, 3 and 4, which are comprised wholly of a systematic signal, this information can be used to estimate the systematic noise levels in the

Table 3.7: Predicted Fluctuations

Band	Energy (keV)	XRB Model count rate (c/s)	Anticipated Fluctuation (c/s)	HEXTE Detector Background (c/s)
1a	15.5–20.2	0.158	0.013	4.06
1b	20.2–24.9	0.109	0.009	3.54
1	15.5–24.9	0.267	0.021	7.60
2	34–41	0.048	0.004	8.71
3	80–132	0.023	0.002	17.7
4	132–261	0.0054	0.0004	42.8

other energy bands if the dependence of the noise on energy is understood. The first step is to calculate the systematic noise as a function of energy in these two bands. This is done by dividing the signal by the instrument background count rate of the bands (table 3.8). The final line in the table is the weighted average of the two measurements.

Using this average as a measurement of the systematic noise, makes an assumption about the energy dependence of the processes creating the systematic noise, since it is an average over different energy bands. At first glance, the agreement of the two measurements of the systematics in each test appear to indicate that the systematics are a constant function of the instrument background over the upper $\frac{3}{4}$ of the instruments energy band. This is equivalent to assuming that the systematics are due to errors in the livetime, since errors in the livetime produce incomplete subtraction of the instrument background. Section 3.4.4 will demonstrate that the major systematic error components are indeed livetime corrections.

The χ^2 test is more sensitive to outliers in the distribution than the KS test which by definition has the two end points fixed. Since the two tests are sensitive to different parts of the flux distributions, they are not necessarily sensitive to the same part of the systematic noise distribution and are therefore treated separately. Table 3.8 shows the weighted average of the systematic effects for the two tests.

Table 3.8: Systematic errors in counts per second per count of internal background

band	energy keV	KS test counts/s/ibkg	error	χ^2 test counts/s/ibkg	error
3	80–132	0.008	0.003	0.0084	0.0016
4	132–261	0.009	0.001	0.0105	0.0010
	Average	0.009	0.001	0.0099	0.0008

Considering the systematics to scale with the internal background, the systematic errors derived for the lower energy bands are shown in table 3.9. Subtracting this

Table 3.9: Systematic noise predicted from bands 3 and 4

band	energy keV	RMS noise counts/s	error
1a	15.5–20.2	0.0100	0.0008
1b	20.2–24.9	0.0088	0.0007
1	15.5–24.9	0.0188	0.0016
2	34–41	0.0216	0.0018

systematic noise in quadrature from the RMS fluctuations in the lower bands gives a slight correction to the fluctuation measurements (table 3.10), which gives the RMS sky flux measurement for the XRB fluctuations. The sky fluctuations are shown with the original fluxes and the systematic corrections in figure 3.25.

Table 3.10: RMS Sky Fluctuations corrected for systematics

band	energy keV	KS test counts/s	error	χ^2 test counts/s	error
1a	15.5–20.2	0.023	0.007	0.021	0.003
1b	20.2–24.9	0.010	0.007	0.017	0.003
1	15.5–24.9	0.037	0.009	0.038	0.004
2	34–41	0.035	0.012	0.016	0.006

3.4.4 Components of the Systematics

In this section, the empirical systematic corrections used in the final results above are shown to be quantitatively consistent with known sources of systematics in the HEXTE detectors.

To understand the cause of the systematic effects, the components of different known systematic effects have been measured. As each significant component of the total is identified it will be removed so that only the unidentified portion of the systematic noise will remain. We have identified three components to the systematic noise : the results of the drift in gain of the detectors, the correction of the livetime errors and the chopping pattern of the aperture modulator. The effect of the gain variations is found to be insignificant, but the other two factors make up the majority of the measured systematic noise.

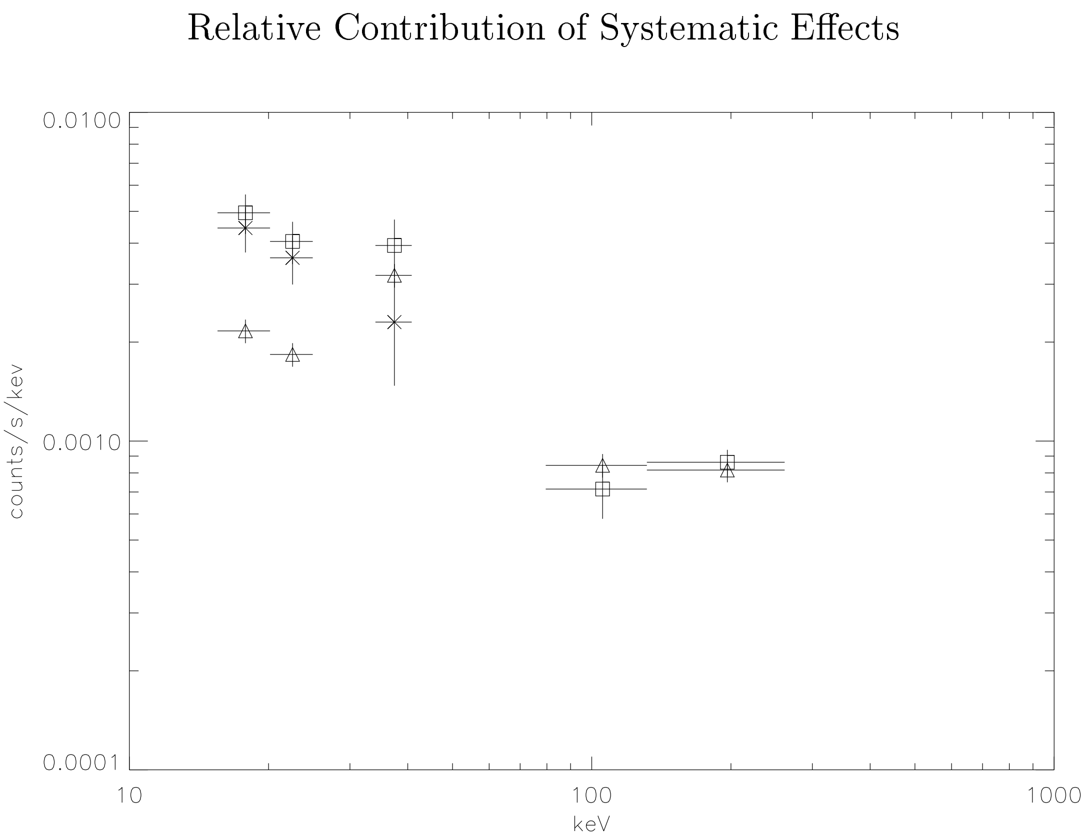

Figure 3.25: The change in the fluctuation measurements with the subtraction, in quadrature, of the systematic noise is shown as a function of energy. The raw fluctuation measurements from the χ^2 test (table 3.3) are the square points. The systematic noise calculations (table 3.9) are the triangles and the sky fluctuations (table 3.10) are the crosses.

Gain Jitter

The HEXTE instrument has automatic gain control circuitry which keeps the gain stable to $\sim$ 0.3% RMS gain variation ([Rothschild *et al.* 1998] and section 2.1.1). This small change in gain moves the edges of the channels in energy space and will change the count rate in the data energy bands. The amount of the change in the counting rate depends on the derivative of the energy spectrum of the background (figure 3.7). Using the average background rates, the channel boundaries were shifted in energy space by 0.3% and the resulting changes in the counting rate are shown in table 3.11 in comparison to the total systematic rate. The effects are

Table 3.11: Systematic effect from Gain Jitter

band	energy keV	systematic noise counts/s	jitter contribution counts/s
1a	15.5–20.2	0.010	0.0002
1b	20.2–24.9	0.009	0.001
1	15.5–24.9	0.019	0.001
2	34–41	0.022	0.002
3	80–132	0.043	0.0002
4	132–261	0.106	0.00002

essentially zero except where the band edges are near the shoulders of peaks in the background distribution where small changes in the energy can cause a large change in counting rate. Even in the worst band near 30 keV, the noise from the jitter is insignificant when added in quadrature to the other systematic effects.

Livetime Correction

The "Biff" correction to the livetime was discussed in section 2.3.3. It is a known source of systematic noise. It introduces counting statistics from the rates that are used in its calculation, moreover it introduces errors from its imperfect correction of the livetime. Livetime errors by their very nature affect all the rates equally and so are energy independent. The effects of this correction have been measured for one source, the Crab. While observing the Crab nebula, which is known to be a constant x-ray source, Biff Heindl measured the increase in the systematics created by this correction on 50 ks of data [Heindl 1999]. The effect was measured to be an increase of 12% over the counting statistics. Since there was only one measurement of this effect made, there is no measure of the error in this measurement except by comparison of the two clusters. I crudely estimate the error by assuming that the measurements from the two different clusters are 1σ apart. This assumption is not a strong statement about the errors and the effect of varying this error is considered in the next section. This effect produces an additional 0.0024 ± 0.0006 counts per second per count of internal background. Table 3.12 shows this effect applied to the different energy bins.

Table 3.12: Systematic results of the Biff correction

band	energy keV	flux counts/s	error
1a	15.5–20.2	0.0025	0.0007
1b	20.2–24.9	0.0021	0.0006
1	15.5–24.9	0.0046	0.0012
2	34–41	0.0053	0.0014

When effects of the Biff correction are removed from the total systematic errors, the remaining unclassified noise is 0.0096 ± 0.0010 counts per second per count of instrument background. The remaining noise per energy band shown in table 3.13.

Table 3.13: Unresolved Systematics after removal of the Biff correction

band	energy keV	RMS noise counts/s	error
1a	15.5–20.2	0.010	0.001
1b	20.2–24.9	0.009	0.001
1	15.5–24.9	0.018	0.002
2	34–41	0.021	0.002

Aperture Modulator

The rocking provides background estimates that are automatically correct to first order in time, so the dominant residual must then vary with the square of the rocking period. The systematic effects of the rocking can therefore be measured as the fraction of the systematic noise which varies with the rocking period.

Most of the observations in the dataset were taken with a 16 second rocking period (see section 2.1.3). A small fraction of the data, 1652 ks, was taken with 32 second rocking. Dividing the data into two separate subsets allows us to directly measure the effect of changes in the rocking period on the systematics. Unfortunately, the 32 second dataset is small and still contains $\sim$ 200 ks or 14% "contamination" from the 16 second rocking period. This results in large error bars on the measurements.

The same analysis used on the complete dataset is used again on the two subsets. Since we are interested only in the systematic effects from these runs, only the upper two bands are considered. The results of the χ^2 test of the two runs are shown in table 3.14.

Table 3.14: 16 and 32 second rocking

band	channel	16 second rocking counts/s	error	32 second rocking counts/s	error
3	81-128	0.033	0.009	0.055	0.017
4	129-245	0.099	0.011	0.171	0.028

Table 3.15: 16 second vs 32 second in counts per second per keV

band	energy keV	16 second rocking counts/s/ibkg	error	32 second rocking counts/s/ibkg	error
3	80–132	0.0075	0.0018	0.012	0.004
4	132–261	0.0093	0.0011	0.016	0.003
	Average	0.0088	0.0009	0.015	0.002

The systematics from the 32 second rocking run can be seen to be larger. The rates are converted into counts per second per keV and the Biff correction noise is removed. The 32 second rocking measurement is corrected for the small amount of contamination from the 16 second rocking, a 10% effect. The results can be seen in table 3.16. Since the effect of doubling the rocking time should quadruple the

Table 3.16: systematic effect of Rocking Period

channel	16 second rocking counts/s/ibkg	error	32 second rocking counts/s/ibkg	error
Average	0.0085	0.0011	0.017	0.003

systematic effect, it is obvious that the rocking period is not the only systematic left. The fractional change from doubling the rocking period is 2.01 $\pm$ 0.20. From this the fraction of the signal that varies by a factor of 4 can be calculated. If a systematic error σ_{rock} is multiplied by a factor of 4, added to another error and the total, σ_{tot}, changes by x, the fraction of the error due to the rocking is:

$$\frac{\sigma_{rock}}{\sigma_{tot}} = \sqrt{\left(\frac{x^2 - 1}{15}\right)}$$

Here x is the fractional change in the systematic error from changing the rocking period. This gives a systematic contribution of 0.0043 $\pm$ 0.0005 due to the rocking period. When this is subtracted in quadrature from the unidentified systematics, the remaining unresolved systematic noise is 0.0086 $\pm$ 0.0022 counts/s/ibkg. The results are summarized in table 3.17.

Table 3.17: Summary of Systematic Components

Component	flux counts/s/ibkg	error
Biff Correction	0.0024	0.0006
Rocking Correction	0.0043	0.0005
Unknown	0.0086	0.0022
Total	0.0099	0.0008

If the errors in the Biff correction were doubled (assuming that the cluster 1 and cluster 2 measurements were $\frac{1}{2}\sigma$ apart). The Biff correction would change to 0.0024 $\pm$ 0.0013, the fractional change for the rocking period would become 1.89 $\pm$ 0.33

and the remainder would become 0.0086 $\pm$ 0.0034 counts/s/ibkg (table 3.18).

Table 3.18: Summary of Systematic Components with larger Biff errors

Component	flux counts/s/ibkg	error
Biff Correction	0.0024	0.0013
Rocking Correction	0.0043	0.0007
Unknown	0.0086	0.0034
Total	0.0099	0.0008

Chapter 4

Results

4.1 Fluctuations

The fluctuations in the XRB have been measured in two broad bands 15.5–24.9 keV and 34–41 keV. The lower band can be divided into two smaller bands 15.5–20.2 keV and 20.2–24.9 keV and still have significant results although the standard errors are increased somewhat.

The fluctuations measurements from the two tests from chapter 3 are summarized in table 4.1. Since the χ^2 test produces more significant results, those will be used throughout the rest of the results chapter.

Since the HEXTE results measure the XRB fluctuations only, to find the fractional fluctuations, the average count in the XRB must be calculated. The XRB model from [Gruber *et al.* 1999] is used. This model is discussed in section 5.2 and

Table 4.1: RMS Sky Flux Measurements corrected for systematics

band	energy keV	KS test counts/s	error	χ^2 test counts/s	error
1a	15.5–20.2	0.023	0.007	0.021	0.003
1b	20.2–24.9	0.010	0.007	0.017	0.003
1	15.5–24.9	0.037	0.009	0.038	0.004
2	34–41	0.035	0.012	0.016	0.006

has also been used in the predictions of the fluctuations in section 5.3. Table 4.2 shows the XRB model flux for the HEXTE field of view for the different energy bands. Using this XRB flux and the fluctuation measurements in table 4.1, the

Table 4.2: XRB Model Flux

band	energy keV	XRB flux counts/s
1a	15.5–20.2	0.158
1b	20.2–24.9	0.109
1	15.5–24.9	0.267
2	34–41	0.048

fractional fluctuations can now be calculated. The results are shown in table 4.3 and figure 4.1. The best fit energy power law index to the spectrum of the fluctuations has the value 1.17 ± 0.54. This fit is not very constraining, since there is only one degree of freedom in the system.

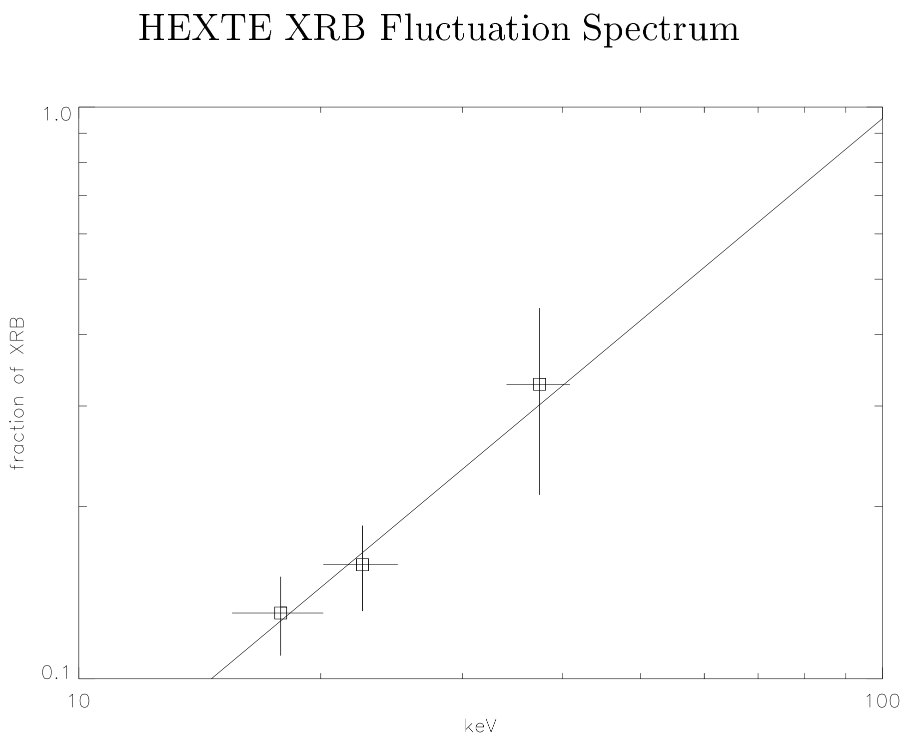

Figure 4.1: The fluctuations in the XRB from HEXTE are shown as a fraction of the model XRB flux. The line is the best fit power law with index 1.17

Table 4.3: Fractional XRB Fluctuation Measurements

band	energy keV	fraction of XRB	error
1a	15.5–20.2	0.130	0.021
1b	20.2–24.9	0.158	0.027
1	15.5–24.9	0.143	0.016
2	34–41	0.33	0.12

4.1.1 Comparing Fluctuations to Previous Results

To compare the fluctuation results to the other measurements in the same general energy bands: OSO-3 [Schwartz and Peterson 1974], HEAO-1 [Shafer 1983] and [Gruber 1992] and Ginga [Butcher *et al.* 1997]; the flux measurements need to be converted to a common field of view, because the fields of view of the instruments vary from 1 square degree to 49 square degrees. To do this, all the fluctuation measurements are converted to a fraction of the XRB flux for a hypothetical telescope of 1 steradian FWHM field of view.

The fields of view of the two HEXTE clusters, from section 2.1.2, are 1.11 and 1.08 square degrees. Since the fluctuations are proportional to $FOV^{\frac{1}{2}}$, the fractional fluctuations are multiplied by the square root of the number of FOVs per steradian to convert to a hypothetical 1 sr FOV instrument. This produces the results in table 4.4 and the HEXTE data points shown in figure 4.2.

The results which most overlap the energy range of the HEXTE measurements are those from the HEAO A-4 experiment [Gruber 1992]. The results of Gruber's

Table 4.4: XRB Fluctuation as Fraction of XRB Flux

band	energy keV	fraction of XRB (counts/s/sr)	error
1a	15.5–20.2	0.0024	0.0004
1b	20.2–24.9	0.0029	0.0005
1	15.5–24.9	0.0026	0.0003
2	34–41	0.0060	0.0021

fluctuation measurements are shown in table 4.5.

Table 4.5: XRB Fluctuation from [Gruber 1992]

band	energy keV	fraction of XRB (counts/s/sr)	error
1	15–25	0.0029	0.0005
2	25–40	0.0034	0.0004
3	40–80	0.0039	0.0002

The results from the 15.5–24.9 keV HEXTE band agree with Gruber's results in his lowest energy band and have almost twice the significance. Figure 4.2 shows the combined results of the divided HEXTE bands and the HEAO A-4 data. The combined results are well fit with a energy power law spectrum of index 0.33 ± 0.09.

An early measurement of the XRB fluctuations (table 4.6) performed with OSO-3 is reported in [Schwartz 1969] and updated in [Schwartz and Peterson 1974]. These authors feel their measurements are significantly contaminated with systematic errors, so they provide only upper limits to the fluctuations.

The results from the HEAO A-2 fluctuation measurements taken at 2–10 keV are

HEXTE and HEAO-1 A4 XRB Fluctuation Spectrum

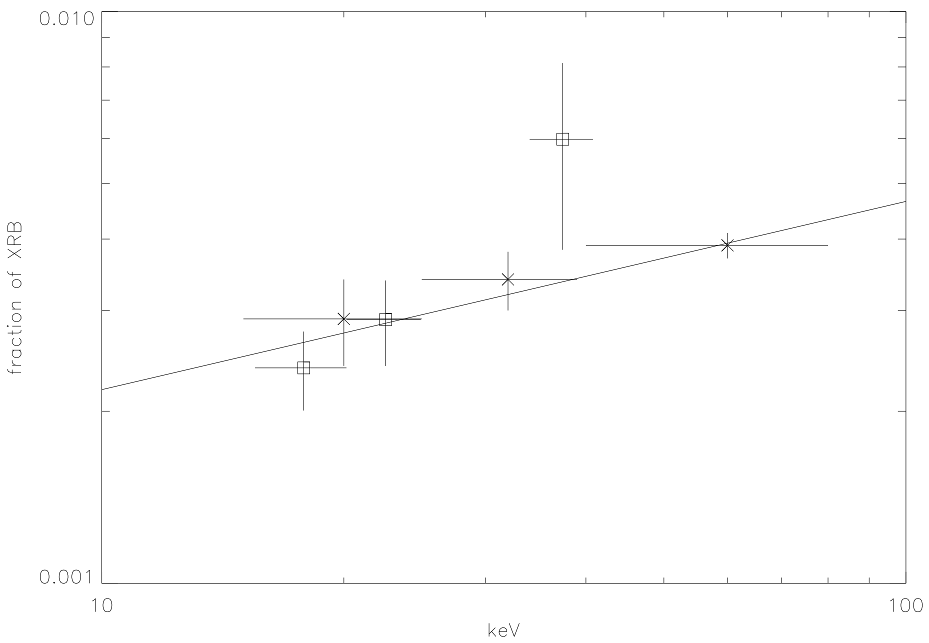

Figure 4.2: The fluctuations in the XRB from HEXTE and HEAO-1 A4 are shown as a fraction of the XRB flux for a hypothetical 1 steradian FWHM instrument. The HEXTE data points are squares and the HEAO points are crosses. The line is the best fit power law to the combined data set, which has a power law index of 0.33 ± 0.09.

Table 4.6: Upper Limits to XRB Fluctuation from [Schwartz and Peterson 1974]

band	energy keV	fraction of XRB (counts/s/sr)
2	7.7–12.5	0.015
3	12.5–22	0.015
4	22–38	0.19
5	38–65	0.04
6	65–113	0.05

reported by [Shafer 1983]. Shafer reports fractional fluctuations of 0.012 ± 0.004, which are converted to the 1 steradian FOV in table 4.7. Shafer's results are in nearly the same energy band as the more recent Ginga measurement. The Ginga measurement [Butcher *et al.* 1997] states an upper limit to the XRB fluctuations. Both results are shown in table 4.7.

Table 4.7: XRB Fluctuation from [Shafer 1983] and [Butcher *et al.* 1997]

Instrument	energy keV (counts/s/sr)	fraction of XRB	error
HEAO A-2	2.5–13.3	0.0014	0.0005
Ginga	4–12	0.00094	upper limit

The Ginga measurement gives a smaller upper limit than the Shafer value. The Ginga instrument has a much smaller field of view than the bins that Shafer used. Shafer used a 49 square degree field of view where the Ginga FOV is 2 square degrees. The smaller field and larger area allows the Ginga measurements to see deeper than the Shafer results. Even with these differences, the Shafer result is within one sigma of the Ginga upper limit. All the fluctuation data is combined in figure 4.3.

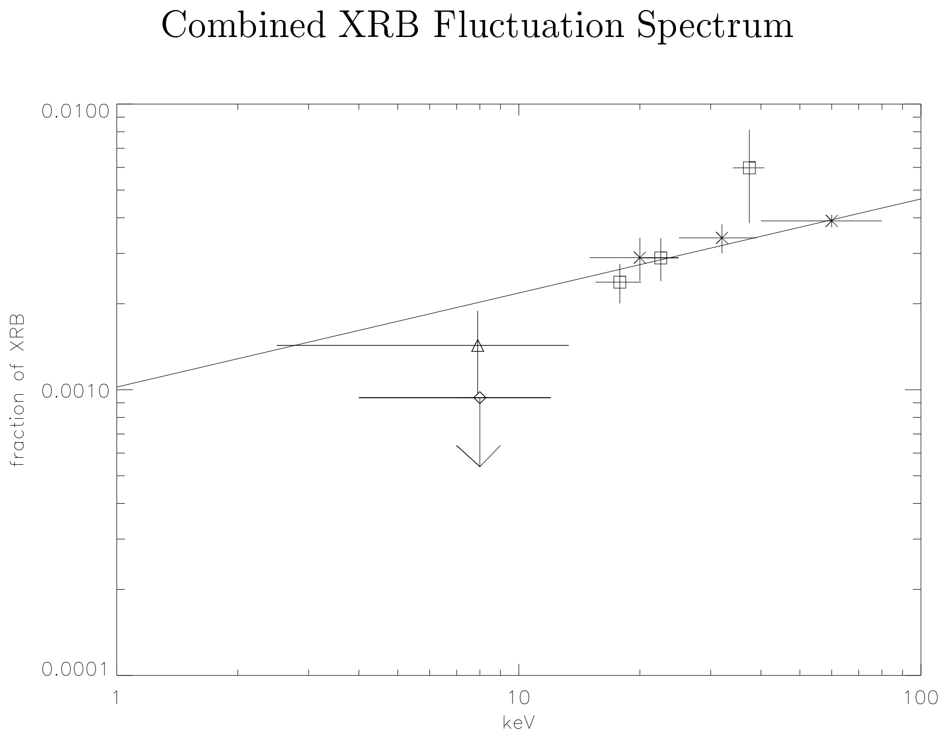

Figure 4.3: The fluctuations in the XRB from all the instruments are shown as a fraction of the XRB flux for a hypothetical 1 steradian FWHM instrument. The HEXTE data points are squares, the A4 points are crosses, The A2 point is a triangle and the Ginga upper limit is a diamond. The line is the best fit power law to the HEXTE and HEAO-1 A4 data, which has a power law index of 0.33 ± 0.09

4.2 Number Density of Sources

There are a number of different ways of calculating the mean number of contributing sources in XRB from the fluctuation measurements. The methods depend in part on different instrument and observing quantities such as the source detection threshold and the sky coverage of the observations. The most constraining method is by fitting the data to the P(D) distribution directly [Condon 1974]. The shape of the P(D) distribution is modeled by the fit parameter to the log N – log S distribution. Unfortunately, the symmeterizing of the HEXTE results caused by the inability to differentiate positive from negative fluctuations renders this method insensitive given our convolved data $\frac{1}{2}(P(D)+P(-D))$. Older methods of finding source counts from fluctuation measurements relied on the relative intensity of the fluctuations $\frac{\delta I}{I}$. These methods are better suited to the HEXTE data. The general method calculates the number of sources from the size of the fluctuations, which is derived in section 5.1. There are a number of ways of making this calculation based on different assumptions about the source distribution, but all have the same functional relation between the number of sources and the fractional fluctuations (see section 5.1.2).

The simplest model calculation, derived in section 5.1.2 assumes a flux I and its fluctuation δI arise from N objects with equal *apparent* luminosity. Ω is the field of view of the instrument.

$$N = \frac{4\pi}{\Omega}\left(\frac{I}{\delta I}\right)^2 \tag{4.1}$$

This model makes unrealistic assumptions about the source distribution, but requires the fewest instrument properties in its calculation and is a good comparative measurement, although less constraining on the absolute number of sources. The important feature of this study is the relative number of sources at different energies, so the absolute number of sources in the background is not critical to the interpretation I make here. Since all the source distribution models have the same relation between the number of sources and the fractional fluctuations:

$$N \propto \left(\frac{I}{\delta I}\right)^2$$

I will proceed with this the simple relation in equation 4.1.

Figure 4.4 shows the HEXTE source number count using this simple model of uniform apparent luminosity. The best fit power law index to this spectrum (table 4.8) is -1.79 $\pm$ 0.07. Although this index has a small formal error, this is not a very constraining measurement since there is only one degree of freedom in the three data point system with two fit variables, the normalization and the power law index.

Table 4.8: Number Count from HEXTE

band	energy keV	number of sources	error
1a	15.5–20.2	2.3x10^6	7.4x10^5
1b	20.2–24.9	1.7x10^6	5.4x10^5
1	15.5–24.9	1.9x10^6	4.4x10^5
2	34–41	5.2x10^5	3.3x10^5

The error measurements for this unrealistic model are formal and should be used in comparison between the different datasets and for the dependence on energy, not as a definite statement about the number of sources on the sky. Since the number of sources in all the models [Fabian 1972] [Schwartz and Gursky 1974] [Schwartz, Murray, and Gursky 1976] [Barcons and Fabian 1988] using the fraction-

HEXTE XRB Source Count Spectrum

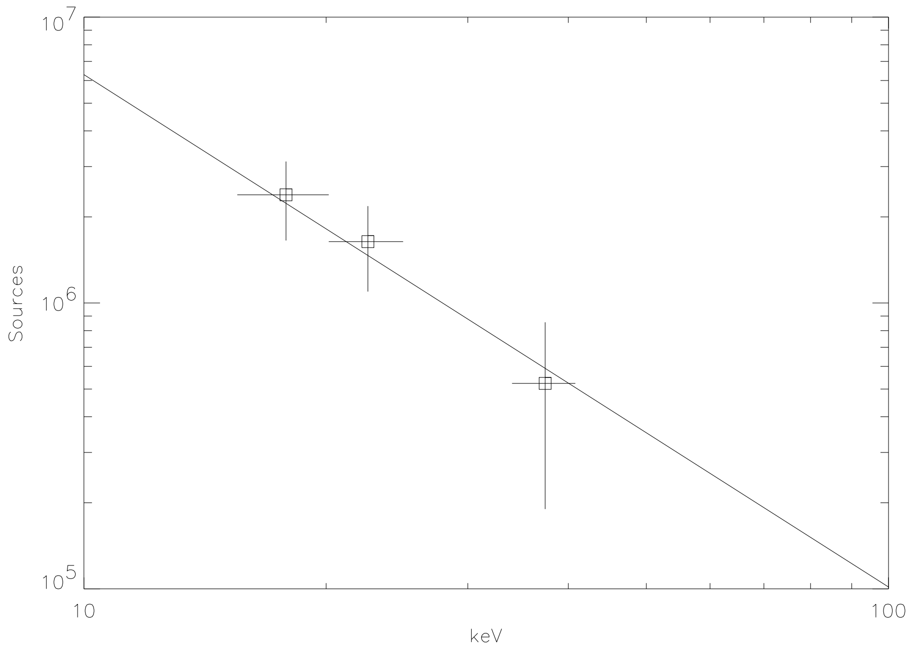

Figure 4.4: The number of XRB sources as a function of energy for the divided lowest HEXTE energy bands. The line is the best fit power law with index -1.79

al fluctuations depend on the square of the fractional fluctuations, the errors are valid for the calculations of the power law index.

Comparison to Previous Results

The HEAO-1 A4 data, table 4.9, agrees well with the HEXTE results, as expected from the agreement in the fluctuation measurements. The combined results have a power law spectral index of -0.64 $\pm$ 0.20 as seen in figure 4.5.

Schwartz's lower limits, shown in table 4.10, are well below the other experiments reported measurements and will not be considered further.

Table 4.9: Number counts for HEAO-1 A4 data

band	energy keV	Number Counts	error
1	15–25	1.6×10^6	5.4×10^5
2	25–40	1.1×10^6	2.6×10^5
3	40–80	8.3×10^5	8.6×10^4
4	80–160	1.3×10^5	8000

Table 4.10: Number counts lower limits from OSO-3

band	energy keV	Number Count
2	7.7–12.5	2.1×10^5
3	12.5–22	4.5×10^5
4	22–38	2.7×10^5
5	38–65	1.0×10^5
6	65–113	5347

Since a smaller fractional fluctuation measurement gives a larger number of sources, the upper limit to the fluctuations from GINGA becomes a lower limit to the number of sources. The HEAO-1 A2 and the GINGA data are shown in table 4.11. The HEAO-1 A2 measurement fits well with the the power law calculated from the HEXTE and HEAO-A4 data but the Ginga results would indicate an increased power law index. Fitting the Ginga data would increase the χ^2 of the fit and would possibly require a more complex model. The combined spectrum of all

Table 4.11: Number Count for Shafer and Butcher data

Instrument	energy keV	Number Count	error
HEAO A-2	2.5–13.3	8×10^6	4×10^6
Ginga	4–12	1.4×10^7	lower limit

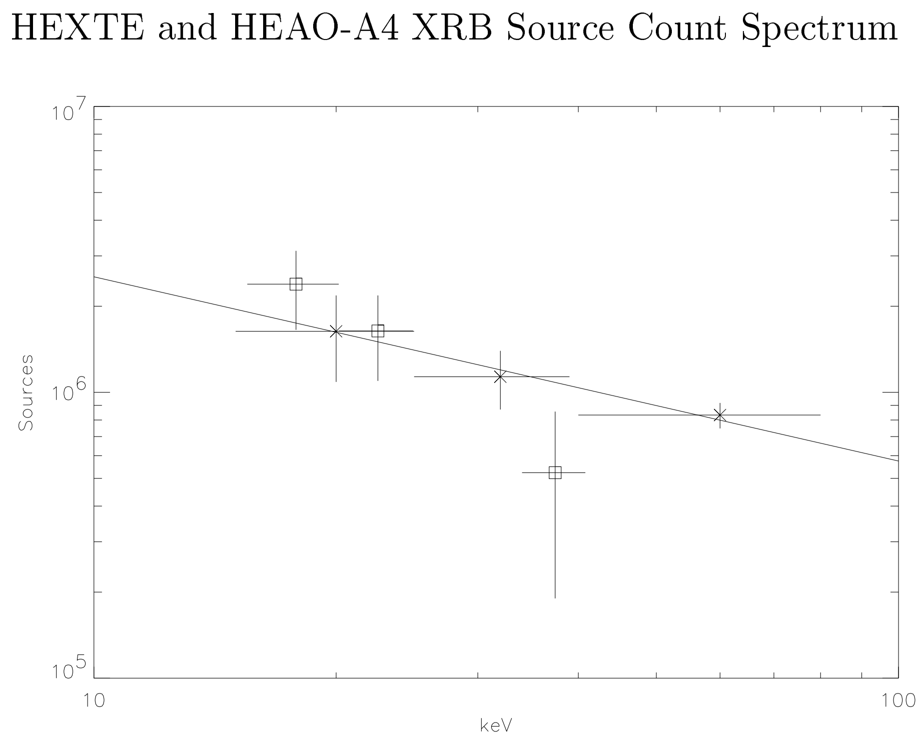

Figure 4.5: The number of XRB sources as a function of energy for the HEXTE and HEAO-1 A4 data. The HEXTE data points are squares and the HEAO points are crosses. The line is the best fit power law to the combined data set, which has a power law index of -0.64 $\pm$ 0.20.

the references is shown in figure 4.6.

This decreasing number of sources is in direct disagreement with the popular model of the XRB which predicts that the XRB flux is modeled to be dominated in this energy range by a population of Seyfert 2 galaxies (section 5.2.3). Figure 4.7 shows a model curve of the number of sources expected by applying equation 4.1 to the fluctuations calculated in section 5.2.3 from parameters in the Zdziarski model component fit to the XRB. This curve is one of a family of curves that can be shifted in total source counts by varying the model parameters, but the shape

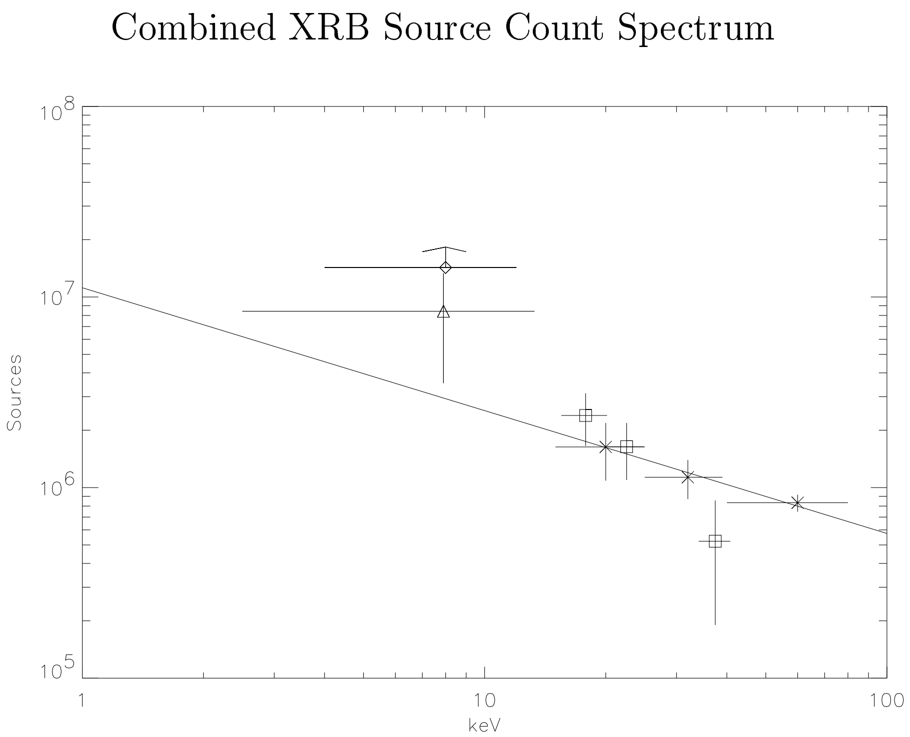

Figure 4.6: The number of XRB sources as a function of energy for all the data sets. The HEXTE data points are squares, the A4 points are crosses, The A2 point is a triangle and the Ginga lower limit is a diamond. The line is the best fit power law to the HEXTE and HEAO-1 A4 data, which has a power law index of -0.64 $\pm$ 0.20.

of the curve is based on the number of sources in the population which dominates the flux of the XRB. For all the recent models of the sources of the XRB, this curve would be flat or slightly increasing in the 15 – 80 keV energy range. The data show a greater than 3σ disagreement with this type of model.

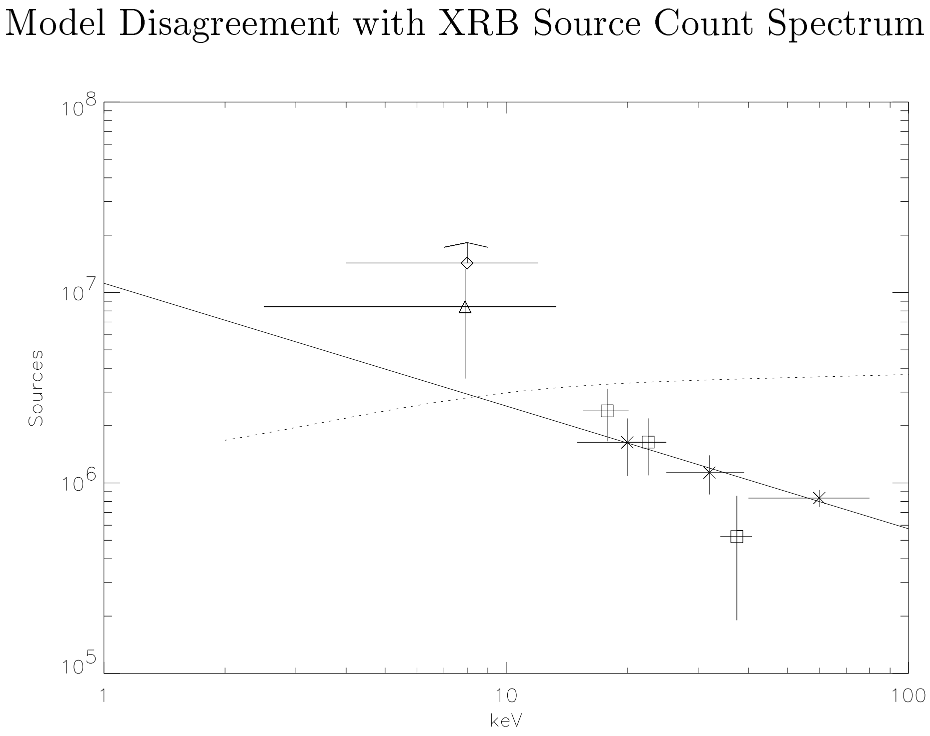

Figure 4.7: The number of XRB sources as a function of energy for all the data sets. The HEXTE data points are squares, the A4 points are crosses, The A2 point is a triangle and the Ginga lower limit is a diamond. The solid line is the best fit power law to the HEXTE and HEAO-1 A4 data, which has a power law index of 0.64 $\pm$ 0.20. The dotted line is the expected source number curve calculated in section 5.2.3 from the Zdziarski model.

Chapter 5

Discussion

The analysis and results chapters have used the relations between an ensemble of sources and the field that it creates. This relation has been approached in different ways. These relations will be discussed, first as a prediction of the fractional fluctuation in the field from a distribution of the sources and secondly from the shape of the fluctuation distribution. [Scheuer 1957] first devised the method of calculating the probability distributions, P(D), for analysis of radio observations. Scheuer adapted the technique to x-ray analysis in [Scheuer 1973]

The broad band measurements of the XRB will be shown and the prevalent model for the XRB will be discussed. The unification model of Seyfert 1 and Seyfert 2 galaxies and the prediction of the changes in the number of sources expected from this relation, in particular, will be considered.

5.1 Source Distributions

In the simplest hypothetical case, the XRB is composed of a set of identical, uniformly distributed sources. If there are N sources in an observed field of view Ω, The expected variation on a random field will be determined by Poisson statistics and will approach $\sqrt{N}$ for large values of N. The fractional variation in a field will be $\frac{1}{\sqrt{N}}$. So the size of the variations can be used to determine the density of sources. Since N scales with the field of view the fluctuations are proportional to $\frac{1}{\sqrt{\Omega}}$.

The calculation of the expected fluctuations depends on the spatial distribution of the sources. Beginning with the simplest example where the sources are distributed evenly within a volume, I outline the relation of the number of sources N to the flux, S, of the sources which create the field, where the luminosity of the individual sources is L and the intrinsic spatial density of the sources is ϕ. The number count (N) of sources, in differential form is :

$$dN = \phi(L)\, dL\, dV \tag{5.1}$$

For a shell at radius r this becomes

$$dN = \phi(L)\, dL\, 4\pi r^2\, dr \tag{5.2}$$

The flux S at a distance r is

$$S = \frac{L}{4\pi\, r^2} \tag{5.3}$$

giving

$$r = \sqrt{\frac{L}{4\pi\, S}} \tag{5.4}$$

for a specific L and

$$dr = -\frac{1}{2}\sqrt{\frac{L}{4\pi}}\, S^{-\frac{5}{2}}\, dS \tag{5.5}$$

Substituting into 5.2

$$dN = -\phi(L)\, dL\, 2\pi \left(\frac{L}{4\pi}\right)^{\frac{3}{2}}\, S^{-\frac{5}{2}}\, dS \tag{5.6}$$

and integrating over L gives

$$dN = -\frac{2}{3}\, K\, S^{-\frac{5}{2}}\, dS \tag{5.7}$$

where

$$K = \int \frac{3L^{\frac{3}{2}}\phi(L)\, dL}{4(4\pi)^{\frac{3}{2}}} \tag{5.8}$$

Integrating over S

$$N(> S_0) = -\int_{S_0}^{\infty} -\frac{2}{3} K\, S^{-\frac{5}{2}}\, dS \tag{5.9}$$

gives

$$N(> S_0) = K\, S_0^{-\frac{3}{2}} \tag{5.10}$$

The form of equation 5.7 is for a uniform spatial distribution of sources in a Euclidean space. To generalize the equation for non-uniform spatial distributions or as well for the effects of a non-Euclidean space, the exponent is allowed to vary.

$$\frac{dN(S)}{dS} \propto S^{-\beta} \tag{5.11}$$

where $\beta = 2.5$ for a uniform distribution.

For this distribution of sources, [Scheuer 1973] derived the relation between the normalization and power law parameters and the distribution of the fluctuations P(D).

5.1.1 Probability Distribution P(D)

From the distribution of sources in equation 5.10 Scheuer derived the shape of the probability distribution P(D).

$$P(D) = \frac{1}{\pi(\beta-1)} \sum_{r=0}^{\infty} \frac{(t-1)!\, sin(t\pi)\, D^r}{(K\Omega_{eff}(-\beta)!)^t\, r!} \tag{5.12}$$

where

$$t = \frac{r+1}{\beta-1} \tag{5.13}$$

and

$$\Omega_{eff} = \frac{2}{\beta(\beta+1)}\Omega \tag{5.14}$$

The probability distributions for three different values of β are shown in figure 5.1. For data histograms such as those from [Butcher *et al.* 1997] (figure 5.2), the best K and β parameters can be found.

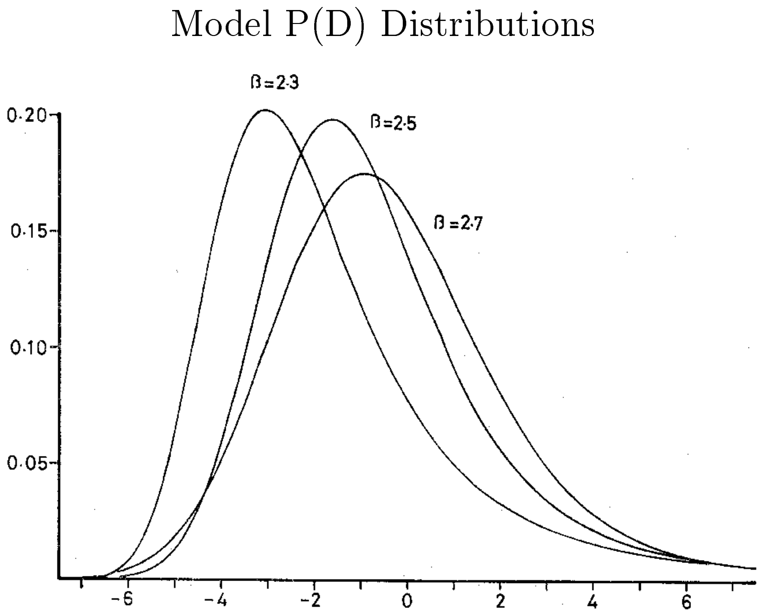

Figure 5.1: The probability distribution vs count rate for the power laws $\frac{dN(S)}{dS} \propto S^{-\beta}$ for three different power law indices. From [Scheuer 1973]

For the data in our study, the sign of the flux measurements is not known (see

Example P(D) Distribution

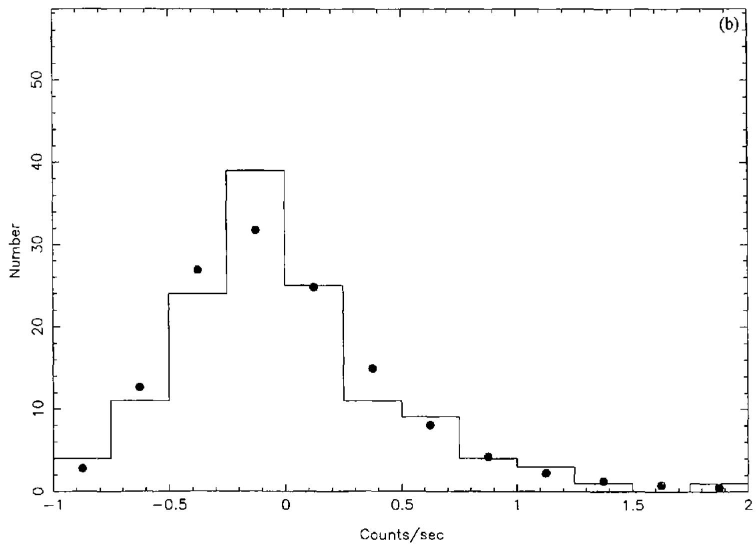

Figure 5.2: The measured P(D) histogram for the 4–12 keV band in Ginga. The points are the best fit P(D). From [Butcher *et al.* 1997]

section 3.3.3), the P(D) distribution is symmetric. The symmetrical P(D) is equivalent to $\frac{1}{2}(P(D) + P(-D))$. Figure 5.3 is an example of one of these convolved probability distributions. Since the convolved distribution is insensitive to the fit parameters K and β, other techniques must be used to find the number of sources from our data.

5.1.2 Counts of Sources from Fractional Fluctuations

The number of sources can be calculated from the level of fractional fluctuations for simple assumptions about the source distribution. For source distributions more complex than that of uniform apparent luminosity, the calculation of the volume over which to integrate the source population becomes a major factor.

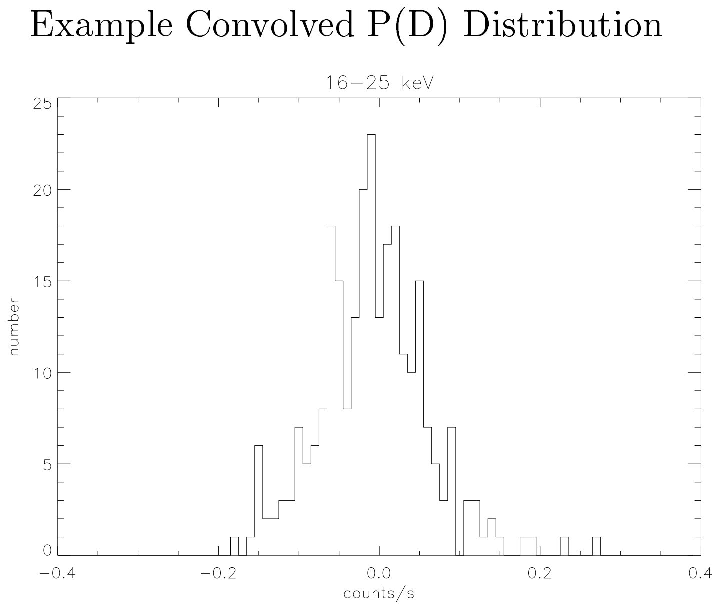

Figure 5.3: This histogram of the HEXTE data from 15.5–24.9 keV which is dominated by sky fluctuations can be seen to be symmetric as compared to the shape of the P(D) distribution shown in figures 5.1 and 5.2.

I will begin with the relation for a source population with a single uniform apparent luminosity that is used in section 4.2, and will compare this results to the more sophisticated models.

Uniform Apparent Luminosity

The simplest case is where a signal is made up of N identical sources of luminosity L. For a field of view Ω The signal $I = nL$. Where :

$$n = \frac{\Omega}{4\pi} N \tag{5.15}$$

The Poisson error on the number n approaches $\sqrt{n}$ for large values of n. The variation in the signal, δI, approaches $\sqrt{n}L$ and the fractional fluctuation is :

$$\frac{\delta I}{I} = \frac{1}{\sqrt{n}} \tag{5.16}$$

$$\frac{\delta I}{I} = \frac{1}{\sqrt{\frac{\Omega}{4\pi} N}} \tag{5.17}$$

$$N = \frac{4\pi}{\Omega} \left(\frac{I}{\delta I} \right)^2 \tag{5.18}$$

Although this source model is unrealistic, the functional relation between N and the fractional fluctuations, $N \propto \left(\frac{I}{\delta I}\right)^2$, remains unchanged in models with a more complex source distribution. This is important since the results rely on the relation between N and the fractional fluctuations, not on the value of N.

Uniform Sources in a Volume

For a more realistic situation, the sample is drawn from sources uniformly distributed within a sphere of radius R_{max}. The closest source is at a distance R_{min}.

The number of sources, from [Schwartz and Gursky 1974], is:

$$N = \frac{4\pi p}{3\Omega} \left(\frac{I}{\delta I} \right)^2 \frac{R_{max}}{R_{min}} \tag{5.19}$$

where

$$p = \frac{< j^2 >}{< j >^2} \tag{5.20}$$

The parameter p allows inclusion of arbitrary luminosity distributions, represented by j, where the j expectation values are taken over the source average of luminosity values [Schwartz *et al.* 1971].

Allowances can be made for the effect of the shape of the detector response function by introducing an effective area Ω_{eff} which is defined by [Condon 1974] as:

$$\Omega_{eff} = \int [f(\theta,\phi)]^{\beta-1} d\Omega \tag{5.21}$$

where $f(\theta, \phi)$ is the response function normalized to unity at the peak.

For the purposes of this study, the important information from these different models is that N is still proportional to the inverse square of the fractional fluctuations. The refinements in the calculation of the number density will not affect the power law index of the number density spectrum.

5.2 Broadband XRB

The spectrum of the XRB from x-rays to gamma-rays can be seen in figure 5.4 from [Zdziarski *et al.* 1995]. The ordinate is in units of constant energy per decade, so that the peak in the energy per decade near 40 keV can be seen. Figure 5.5 from

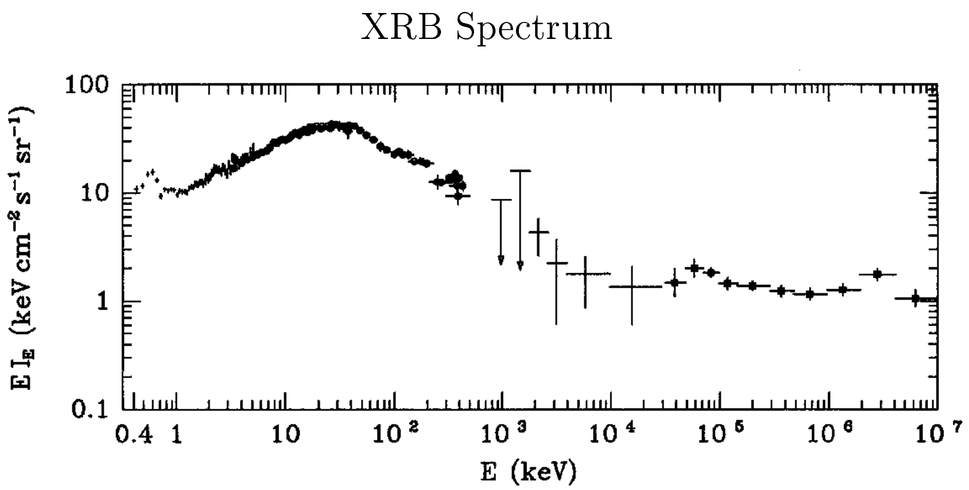

Figure 5.4: The XRB over a wide energy range from less than 1 keV to 10 GeV. The figure shows data from a number of different satellite based and balloon based instruments. From [Zdziarski *et al.* 1995].

[Gruber *et al.* 1999] shows the XRB from 1 to several hundred keV with the peak in the energy flux. Gruber also created a piecewise empirical fit to the XRB spectrum, given in units of keV/(cm^2-s-keV-sr) :

$$7.877E^{-.29} * e^{-E/41.13} \qquad\qquad 3keV < E < 60keV$$

and

$$0.0259(E/60)^{-5.5} + 0.504(E/60)^{-1.59} + 0.0288(E/60)^{-1.05} \qquad 60keV < E < 6000keV,$$

which is shown as the solid line in figure 5.5. The functional form for the lower energy portion was developed by [Boldt 1987].

The difficulty in finding the sources which create the XRB is that the spectral

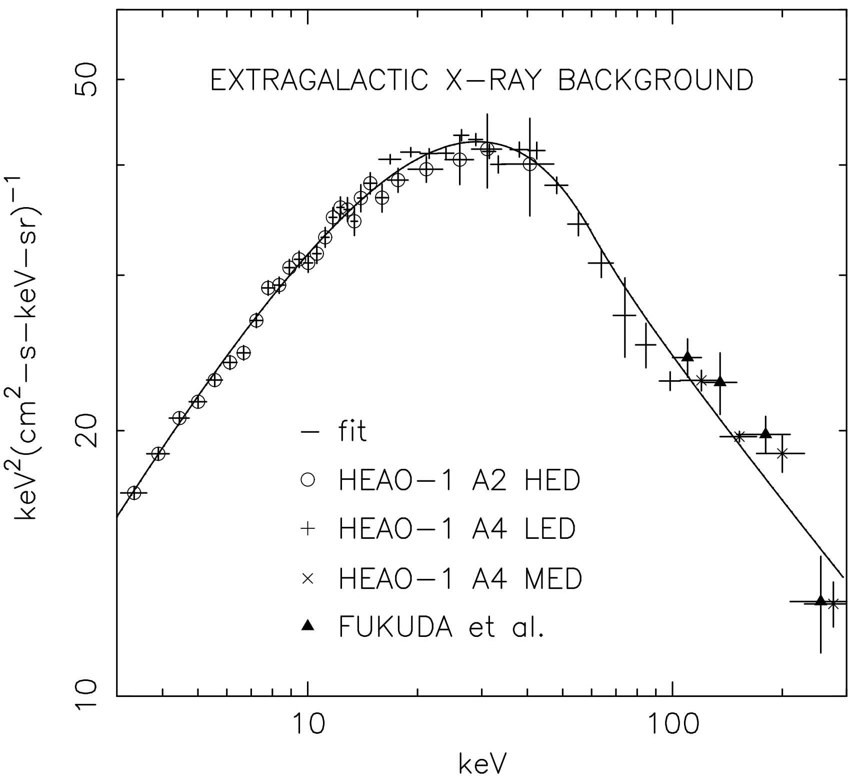

Figure 5.5: The spectrum of the XRB from HEAO-1 is shown with Grubers empirical fit in units of constant energy per decade. From [Gruber *et al.* 1999].

shape of the XRB doesn't fit the shape of any known class of sources. Up till now, the most promising model of the XRB has been emission from different classes of active galaxies[Comastri *et al.* 1995] [Zdziarski 1996] [Gilli, Risaliti, and Salvati 1999] (and others). This model has difficulty in the 10 to few hundred keV energy range where the majority of the energy flux in the XRB is. In this energy range the modeled XRB is dominated by the emission from Seyfert galaxies, a classification of active galaxies. These models rely on the active galaxy unification model to predict the relative contributions of the different types of Seyfert galaxies.

5.2.1 Unified AGN Model

[Lawrence 1987] was the first to try to explain the widely varied classes of AGN as arising from a single model. The model had to work for objects whose luminosities varied by several orders of magnitude and which display a wide variety of different phenomenologies such as broad and narrow optical emission lines, soft and hard x-ray flux and superluminal jets. The part of this model that is of interest to this study deals with the unification of type 1 and type 2 Seyfert galaxies.

Seyfert Unification Model

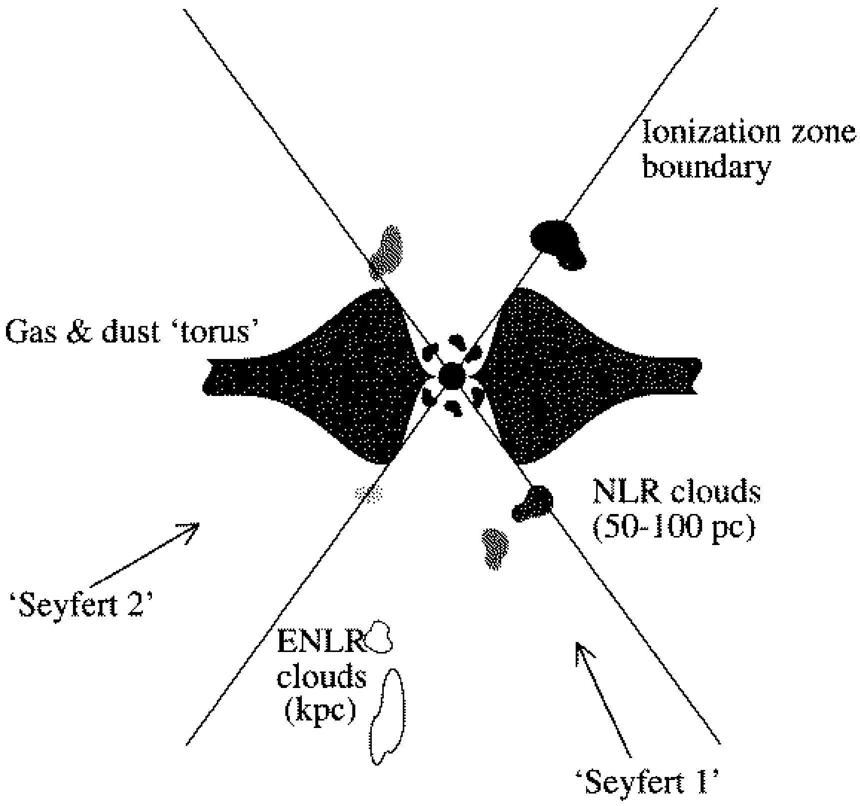

Figure 5.6: Model of the difference between Seyfert 1 and Seyfert 2 galaxies based on viewing angle. From [Peterson 1997].

The basic components of any unified AGN model are a massive black hole of $\sim 10^{6}\ M_{\odot}$ with an accretion disk surrounded by a large torus of material (see figure 5.6). There are clouds of material both near the compact object, the broad line region, and farther away, the narrow line region.

Seyfert galaxies are classified by their optical properties. Amongst their defining properties, Seyfert 1 galaxies have both broad and narrow emission lines (Figure 5.7) while Seyfert 2 galaxies have only narrow emission lines (top panel of figure 5.8).

Seyfert 1 Spectrum

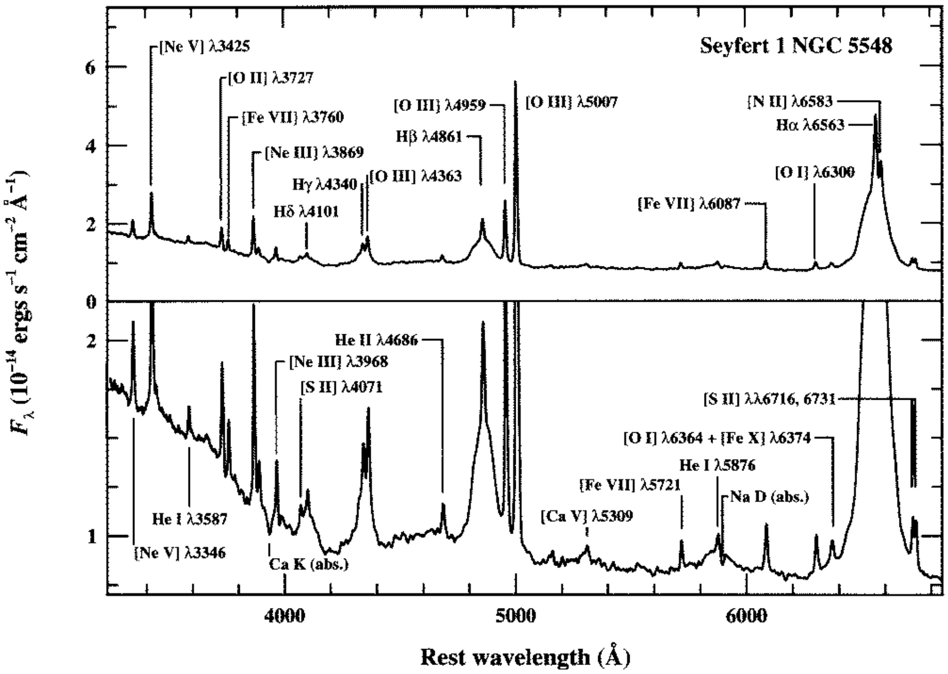

Figure 5.7: Optical spectrum of NGC 5548. The figure shows narrow and broad emission lines, for example the Hβ line. From [Peterson 1997].

The unification model explains this difference in the optical properties of the galaxies by considering a single underlying object that appears as a Seyfert 1 when viewed from some angles and as a Seyfert 2 when viewed from others. The broad lines in the Seyfert 1 spectra are modeled as originating close to the nucleus of the active galaxy (AGN) where the material is hot so the lines are thermally broadened. The angles that define the Seyfert 2 have the 'torus' of material between the broad line clouds and the line of sight. The evidence to support this comes from the polarized spectra of Seyfert 2s. Singly scattered light is polarized, so that one would expect that the light from near the core that was scattered into the line of sight would show the broad lines typical of a Seyfert 1.

Figure 5.8 shows this evidence of Seyfert 1 type broad lines in the polarized light from a Seyfert 2 spectrum.

The x-ray spectra, which show evidence for a much larger column of material in the line of sight to the Seyfert 2 galaxies [Zdziarski *et al.* 1995] also support this model (figure 5.9). The opening angle of the torus therefore determines the ratio of the two different types of Seyfert galaxies.

5.2.2 Ratio of Seyfert 1's to Seyfert 2's

The number ratio of type I AGN to type II counterparts should be determined by the average solid angle for obscuring the compact source of the AGN by the torus (see figure 5.6). From optical surveys (table 5.1), the ratio of Seyfert 2 s to Seyferts 1s is observed to be about 2.5 : 1. Since the x-rays are more penetrating, the

Seyfert 2 and Hidden Seyfert 1 Spectrum

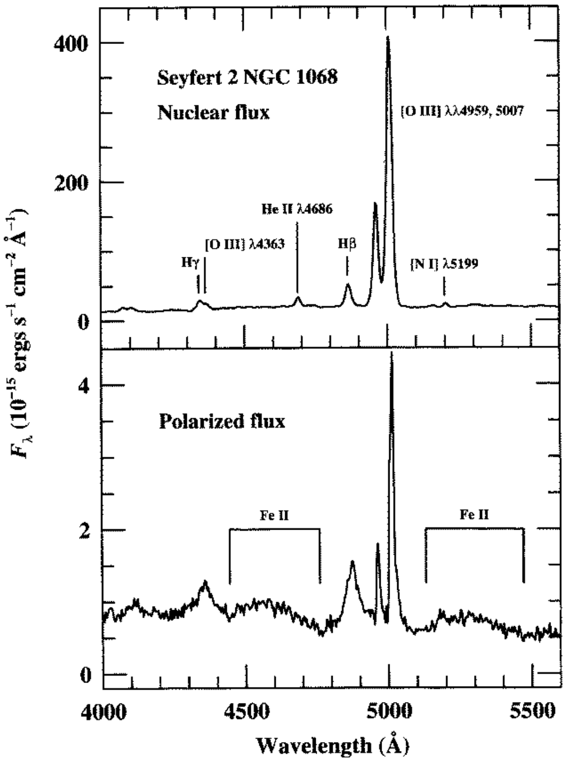

Figure 5.8: The top panel is an optical spectrum of the Seyfert 2 galaxy NGC 1068. The bottom panel shows the polarized spectrum of the same source which shows the broad emission lines typical of Seyfert 1 galaxies. From [Peterson 1997].

opening angle of figure 5.6 should be larger or at least the same in x-rays as in the optical. Since a larger opening angle decreases the ratio of Seyfert 2s to Seyfert 1s, the optical value of 2.5 : 1 should be an upper limit.

Table 5.1: Current Spatial Densities of AGN from [Peterson 1997]

Class	$h_0^3\ Gpc^{-3}$
Radio Quiet	
Seyfert 2	8 x 10^5
Seyfert 1	3 x 10^5
QSO	800
Radio Loud	
FR I	2 x 10^4
BL Lac	600
FR II	80
Quasars	20

5.2.3 Source Counts Predicted by Model

Since the models of the x-ray background fit the spectra and the number of sources of different classifications of AGN to create the background, these models can be used to predict the fractional fluctuations which we have measured in section 4.2.

I have used the model by [Zdziarski 1996] to estimate the fluctuations I expect in my results. He and others have determined loosely average spectral properties of classes of Seyfert galaxies which they then incorporate into a model of the spectrum of the XRB [Zdziarski *et al.* 1995]. Figure 5.10 shows their model source contributions to the XRB. The contributions shown are from different types of AGN and

Average Seyfert 1 and 2 X-ray Spectra

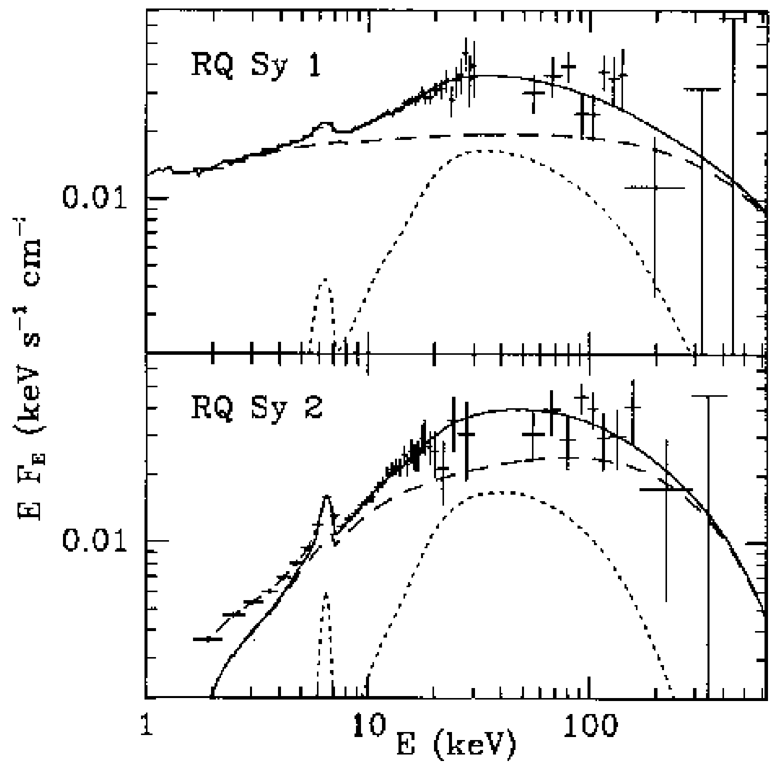

Figure 5.9: Averaged spectra of Seyfert galaxies. The top panel is the average of 6 Seyfert 1 spectra from Ginga and OSSE. the lower panel is the average of three Seyfert 2 spectra from the same instruments. From [Zdziarski *et al.* 1995]

from type 1A supernovae. In the energy range near the 30 keV peak, the model shows the XRB as being dominated by emission from Seyfert Galaxies. The model uses the average spectra shown in figure 5.8

Model Fit to XRB Spectrum

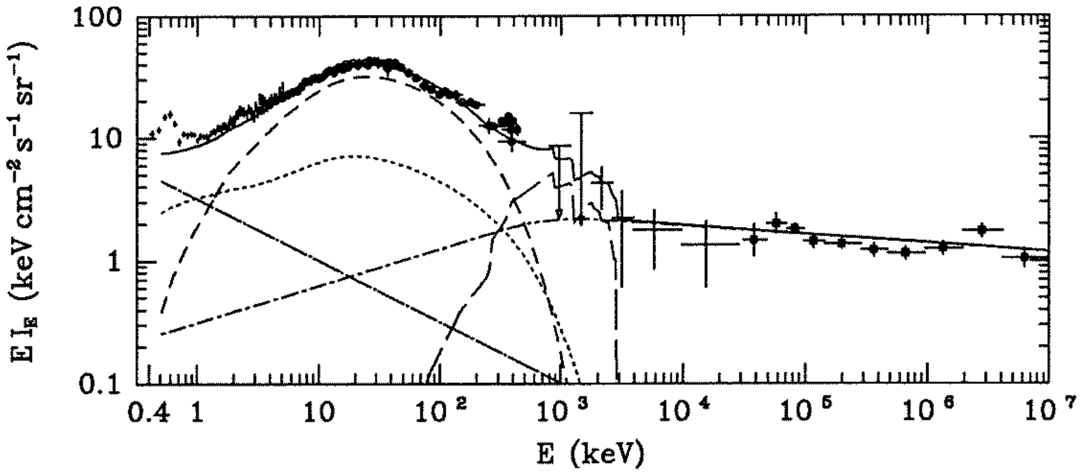

Figure 5.10: A model fit to the XRB spectrum [Zdziarski 1996] with contributions from different classes of AGN. The long dashed-dotted line is the QSO component. The short dashed-dotted line is the Blazar component. The short dashed line is the Seyfert-1 galaxies and the long dashed line is the remainder which [Zdziarski 1996] model as Seyfert-2 galaxies. Normalizations for the different spectral components have been adjusted to fit the data.

The model by [Zdziarski 1996] employs an adjustment to the ratio of Seyfert 1s to Seyfert 2s of 5 to 1. This large ratio is required for the less luminous Seyfert 2 galaxies to make up half of the flux of the XRB at a few keV and the majority of it between 10 and 300 keV.

To compare the fluctuations expected from this model to my measurements, I created a simple program which took the average source spectra and the expected numbers in the ratio in the model and calculated the fluctuations. It then used the same calculation of the number of sources which I used on my fluctuation measurements (see section 4.2) and found a family of curves which represented the model. Figure 5.11 which is the same as 4.7 shows a representative expected curve from the

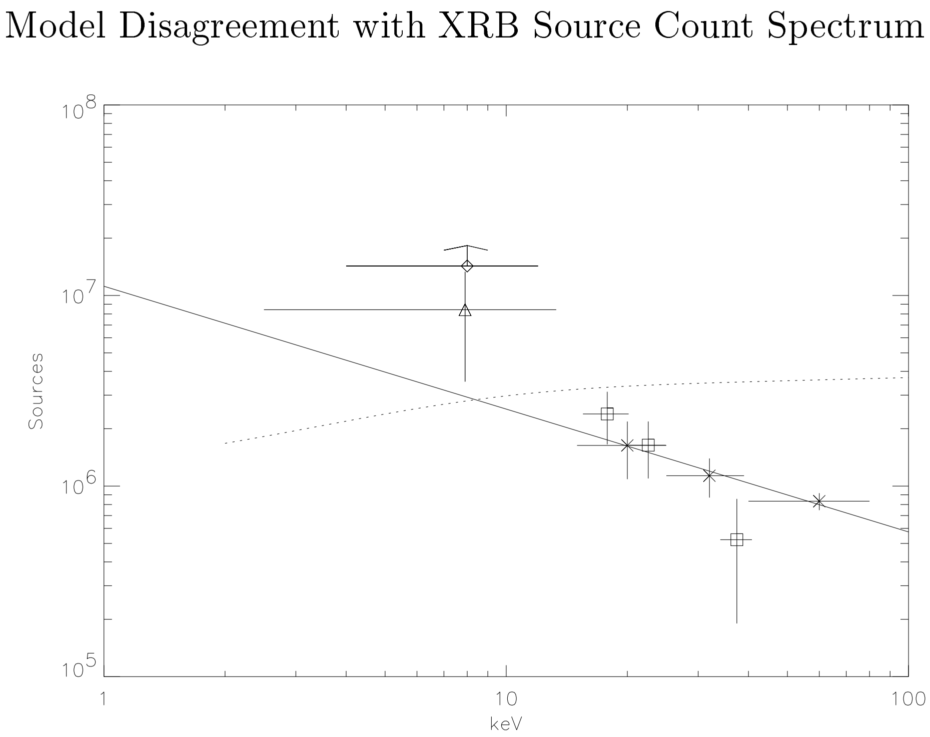

Figure 5.11: The number of XRB sources as a function of energy for all the data sets. The HEXTE data points are squares, the A4 points are crosses, The A2 point is a triangle and the Ginga lower limit is a diamond. The solid line is the best fit power law to the HEXTE and HEAO-1 A4 data, which has a power law index of 0.64 $\pm$ 0.20. The dotted line is the expected source number curve calculated in section 5.2.3 from the Zdziarski model.

XRB model. Since the Seyfert 2 component of the XRB dominates the model in the 10 to 100 keV energy range, the curve is just a constant — the number of Seyfert 2 galaxies. The combined HEXTE and HEAO-1 A4 data show a 3σ disagreement with this model and indicate a population of less numerous, and for that reason, necessarily brighter sources as the dominant source of the XRB in the 15 to 80 keV range. I compare the relative number of sources with energy instead of the absolute number of sources since the spectral relation does not have the tuning parameters which enter into the calculation of the absolute number of sources.

5.3 Fluctuations Predicted by HEAO-1 A2

Table 5.2: Predicted Fluctuations

Band	Energy (keV)	XRB Model count rate (c/s)	Anticipated Fluctuation (c/s)	HEXTE Detector Background (c/s)
1a	15.5–20.2	0.158	0.013	4.06
1b	20.2–24.9	0.109	0.009	3.54
1	15.5–24.9	0.267	0.021	7.60
2	34–41	0.048	0.004	8.71
3	80–132	0.023	0.002	17.7
4	132–261	0.0054	0.0004	42.8

Early on in the accumulation of the data, I needed an idea of the level of the fluctuations I expected, to determine if I could see 'deep' enough to measure these fluctuations. I used the fluctuation level from the HEAO-1 A2 data [Shafer 1983] as an estimate. Table 5.2 shows the extrapolation of the expected fluctuations, which turned out to be smaller than the measurements (see figure 4.7).

Chapter 6

Conclusions

XRB Fluctuations

The fluctuations in the x-ray background for three wide energy bands have been determined. They are 13.0 $\pm$ 2.1 % of XRB flux from 15.5 to 20.2 keV, 15.8 $\pm$ 2.7 % from 20.2 to 24.9 keV and 32 $\pm$ 11 % from 34 to 41 keV for a 1.1 square degree field of view.

Number Counts of XRB Sources

The spectrum of the source density when combined with data from the HEAO-1 A4 instrument results in an energy power law spectral index to the number of sources of -0.64 $\pm$ 0.20 from 15 to 80 keV. This result is in direct disagreement with models of the XRB in which the emission in this energy range is dominated by a class of sources more numerous than Seyfert 1s.

Wishful Thinking

A survey with a large sky coverage is needed to improve the fluctuation measurements made with large fields of view with the HEAO-1 satellite. Since a smaller field of view is more sensitive to the fluctuation, an imaging instrument with a large field of view would be able to more sensitively measure fluctuations.

An imaging instrument a such as ABRIXAS using grazing incidence mirrors with response up to 100 keV would be the best of both worlds, giving a large sky coverage with small resolution elements. Such an instrument would be able to put the number count problem to rest along with making a measurement of the dipole moment of the distribution and would be able to place limits on the large scale structure of the early universe.

Bibliography

[Barcons and Fabian 1988] Barcons, X. and Fabian, A. C. 1988, *MNRAS*, **230**, 189–206.

[Boldt 1987] Boldt, E. 1987, *Phys. Reports*, **146**, 215.

[Butcher *et al.* 1997] Butcher, J. A. *et al.* 1997, *MNRAS*, **291**, 437–445.

[Carrera, Fabian, and Barcons 1997] Carrera, F., Fabian, A. C., and Barcons, X. 1997, *MNRAS*, **285**, 820–830.

[Comastri *et al.* 1995] Comastri, A., Setti, G., Zamorani, G., and Hasinger, G. 1995, *A&A*, **296**, 1–12.

[Condon 1974] Condon, J. J. 1974, *ApJ*, **188**, 279–286.

[Fabian 1972] Fabian, A. C. 1972, *Nature Phys. Sci.*, **237**, 19.

[Fabian and Barcons 1992] Fabian, A. C. and Barcons, X. 1992, *ARA&A*, **30**, 429.

[Giacconi *et al.* 1962] Giacconi, R., Gursky, H., Paolini, F. R., and Rossi, B. 1962, *Phys.Rev.Lett*, **9**, 439–443.

[Giacconi and Zamorani 1987] Giacconi, R. and Zamorani, G. 1987, *ApJ*, **313**, 20–27.

[Gilli, Risaliti, and Salvati 1999] Gilli, R., Risaliti, G., and Salvati, M. 1999, A&A in Press.

[Gould 1967] Gould, R. J. 1967, *Amer. J. of Phys.*, **35**, 376.

[Gruber 1992] Gruber, D. E. 1992. The hard x-ray background. in *The X-ray Background*, ed. X. Barcons and A. C. Fabian, 44 – 53. Cambridge university press.

[Gruber *et al.* 1996] Gruber, D. E., Blanco, P. R., Heindl, W. A., Pelling, M. R., Rothschild, R. E., and Hink, P. L. 1996, *A&AS*, **120**, 641–644.

[Gruber *et al.* 1999] Gruber, D. E., Matteson, J. L., Peterson, L. E., and Jung, G. V. 1999, ApJ. in Press.

[Guilbert and Fabian 1986] Guilbert, P. W. and Fabian, A. C. 1986, *MNRAS*, **220**, 439–451.

[Heindl 1999] Heindl, W. A. 1999. Private Communication.

[Henry 1971] Henry, P. S. 1971, *Nature*, **231**, 516–518.

[Hink *et al.* 1991] Hink, P. L., Rothschild, R. E., Pelling, M. R., MacDonald, D. R., and Gruber, D. E. 1991, in *EUV,X-Ray, and Gamma-Ray Instrumentation for Astronomy II*, volume 1549, SPIE, 193–202.

[Jahoda *et al.* 1996] Jahoda, K., Swank, J. H., Giles, A. B., Stark, M. J., Strohmayer, T., and Zhang, W. 1996, *Proc. SPIE*, **2808**, 5.

[Lahav, Piran, and Treyer 1997] Lahav, O., Piran, T., and Treyer, M. A. 1997, *MNRAS*, **284**, 499–506.

[Lawrence 1987] Lawrence, A. 1987, *PASP*, **99**, 309–334.

[Levine *et al.* 1996] Levine, A. M., Bradt, H., Cui, W., Jernigan, J. G., Morgan, E. H., Remillard, R., Shirey, R. E., and Smith, D. A. 1996, *ApJ*, **469**, L33–L36.

[Marshall *et al.* 1980] Marshall, F. E., Boldt, E. A., Holt, S. S., Miller, R. B., Mushotzky, R. F., Rose, L. A., Rothschild, R. E., and Serlemitsos, P. J. 1980, *ApJ*, **235**, 4–10.

[Mather *et al.* 1994] Mather, J. C. *et al.* 1994, *ApJ*, **420**, 439–444.

[Mather *et al.* 1990] Mather, J. C. *et al.* 1990, *ApJ*, **354**, L37–L40.

[Pelling, Rothschild, and MacDonald 1991] Pelling, M. R., Rothschild, R. E., and MacDonald, D. R. 1991, in *EUV,X-Ray, and Gamma-Ray Instrumentation for Astronomy II*, volume 1549, SPIE, 134–146.

[Penzias and Wilson 1965] Penzias, A. A. and Wilson, R. W. 1965, *ApJ*, **142**, 419.

[Peterson 1997] Peterson, B. M. 1997, *An Introduction to Active Galactic Nuclei*, (: Cambridge university press).

[Press *et al.* 1988] Press, W. H., Flannery, B. P., Teukolsky, S. A., and Vetterling, W. T. 1988, *Numerical Recipes in C : The Art of Scientific Computing*, (: Cambridge University Press).

[Rothschild *et al.* 1998] Rothschild, R. E., Blanco, P. R., Heindl, W. A., MacDonald, D. R., Marsden, D. C., Pelling, M. R., Wayne, L. R., and Hink, P. L. 1998, *ApJ*, **496**, 538–549.

[Rothschild, Pelling, and Hink 1991] Rothschild, R. E., Pelling, M. R., and Hink, P. L. 1991, in *EUV,X-Ray, and Gamma-Ray Instrumentation for Astronomy II*, volume 1549, SPIE, 120–133.

[Scheuer 1957] Scheuer, P. A. G. 1957, *Proc. Camb. Phil. Soc*, **53**, 764.

[Scheuer 1973] Scheuer, P. A. G. 1973, *MNRAS*, **166**, 329–337.

[Schmitt *et al.* 1991] Schmitt, J. H. M. M., Snowden, S. L., Aschenbach, B., Hasinger, G., Pfeffermann, E., Predehl, P., and Trumper, J. 1991, *Nature*, **349**, 583–587.

[Schwartz and Gursky 1974] Schwartz, D. and Gursky, H. 1974. The cosmic x-ray background. in *X-ray Astronomy*, ed. R. Giacconi and H. Gursky, 359 – 388. D. Reidel Publishing Company.

[Schwartz 1969] Schwartz, D. A. 1969. PhD thesis, University of California, San Diego.

[Schwartz *et al.* 1971] Schwartz, D. A., Boldt, E. A., Holt, S. S., and Serlemitsos, P. J. 1971, *Nature Phys. Sci.*, **231**, 110.

[Schwartz, Murray, and Gursky 1976] Schwartz, D. A., Murray, S. S., and Gursky, H. 1976, *ApJ*, **204**, 315–321.

[Schwartz and Peterson 1974] Schwartz, D. A. and Peterson, L. E. 1974, *ApJ*, **190**, 297–303.

[Shafer 1983] Shafer, R. A. 1983. PhD thesis, University of Maryland.

[Taylor and Wright 1989] Taylor, G. B. and Wright, E. L. 1989, *ApJ*, **339**, 619–628.

[Tytler *et al.* 1999] Tytler, D., Burles, S., Lu, L., Fan, X.-M., Wolfe, A., and Savage, B. D. 1999, *AJ*, **117**, 63–67.

[Ueda *et al.* 1998] Ueda, Y. *et al.* 1998, *Nature*, **391**, 866–868.

[Valinia and Marshall 1998] Valinia, A. and Marshall, F. E. 1998, *ApJ*, **505**, 134–147.

[Zdziarski 1996] Zdziarski, A. A. 1996, *MNRAS*, **81**, 9.

[Zdziarski *et al.* 1995] Zdziarski, A. A., niel Johnson, W., Done, C., Smith, D., and McNaron-Brown, K. 1995, *ApJ*, **438**, L63 – L66.

[Zdziarski, Zycki, and Krolik 1993] Zdziarski, A. A., Zycki, P. T., and Krolik, J. H. 1993, *ApJ*, **414**, L81–L84.

Appendix A

List of Observations

A.1 Observations

Table A.1: Observations used in Analysis

Observation	Length ksec	l	b	Smearing factor
00011 A	46	172.884	19.120	1.067
00011 B	40	172.884	19.120	1.036
00014 A	32	151.020	-12.758	1.144
0421+56 A	58	149.536	4.706	1.090
10001-02 A	43	162.939	5.155	1.001
10002 A	85	149.770	-14.565	1.002
10006-01 A	35	96.005	-8.293	1.000
10006-01 B	51	96.005	-8.293	1.046
10007-01 A	50	99.407	-39.153	1.030
10009-01 A	49	314.214	-2.226	1.010
10023-01 A	77	151.382	-9.574	1.070
10026-01 A	41	200.801	-20.018	1.353
10027-03 A	53	250.712	14.117	1.014
10032-01 A	55	303.837	33.349	1.091
10032-01 B	66	303.837	33.349	1.031
10033-01 A	38	208.868	13.932	1.000
10033-01 B	31	208.868	13.932	1.044
10033-01 C	51	208.868	13.932	1.030
10034 A	74	236.871	-30.262	1.007
10040-01 A	229	90.996	-7.211	1.080
10043 A	110	206.815	-19.336	1.079
10050-01 A	47	58.101	37.121	1.001

Table A.1: Observations used in Analysis

Observation	Length ksec	l	b	Smearing factor
10080 A	92	305.676	-45.199	1.030
10088-01 A	28	333.207	-5.312	1.031
10112-01 A	60	353.874	-5.634	1.005
10114-01 A	65	282.112	-9.367	1.165
10122-03 A	77	322.450	-0.360	1.039
10126 A	84	80.162	0.500	1.015
10133-02 A	42	2.264	4.223	1.000
10135 A	93	276.318	-32.568	1.002
10139 A	126	300.258	-43.844	1.049
10161-01 A	109	126.030	2.819	1.233
10172 A	106	136.027	1.509	1.144
10192-02 A	52	288.633	-0.672	1.001
10218 A	81	279.638	-31.976	1.007
10223-01 C	66	10.295	-0.776	1.000
10228-02 A	97	276.058	-33.282	1.027
10228-03 A	66	43.372	0.230	1.026
10291-02 A	48	92.819	-25.379	1.000
10292 A	151	217.749	55.936	1.011
10297-02 A	50	31.618	69.990	1.005
10307-01 A	28	263.262	17.373	1.000
10307-01 B	23	263.262	17.373	1.000
10307-01 E	105	263.262	17.373	1.000
10311 A	121	36.517	-30.410	1.002
10320-01 A	21	281.289	74.264	1.000
10320-01 B	25	281.289	74.264	1.000
10320-01 C	50	281.289	74.264	1.293
10320-01 D	50	281.289	74.264	1.082
10328 A	52	336.176	-21.876	1.114
10329-03 A	92	284.129	-61.717	1.009
10330 C	44	291.904	64.353	1.230
10337-01 A	23	76.475	5.541	1.000
10337-01 B	25	76.475	5.541	1.000
10337-01 C	27	76.475	5.541	1.000
10337-01 D	25	76.475	5.541	1.000
10337-02 A	12	340.128	-39.296	1.000
10337-02 B	19	340.128	-39.296	1.000
10337-02 C	21	340.128	-39.296	1.000

Table A.1: Observations used in Analysis

Observation	Length ksec	l	b	Smearing factor
10337-02 D	21	340.128	-39.296	1.000
10343-01 A	118	144.114	28.504	1.036
10345-01 C	46	180.085	65.665	1.190
1068 A	56	172.589	-51.375	1.000
1116 A	44	224.695	68.721	1.131
1259 A	80	304.558	-1.299	1.026
1538-52 A	177	327.757	1.699	1.000
1542 A	88	274.217	81.799	1.003
1624-49 A	22	335.264	-0.746	1.000
1624-49 B	29	335.264	-0.746	1.078
1728-34 A	159	354.613	-0.709	1.005
1735-44 A	114	346.395	-7.600	1.108
1820-30 A	131	3.135	-8.514	1.126
1820-30b A	119	3.135	-8.514	1.055
1822 A	73	357.177	-11.889	1.202
1822a A	11	357.177	-11.889	1.014
18325 B	209	336.176	-21.880	1.042
1837+049 A	20	36.416	4.297	1.062
1916 G	106	31.720	-9.015	1.069
1916 H	185	31.720	-9.015	1.249
20002-01 A	92	54.543	45.779	1.002
20008-01 A	62	168.593	-15.793	1.000
20008-02 A	74	348.705	21.905	1.002
20009-01 A	57	275.229	-33.066	1.000
20013-03 C	50	295.598	-48.796	1.037
20013-04 A	13	34.837	14.451	1.006
20013-04 B	30	34.837	14.451	1.024
20015-01 A	88	323.535	-54.359	1.150
20021-01 G	52	69.700	-53.648	1.454
20021-02 A	64	206.516	20.368	1.019
20022-01 A	91	53.819	-49.541	1.000
20035-01 A	191	200.631	24.216	1.001
20061-01 A	79	283.013	-32.767	1.037
20066-01 B	34	303.793	-6.683	1.219
20066-02 A	40	307.405	0.179	1.004
20083-01 A	160	353.994	-1.211	1.005
20083-01 B	153	353.994	-1.211	1.003

Table A.1: Observations used in Analysis

Observation	Length ksec	l	b	Smearing factor
20084-02 A	101	344.253	-1.914	1.013
20089-01 A	38	9.640	-6.729	1.000
20092-01 A	75	36.090	-4.689	1.066
20092-01 B	131	36.090	-4.689	1.021
20115-01 A	95	344.707	-0.288	1.009
20130 A	106	295.907	-0.326	1.033
20130 B	76	295.907	-0.326	1.638
20145-01 A	85	109.449	-0.856	1.000
20145-01 B	107	109.449	-0.856	1.542
20155-01 A	97	286.365	6.538	1.005
20155-02 A	93	180.092	-1.052	1.001
20158-01 A	47	59.624	-5.080	1.001
20163-01 A	178	78.398	2.121	1.006
20253-01 A	18	112.094	-1.954	1.000
20253-01 B	388	112.094	-1.954	1.559
20255 A	101	120.451	1.684	1.008
20256-01 A	40	4.851	6.253	1.000
20258-01 A	81	299.494	-3.168	1.065
20262-01 B	84	40.296	-3.352	1.065
2030 A	50	77.369	-1.519	1.009
20307-01 A	48	257.970	-28.408	1.000
20309-01 A	83	260.340	-17.467	1.000
20318-01 A	87	148.259	70.526	1.000
20318-02 A	96	339.891	53.231	1.006
20320-01 A	34	65.357	-59.097	1.000
20324-01 B	86	329.986	-23.672	1.043
20324-01 C	43	329.986	-23.672	1.000
20324-02 A	188	135.961	2.776	1.306
20325-01 A	63	257.930	-24.155	1.675
20326-01 A	29	137.554	69.208	1.000
20333-01 A	171	190.731	-26.754	1.104
20334-02 A	41	251.613	-34.363	1.007
20335-01 A	60	47.330	-61.814	1.000
20337-01 A	46	20.327	78.761	1.000
20348-01 A	55	349.224	12.700	1.000
2127+119 A	94	65.628	-27.612	1.085
2127+119 B	51	65.628	-27.612	1.000

Table A.1: Observations used in Analysis

Observation	Length ksec	l	b	Smearing factor
2155 B	78	18.242	-52.838	1.035
30012-01 A	54	337.191	-41.984	1.039
30021-01 A	59	309.935	20.425	1.017
herx1 A	301	58.137	37.114	1.884
30053-02 A	36	333.239	-5.333	1.000
30053-02 B	43	333.239	-5.333	1.000
30104-01 A	50	77.510	-1.448	1.009
30104-01 B	118	77.510	-1.448	1.672
30118 A	106	83.946	-2.826	1.081
30118 B	72	83.946	-2.826	1.083
30240-01 A	53	310.070	19.053	1.006
30216-01 B	126	286.125	74.410	1.069
30216-01 C	126	286.125	74.410	1.020
30407-01 A	100	244.510	-34.692	1.146
30407-01 B	16	244.510	-34.692	1.002
390 A	145	111.451	27.247	5.576
4151 A	53	154.180	75.586	1.020
4151 E	90	154.180	75.586	1.129
4151 D	20	154.180	75.586	1.186
4U0614+091 A	29	201.227	-2.779	1.000
4U0614+091 B	25	201.227	-2.779	1.002
4U_1626-67 A	100	322.006	-13.500	1.008
7172 A	97	15.615	-53.699	1.009
AU A	46	13.070	-37.399	1.002
AU B	43	13.070	-37.399	1.000
COMA A	66	44.993	87.505	1.017
H0348-120 A	98	202.387	-44.184	1.041
HD5394 A	51	123.945	-1.858	1.001
HD5394 B	29	123.945	-1.858	1.002
J1655 A	65	345.360	1.908	1.011
J1655 D	23	345.360	1.908	1.008
J1712 A	9	0.219	8.179	1.000
J1712 B	39	0.219	8.179	1.013
J1940 E	78	29.118	-15.737	3.370
MRK_279 A	50	114.738	47.083	1.113
NGC3783 A	70	288.019	22.850	1.010
NGC_4507 A	134	300.194	22.653	1.046

Table A.1: Observations used in Analysis

Observation	Length ksec	l	b	Smearing factor
NGC_7469 A	697	83.996	-45.586	1.078
NMKN_348 C	182	122.911	-30.641	1.099
SS_433 A	43	40.036	-2.715	1.004
VW A	78	284.809	-38.197	1.354
X0142+614 A	40	129.740	-0.062	1.013
a754 C	82	239.746	25.076	1.246
bp6 A	174	135.327	41.638	1.064
bycam A	202	152.058	16.215	1.253
cenx3 A	257	292.435	0.182	1.041
cenx3a A	9	292.435	0.182	1.000
cygx3 A	84	80.170	0.528	1.015
cygx3 B	56	80.170	0.528	1.030
cygx3 C	48	80.170	0.528	1.169
cygx3 D	11	80.170	0.528	1.087
cygx3 E	10	80.170	0.528	1.000
j0437 A	68	253.295	-41.711	1.049
j1008 A	51	283.324	-1.874	1.000
j1008 B	45	283.324	-1.874	1.000
j1008 C	56	283.324	-1.874	1.015
j1008 D	9	283.324	-1.874	1.006
j1808 A	158	355.709	-8.725	1.012
mcg630 C	408	313.922	27.283	1.059
mcg81111 A	85	166.061	10.985	1.253
ncygx2 A	85	87.775	-11.406	1.031
ncygx2 B	224	87.775	-11.406	1.233
ncygx2a A	42	87.775	-11.406	1.000
ngc253 A	17	127.949	-87.619	1.032
ngc253 B	29	127.949	-87.619	1.008
ngc3516 A	265	133.130	42.801	1.009
ngc3516 B	174	133.130	42.801	1.011
txcol A	115	246.818	-29.431	1.211
txcola A	13	246.818	-29.431	1.000
txcola B	18	246.818	-29.431	1.194
velax1 B	29	263.441	4.083	1.000
velax1 D	70	263.441	4.083	2.107
xper A	35	163.575	-16.685	1.001

Table A.1: Observations used in Analysis

Observation	Length ksec	l	b	Smearing factor
xper A	70	163.575	-16.685	1.033

Appendix B

Extraction Software

B.1 Software

Here is a short introduction to my HEXTE packet data archive extraction tools. They are all based around David Marsdens wonderful program get_accum.

Location of Software

My idl files are located on mamacass.ucsd.edu in /home/dm/xte/idl. Davids idl programs are also on mamacass in /home/hexte/idl. All the other tools are on mamacass in /home/HEXTE/solaris_bin.

B.1.1 First the shell scripts

scanh

Usage: scanh keyword

scanh takes a human readable or obscat file and searches the start line, PI and SOURCE for a match with the keyword string. It outputs the observations that have a match in any of the three lines. If the output from scanh is redirected into a file with the extension .obs it can be used as input to tgood and thk2.

tgood

Usage : tgood path

tgood takes the observations in the .obs files in path and creates a shell script to collect the data needed by get_accum. the scripts have the extension .good.

***.good scripts**

The scripts assume the correct initial CD (if any) has been placed in the CD drive. The scripts prompt for all further CD's. The data is placed in a subdirectory dat which is created if necessary. There are four different types of files created by the *.good scripts: the event data file (.dat), the livetime correction data file (.cor2), the ra and dec file (.a14) and the housekeeping information file (.hk2). The housekeeping file has the following fields: idf, shield a, pme1 LLD, pme1 XULD, particle monitor LLD, internal saa detection, modulator position, dwell, and science mode.

thk

Usage : thk pre_saa_timelag(seconds) post_saa_timelag(seconds) path

thk reads in the .obs files in path and creates .xliv files for each. The .xliv files contain the good data times that have not been corrected for the proper occult times.

fliv

Usage : fliv ra dec horiz_angle path

fliv takes the .xliv files crated by thk and corrects them for the proper earth occult times. The output files are named .liv and are the input files for observe2a and observe2b

epmxyz

Usage : epmxyz < *.liv

epmxyz outputs spacecraft coordinates for data intervals in a .liv file. The output is in the form:
avgMET avgX avgY avgZ #ofIDFs sigmaX sigmaY sigmaZ

B.1.2 Now the idl programs

observe2a.pro and observe2b.pro

Usage : observe2[ab],filename,/fits,/cor

filename is the root name of a .liv[12] file (without the .liv extension.) observe creates a idl save file with the total spectra for the livetime intervals in filename. The

/fits parameter creates fits files of this spectrum. The /cor option causes get_accum to make the Fred and Biff corrections. observe2a is for cluster a and observe2b is for cluster 2. The programs observe* are a wrapper around get_accum(TM).

get_accum is a trademark of Marsden Enterprises.